UNIVERSITY OF CALGARY

Finite Element Analysis of the Interventricular Septum

by

Gregory Scott Nelson

A DISSERTATION

SUBMITTED TO THE FACULTY OF GRADUATE STUDIES

IN PARTIAL FULFILMENT OF THE REQUIREMENTS FOR THE

DEGREE OF DOCTOR OF PHILOSOPHY

PROGRAMME OF BIOMEDICAL ENGINEERING

CALGARY, ALBERTA

FEBRUARY, 1999

Abstract

The interventricular septum, which flattens and inverts in conditions such as pulmonary hypertension and mitral stenosis, is considered by many to be an unstressed membrane, in that its position is assumed to be determined solely by the transseptal pressure gradient (TSP). A 2-D finite element model (including the effects of hyperelasticity, geometric nonlinearity, and residual stress) was developed to investigate whether compression and bending moments (behaviour incompatible with a membrane) exist in the septum during diastole under abnormal loading conditions (pulmonary artery [PA] constriction). Hemodynamic and echocardiographic data were obtained in 6 open-chest anaesthetized dogs. For both control and PA-constriction cardiac cycles, the measured LV and RV pressures (LVP and RVP) were applied to a residually stressed mesh (RS mesh). The shear modulus, G, and end-bending moments were adjusted until the deformed, loaded RS mesh matched satisfactorily the observed configuration of the septum. During PA constriction, a greater G was required to obtain matches relative to control, as were end-bending moments (end-bending moments were not required for the control). Furthermore, substantial circumferential compressive stresses occurred during PA constriction compared to those which occurred during control. The development of substantial compression may have important implications with respect to diastolic suction. It is also conceivable that such compressive stresses might impede septal blood flow and contribute to the unexplained ischemia observed in some conditions characterized by abnormal septal motion.

Acknowledgements

Thanks to my teachers...

Dr. John Tyberg – you introduced me to the exciting world of cardiac mechanics, and you made my graduate experience extraordinary. I will never forget your patience.

Dr. Nigel Shrive – you introduced me to biomedical engineering, and you taught me everything I know about structural mechanics. Long live bending moments.

Dr. Henk ter Keurs – you showed me the importance of the F-SL relation, and not to be afraid to use it.

Dr. Ezzeldin Sayed-Ahmed – you taught *me* the language of ABAQUS and even some Fortran, now that was an accomplishment.

Thanks to my colleagues...

Mr. Gerry Groves – your door was always open to me, you are one of the kindest and most helpful people I know. Coffee-partners for life.

Mrs. Cheryl Meek – you made my experiments a success, and turned me on to carotid cut-downs and cardiac surgery.

Mr. Dale Bergman and Mr. John Nystrom – there was never a computer problem you could not solve.

Dr. Rosa Sas – your data-crunching knowledge and plotting expertise saved me

many times.

Drs. Ellen Hollander, Yi Hui Sun, and Mrs. Lisa Semeniuk-Woo – as fellow graduate students you made my work-life enjoyable and I think some of your female sensitivity rubbed off on me (Danielle thanks you).

Thanks to my best friends...

Mr. Mark Richardson and Mr. Brad Scott – you kept me sane throughout this whole process. Friends for life boys.

Thanks to my immediate and extended family...

Your support has meant so much to me.

Thanks to my parents...

Mrs. Marlene Nelson and Mr. Rick Scarff – for your support and especially Sunday-night dinners.

Thanks to my wife...

Dr. Danielle Nelson – you truly are the most important person in my life, you understand everything that I have had to endure. You complete me.

Finally, thanks to...

Medical Research Council of Canada – for providing me with a studentship and supporting my research throughout my graduate programme.

To my wife,

Danielle

D • G MAY 9 1998

Table of Contents

Approval Page....ii

Abstract....iii

Acknowledgements....iv

Dedication....vi

Table of Contents....vii

List of Tables....xii

List of Figures....xiii

List of Abbreviations....xxiv

Glossary....xxviii

Epigram....xxxvi

Chapter 1

The Interventricular Septum: Structural Aspects and Significant Studies....1

1.1 Anatomy....2

1.2 Fibre Architecture....3

1.3 Blood Supply....3

1.4 Conduction System....4

1.5 Mechanics of the Septum Under Physiological Conditions....5

1.6 Mechanics of the Septum Under Pathophysiological Conditions....6

Chapter 2

Analysis of Stress in the Heart 24

2.1 Wall Stress and Cardiac Function 25

2.2 Measurement of Wall Stress *In Vivo* 26

2.3 Thin- and Thick-Walled Models Used to Calculate Ventricular Wall Stress 26

2.4 The Finite Element Method 32

2.5 FE Analysis of Ventricular Wall Stress 33

Chapter 3

Experimental Methods 45

3.1 Animal Preparation 46

3.2 Echocardiographic Frame Acquisition 47

3.3 Experimental Protocol 48

3.4 Hemodynamic Data Analysis 48

3.5 Echocardiographic Frame Analysis 48

3.6 Statistical Analysis 48

Chapter 4

FE Model and FE Analysis Description 51

4.1 Use of the FE Method to Model the Interventricular Septum 52

4.2 FE Method Description 53

4.3 FE Software/Computer Hardware....54

4.4 FE Mesh....55

4.5 Constitutive Relations....55

4.6 Geometric Nonlinearity....56

4.7 FE Solution....58

4.8 Incorporation of Residual Stress....58

4.9 Accounting for Sarcomere Length Changes during the Cardiac Cycle....59

4.10 Loading Conditions....59

4.11 Mesh Sensitivity Analysis....60

Chapter 5

Results....71

5.1 Hemodynamics and Cardiac Function during Diastole....72

5.2 Septal Geometry during Diastole....74

5.3 Structural Mechanics of the Septum during Diastole....74

5.3.1 *Shear Modulus (G) and End-Bending Moments*....74

5.3.2 *Principal Stress Vector Plots*....76

5.3.3 *Structural Bending Stiffness (K_{bend})*....78

5.3.4 *Axial Force and Bending Moment Diagrams*....80

5.3.5 *Strain Energy*....81

5.4 Model Validation and Evaluation....82

5.4.1 *Comparison of FE Solution with*

Thick-Walled Cylindrical Solution.....82

5.4.2 *Plane Stress vs. Plane Strain*.....84

Chapter 6

Discussion.....121

6.1 Effect of PA Constriction on

Hemodynamics and Septal Geometry.....122

6.2 Model Findings and Considerations.....123

6.2.1 *Increased K_{bend} and G during PA Constriction*.....123

6.2.2 *End-Bending Moment Requirements during*

PA Constriction.....126

6.2.3 *Arch-Like Behaviour of the Distorted Septum*.....127

6.2.4 *Comparison of Control Results with Thick-Walled Model*.....129

6.2.5 *Variation of Axial Force and Bending Moment*

in the Septum.....131

6.2.6 *Strain Energy and Diastolic Suction*.....133

6.2.7 *Reverse FE Analysis*.....135

6.2.8 *Neo-Hookean Stress-Strain Relation*.....136

6.2.9 *Principal Stresses*.....138

6.2.10 *Assessment of Septal Geometry*.....138

6.2.11 *Residual Stress*.....139

6.3 Conclusions.....140

Chapter 7

Future Directions 143

7.1 Circumferential Compressive Stress and Septal Ischemia 144

7.2 Effects of the Pericardium and Extension of the Model to the LV Free Wall 144

7.3 Fibre Architecture and Nonlinear Constitutive Relations 145

7.4 Long-Axis Inversion of the Septum 147

References 148

List of Tables

Table 5.1

Effect of PA constriction on mean diastolic aortic pressure.....85

Table 5.2

SE_{60} (strain energy calculated for 60% of the mesh) expressed as a percentage of SE_{full} (strain energy calculated for the entire mesh) during control and PA constriction at the maximum negative transseptal pressure gradient and end-diastole.....115

List of Figures

Chapter 1

Figure 1.1

Illustration of the traditional view of the ventricles.....15

Figure 1.2

Schematic diagram of the membranous and muscular components

of the interventricular septum.....16

Figure 1.3

Orientation of muscle fibres across the left ventricular free wall.....17

Figure 1.4

Bifurcation of myocardial fibres at the anterior interventricular sulcus.....18

Figure 1.5

Schematic diagram of the coronary arteries responsible for blood supply

of the normal human interventricular septum.....19

Figure 1.6

Plot of the transseptal pressure gradient and end-diastolic right

ventricular and left ventricular septum-to-free wall diameters.....20

Figure 1.7

Cross-sectional echocardiograms of the heart during control and

PA-constriction loading conditions in diastole.....21

Figure 1.8

3-D plot showing the combined effects of the transseptal pressure

gradient and left ventricular transmural pressure on septal segment length.....22

Figure 1.9

Plot of the transseptal pressure gradient and end-diastolic and

end-systolic right ventricular septum-to-free wall diameters.....23

Chapter 2

Figure 2.1

Distribution of radial, circumferential, and longitudinal stress from

endocardium to epicardium in the wall of an ellipsoidal ventricle.....39

Figure 2.2

Stress distribution in the myocardium based on a thick-walled model.....40

Figure 2.3

Myocardial wall stress distribution at end-diastole and end-systole computed with fibre orientation incorporated in the model.....41

Figure 2.4

Circumferential stress (normalized to LaPlace stress), based on classical theory and finite deformation theory, plotted as a function of wall thickness.....42

Figure 2.5

Comparison of passive pressure-volume curves predicted by a finite element model when the material of the wall was composed of a nonlinear as compared to a linear constitutive relationship.....43

Figure 2.6

Comparison of the chamber stiffnesses expressed as a function of the pressure when classical theory vs. finite deformation theory was used for a finite element model.....44

Chapter 3

Figure 3.1

Geometric analysis of the interventricular septum.....50

Chapter 4

Figure 4.1

Schematic diagrams of a cross-sectional (minor-axis) view of the heart and loading of the septum during PA constriction.....61

Figure 4.2

A loaded structure and a typical finite element model.....62

Figure 4.3

2-D finite element mesh used to model the interventricular septum.....63

Figure 4.4

Diagram illustrating the "pδ" effect.....64

Figure 4.5

Diagram illustrating how the residually stressed mesh was obtained.....65

Figure 4.6

Plot of circumferential residual stress as a function of radial position.....66

Figure 4.7

Sarcomere length changes during the cardiac cycle.....67

Figure 4.8

Diagram illustrating how the dimensions of the initial residually stressed mesh were adjusted according to sarcomere length during the diastolic interval....68

Figure 4.9

Diagram depicting how the residually stressed mesh was loaded for both control and PA-constriction cycles....69

Figure 4.10

Comparison of transseptal (mid-septum) circumferential stress profiles obtained from 3 different meshes under the same loading (PA constriction)....70

Chapter 5

Figure 5.1

Plot of left ventricular pressure as a function of time during diastole (control and PA constriction)....86

Figure 5.2

Plot of right ventricular pressure as a function of time during diastole (control and PA constriction)....87

Figure 5.3

Plot of the transseptal pressure gradient as a function of time during diastole (control and PA constriction).....88

Figure 5.4

Plot of left ventricular cross-sectional area as a function of time during diastole (control and PA constriction).....89

Figure 5.5

Plot of left ventricular pressure as a function of left ventricular cross-sectional area during diastole (control and PA constriction).....90

Figure 5.6

Plot of left ventricular transmural pressure as a function of time during diastole (control and PA constriction).....91

Figure 5.7

Plot of right ventricular transmural pressure as a function of time during diastole (control and PA constriction).....92

Figure 5.8

Plot of curvature of the mid-portion of the septum as a function of time

during diastole (control and PA constriction).....93

Figure 5.9

Plot of insertion-point length of the septum as a function of time during diastole (control and PA constriction).....94

Figure 5.10

Plot of thickness of the septum as a function of time during diastole (control and PA constriction).....95

Figure 5.11

Plot of shear modulus of the septum as a function of time during diastole (control and PA constriction).....96

Figure 5.12

Plot of end-bending moments as a function of time during diastole (PA constriction only).....97

Figure 5.13

Schematic diagram relating x-plane- , y-plane- , and shear-stress to principle stresses.....98

Figure 5.14

Principal stress vector plots for control and PA-constriction loading conditions at the maximum negative transseptal pressure gradient.....99

Figure 5.15

Plots of transseptal circumferential stress and strain for control and PA-constriction loading conditions at the maximum negative transseptal pressure gradient.....101

Figure 5.16

Principal stress vector plots for control and PA-constriction loading conditions at mid-diastasis.....102

Figure 5.17

Plots of transseptal circumferential stress and strain for control and PA-constriction loading conditions at mid-diastasis.....104

Figure 5.18

Principal stress vector plots for control and PA-constriction loading conditions at end-diastole.....105

Figure 5.19

Plots of transseptal circumferential stress and strain for control and PA-constriction loading conditions at end-diastole.....107

Figure 5.20

Plot of structural bending stiffness of the septum as a function of time during diastole (control and PA constriction).....108

Figure 5.21

Schematic diagram of a circumferential stress distribution across the septum.....109

Figure 5.22

Axial force plotted as a function of element column position for control (at mid-diastasis and end-diastole) and PA-constriction (inverted septum and flattened septum) loading conditions.....110

Figure 5.23

Bending moment plotted as a function of element column position for control (at mid-diastasis and end-diastole) and PA-constriction (inverted septum and flattened septum) loading conditions.....111

Figure 5.24

Plot of strain energy in the septum as a function of time during diastole (control and PA constriction)..... 112

Figure 5.25

Plot of strain energy (in the septum) and left ventricular cross-sectional area as a function of time during diastole (control)..... 113

Figure 5.26

Plot of strain energy (in the septum) and left ventricular cross-sectional area as a function of time during diastole (PA constriction)..... 114

Figure 5.27

Comparison of transseptal radial stress values calculated by the finite element model and a thick-walled solution during control (at end-systole, mid-isovolumic relaxation, mid-diastasis, and end-diastole)..... 116

Figure 5.28

Comparison of transseptal circumferential stress values calculated by the finite element model and a thick-walled solution during control (at end-systole and mid-isovolumic relaxation)..... 117

Figure 5.29

Comparison of transseptal circumferential stress values calculated by the finite element model and a thick-walled solution during control (at mid-diastasis).....118

Figure 5.30

Comparison of transseptal circumferential stress values calculated by the finite element model and a thick-walled solution during control (at end-diastole).....119

Figure 5.31

Comparison of results obtained from finite element meshes constructed using either plane-stress or plane-strain elements (control and PA constriction at mid-diastasis).....120

Chapter 6

Figure 6.1

Deformation and bending moment diagram of a beam with fixed ends subject to uniformly distributed loading.....142

List of Abbreviations

AoP	aortic pressure
CSA_{LV}	cross-sectional area of the LV
δ	deformation
$[\delta]$	nodal deformation vector
ε_i	principal normal strain
ε_x	strain in the x-plane
ε_y	strain in the y-plane
ε_z	strain in the z-plane
E	Young's modulus
ED	end-diastole
ES	end-systole
FE	finite element
$\{F\}$	nodal force vector
G	shear modulus
IVR	isovolumic relaxation
$\bar{I}_1$	first deviatoric stretch invariant
J	volumetric strain
K_{bend}	structural bending stiffness
$[K_{element}]$	element stiffness matrix
$[K_{geom}]$	geometric matrix

$[K_{struct}]$	structural stiffness matrix
$[K_{struct\text{-}red}]$	reduced structural stiffness matrix
λ_i	principal stretch
$\overline{\lambda_i}$	deviatoric stretch
L_{IP}	insertion-point length
L_{septal}	septal midwall segment length
LAD	left anterior descending (coronary artery)
LBBB	left-bundle branch block
LV	left ventricle
LVEDP	left ventricular end-diastolic pressure
LVP	left ventricular pressure
LVP_{peri}	left ventricular pericardial pressure
LVTMP	left ventricular transmural pressure
Max TSP_{neg}	maximum negative transseptal pressure gradient
M_0	initial bending moment
M_{pri}	primary bending moment due to lateral loading
M_{sec}	secondary bending moment due to $p\delta$ effect
M_{tot}	total bending moment due to lateral loading and $p\delta$ effect
υ	Poisson's ratio
p	axial load
P_i	internal pressure loading
P_o	external (outer) pressure loading

PA	main pulmonary artery
R_i	internal short-axis radius of curvature
R_o	external (outer) short-axis radius of curvature
R_{septal}	septal short-axis radius of curvature
RS	residually stressed (mesh)
RV	right ventricle
RVP	right ventricular pressure
RVP_{peri}	right ventricular pericardial pressure
RVPO	right ventricular pressure overload
RVTMP	right ventricular transmural pressure
RVVO	right ventricular volume overload
σ_{circ}	circumferential stress
σ_{long}	longitudinal stress
σ_{LV}	circumferential stress at the LV-septal surface
σ_{max}	maximum principal stress
σ_{min}	minimum principal stress
σ_{rad}	radial stress
σ_{RV}	circumferential stress at the RV-septal surface
σ_x	stress in the x-plane
σ_y	stress in the y-plane
σ_z	stress in the z-plane
$\{\sigma\}$	axial stress vector

SD	standard deviation
SE_{full}	strain energy calculated for the entire mesh
SE_{60}	strain energy calculated for 60% of mesh
SL	sarcomere length
τ_{xy}	shear stress in the x-y plane
θ_p	principal stress angle
t	thickness
T	tension
TSP	transseptal pressure gradient
$U(\varepsilon)$	strain-energy function

Glossary

Anisotropy – elastic properties of the material vary with direction

Axial force – force resultant which passes through the centroid of a particular section and is parallel to the longitudinal axis of the member at that section

Axisymmetric – symmetric about an axis

Bending moment – moment is a load resultant which produces a rotation; bending moment is a moment for which the rotation appears as bending of a member

Boundary condition – constraint which defines how a structure is loaded, deforms or displaces in space

Bundle branches – branches from the His bundle which extend to the right and left ventricles

Circumferential – direction around the axis of a solid of revolution (perpendicular to any radius)

Closed form solution – precise equation based on exact analysis of a continuum from the

governing differential equations of continuum mechanics

Compressive stress – stress which causes an elastic body to shorten in the direction of the applied stress

Constitutive relation – quantitative relationship between the stresses and strains in a material

Continuum mechanics – study of distribution of physical quantities under circumstances where their discrete nature is unimportant; they may be regarded as continuous functions of position; a continuum is deemed to be the same down to infinitesimal size

Coronary artery – artery which supplies heart tissue with blood

Coronary stenosis – narrowing of the lumen of a coronary artery

Coronary sinus – venous sinus opening into the right atrium which drains the cardiac veins

Crux of the heart – intersection of the walls separating the right and left sides and the atrial and ventricular chambers of the heart

Deviatoric strain – strain which produces a change in shape without a change in volume

Diastasis – phase of slow ventricular filling

Diastole – relaxation and filling phase of the cardiac cycle

Element – a division of the structure of interest of finite size

Element stiffness matrix – relationship between nodal forces and nodal displacements as with a linear spring

Ellipsoid – surface whose intersection with every plane is an ellipse

Endocardium – inner surface of the heart

Epicardium – outer surface of the heart

Gaussian integration – numerical technique for estimating the area under a curve

Hemodynamics – circulatory movements of blood and the forces involved in circulation

Heterogeneity – different properties at different locations

His bundle – band of specialized fibres that carry the cardiac action potential from the atrioventricular node to the interventricular septum and then to the right and left ventricles via the bundle branches

Homogeneity – physical properties consistent throughout an elastic body

Hypertrophy – enlargement or overgrowth of an organ due to an increase in size of its constituent cells

Incompressibility – when volume is conserved during deformation

Invariance – property of a physical quantity being unchanged by certain transformations or operations

Ischemia – insufficient blood supply to an organ or tissue

Isotropy – elastic properties of a material are the same in all directions

Isovolumic relaxation period – during diastole, relaxation with little or no change in volume

Large deformation theory – when rotations, displacements, and strains are large with

respect to the undeformed body, resulting in nonlinear strain-displacement relations

Left bundle branch block – interruption of conduction in left bundle branch

Linear elasticity – linear stress-strain relationship

Longitudinal – direction along the long-axis of a solid of revolution

Mitral stenosis – narrowing of the mitral (left atrioventricular) orifice

Mueller manoeuver – inspiratory effort with a closed glottis after expiration; results in negative intrathoracic pressure with engorgement of intrathoracic vascular structures

Myocardial infarction – death of heart muscle as a result of interruption of blood supply to the area

Myocardium – heart muscle

Nodal deformation vector – matrix of nodal displacements

Nodal force vector – matrix of nodal forces

Node – location where elements are connected

Nonlinear elasticity – nonlinear stress-strain relationship

Pericardium – membranous sac surrounding the heart and roots of the great vessels, consisting of an outer fibrous layer and an inner serosal layer

Plane strain – development of strains in the plane of interest only, no strain components in the direction perpendicular to the plane

Plane stress – development of stresses in the plane of interest only, no stress components in the direction perpendicular to the plane

Poisson's ratio – ratio of transverse strain to axial strain under uniaxial loading

Principal plane of stress – for a point in an elastic body, a plane at that point across which the shear stress vanishes

Pulmonary hypertension – increased pressure within the pulmonary arterial circulation

Purkinje fibres – terminal branches of the cardiac conducting system that run along the subendocardium

Radial – direction across the wall thickness along the radius of curvature

Roentgenographic – radiographic

Sarcomere – repeating contractile units of myofibrils, composed of overlapping actin and myosin filaments

Shape function – mathematical expression which defines how a finite element displaces given a unit displacement in one direction at one node

Shear modulus – relationship between shear stress and shear strain

Small deformation theory – when rotations, displacements, and strains are small with respect to the undeformed body (i.e., < 1 %); strains are differentials of the displacements, not necessarily linear functions

Strain – change in length per unit length

Strain energy – potential energy stored in a body by virtue of an elastic deformation; equal to the work that must be done to produce this deformation

Stress – force per unit cross-sectional area of a material

Stroke volume – the volume of blood pumped from each ventricle during a single contraction; the difference between end-diastolic and end-systolic volume

Systole – contraction and ejection phase of the cardiac cycle

Tensile stress – stress which causes an elastic body to lengthen in the direction of the applied stress

Thebesian channels – vascular channels which originate in the myocardium and open directly into the chambers of the heart, bypassing the coronary venous return to the right atrium

Trabeculae carneae – irregular muscle bundles projecting from the interior of the ventricles

Transversely isotropic – elastic properties of a material are the same in one plane but different in the direction perpendicular to the plane

Volumetric strain – strain which produces a change in volume without a change in shape

Young's modulus – slope of the linear relationship between extensional stress and strain

Too often biologists simply cannot bring themselves to make a sufficiently serious study of the structural aspects of their problems. Yet there can be no reason to assume that, while Nature uses methods of infinite subtlety in her chemistry and her control mechanisms, her structural approach should be a crude one.

James E. Gordon, *Structures*

CHAPTER 1

THE INTERVENTRICULAR SEPTUM:

STRUCTURAL ASPECTS AND SIGNIFICANT STUDIES

To understand the potential structural behaviour of the interventricular septum under load, the structural aspects of the septum must be understood. After a brief description of the anatomy, fibre architecture, blood supply, and conduction system of the septum, a number of studies which have contributed significantly to the understanding of septal mechanics are reviewed.

1.1 Anatomy

As its name indicates, the interventricular septum is located between the left and the right ventricles (LV and RV, respectively) of the heart. Figure 1.1 illustrates the traditional view of the ventricles. The RV wraps around approximately ⅓ of the circumference of the comparatively thicker LV and defines the zone of the interventricular septum (cross hatching).[138] Figure 1.2 shows that the septum (long-axis view) is roughly triangular in shape (with the base of the triangle at the level of the aortic cusps),[1] and is comprised of both membranous and muscular components.[6] This dissertation will focus on the muscular septum. The membranous septum, which does not contract, is a small structure located at the junction of the inlet, trabecular and outlet components of the muscular septum. Most investigators agree that the membranous septum represents the closure of the last version of the interventricular foramen and that most of this part of the septum is derived from the tissue of the atrioventricular "cushion."[46] The inlet component of the muscular septum separates the inlet portions of the LV and RV and extends to the crux of the heart (the point of junction of the interventricular, interatrial and posterior interventricular grooves[2]). The

trabecular septum is characterized by interlacing muscle bundles, the *trabeculae carneae*, and extends from the membranous septum to the apex at an angle of $\approx 45°$. The outlet part of the muscular septum separates the outlet portions of the LV and RV and merges imperceptibly with the upper part of the trabecular septum.[6]

1.2 Fibre Architecture

Streeter et al[144,145,147] analysed the orientation of muscle fibres across the LV free wall. They found the middle 60% to have a nearly circumferential fibre orientation, with fibres becoming increasingly oblique on either side of this central zone (see Figure 1.3). The fibre architecture of the septum is equivalent to that of the LV free wall[117,145] except at the RV insertions where a portion of the septum derives from the subendocardial fibres (i.e., just beneath the interior surface of the ventricle) of the RV free wall (see Figure 1.4).[42,144] In contrast to the subepicardial fibres (i.e., just beneath the exterior surface of the ventricle) which run continuously (along the anterior and posterior interventricular grooves) from the RV free wall to the anterior surface of the LV, the subendocardial fibres bend back to form part of the septum.[153]

1.3 Blood Supply

The septal myocardium in the human receives most of its blood supply from the long penetrating arteries of the left anterior descending (LAD) coronary artery, as depicted in Figure 1.5.[69] The septal branches of the posterior descending coronary artery contribute

only slightly to the total blood supply of the septum. The only value of these posterior penetrating arteries may be as a source of potential collateral circulation. Although not shown, the majority of venous blood in the human septum is drained into the left anterior interventricular vein; the remainder into the posterior interventricular vein. Both of these veins empty into the coronary sinus, through which the venous blood ultimately reaches the right atrium.[69]

In contrast to humans, a single major septal artery, branching from either the left coronary artery or LAD, penetrates directly into the septal myocardium in dogs.[14,109,161] Furthermore, venous drainage of the septal artery occurs by way of Thebesian channels, which empty directly into the RV rather than by way of the coronary sinus.[102,118]

1.4 Conduction System

The conduction system of the interventricular septum is well defined. The bundle of His proceeds down the subendocardial surface of the right side of the septum for approximately 1 cm before dividing into right and left bundle branches. The right bundle branch emerges directly from the bundle of His and continues down the right side of the septum. The left bundle branch emerges almost perpendicularly from the bundle of His, perforating the septum and splitting into anterior and posterior divisions. These two divisions, together with the right bundle branch, finally subdivide into a complex network of conducting fibres called Purkinje fibres, which branch out over the subendocardial surfaces of both ventricles.[13]

1.5 Mechanics of the Septum Under Physiological Conditions

Understanding the motion pattern of the interventricular septum and how this structure relates to the rest of the heart under physiological conditions is essential in order to appreciate fully its behaviour under pathophysiological (i.e., abnormal) conditions. Under physiological conditions, when LV pressure (LVP) is greater than RV pressure (RVP), the transseptal pressure gradient (TSP = LVP - RVP) is positive by several mm Hg at end-diastole and can be as high as 100 mm Hg at end-systole. Consequently, the septum maintains a short-axis (i.e., axis perpendicular to the long-axis of the LV) radius of curvature throughout diastole (i.e., ventricular relaxation and filling with blood) and systole (i.e., ventricular contraction and ejection of blood) and which appears equivalent to that of the LV free wall.[77,138] Many studies, however, have shown that the short-axis radius of curvature of the septum is slightly greater than that of the LV free wall.[3,21,40,54,68,77,86,88] The thickness of the septum nearly matches that of the LV free wall and the septum contains roughly ⅓ of the total LV mass.[48] Under physiological conditions, the septum thickens and moves leftward during systole, toward the centre of the LV cavity;[138] the opposite occurs during diastole. Systolic thickening of the septum results from longitudinal and latitudinal shortening of the septal myocardium, similar to what occurs in the LV free wall.[133] The septum, based on information presented thus far, seems to operate as part of the LV, both from an anatomic and functional viewpoint.[8,138]

1.6 Mechanics of the Septum Under Pathophysiological Conditions

Interest in the mechanics of the interventricular septum may have been initiated as early as 1914, when Henderson and Prince[60] suggested that displacement of the septum during diastole might explain how filling of one ventricle influenced the performance of the other. The substantial interest in the septum, however, came much later as a result of a study by Popp et al[121] who were the first to observe that patients with RV volume overload (RVVO), in addition to having a large RV during diastole, exhibited rightward motion of the septum during systole. This rightward systolic motion was labelled "paradoxical" because of the apparent contradiction with what occurs under normal conditions (i.e., the septum normally moves leftward during systole). Later findings by Diamond et al[32] in patients and by Kerber et al[76] in dogs supported the observations made by Popp et al.[121] Bemis et al,[11] using a contracting dog heart model, showed that increasing RV volume resulted in proportional increases in LV end-diastolic pressure without affecting LV volume. It was reasoned that the septum shifted abnormally leftward during diastole resulting in an alteration in LV geometry. Similar findings were reported by Elzinga et al[35] in cats and by Santamore et al[131] in rabbits.

Observations consistent with those described during RVVO also occurred under RV pressure overload (RVPO) conditions. Stool et al[143] constricted the pulmonary arteries (PA constriction) in dogs and observed a gradual increase in RV diastolic pressure and a decrease in LV septum-to-free wall diameter at end-diastole. They speculated that this was the result of a leftward shift of the septum during diastole. Similar findings were reported

by Badke[10] and by Olsen et al[108] in dogs.

Paradoxical septal motion is not consistent with the traditional view that the septum functions as part of the LV. Consequently, the function of the septum becomes difficult to understand under abnormal conditions. Studies which have helped to define better the determinants of septal position and motion under abnormal conditions will now be discussed.

Kingma et al[78] developed an open-chest canine model and investigated the effects of both RVVO and RVPO on the position and motion of the septum, as determined by sonomicrometry and 2-D echocardiography. Both RVVO and RVPO resulted in a progressive increase in the end-diastolic RV septum-to-free wall diameter and a reciprocal decrease in the end-diastolic LV septum-to-free wall diameter, thereby confirming the studies described previously.[10,11,35,108,131,143,148] Furthermore, Kingma's study showed that the septal position at end-diastole (as reflected by the septum-to-free wall diameters) was governed by the transseptal pressure gradient, TSP (see Figure 1.6). As mentioned previously, TSP is normally positive at end-diastole (by several mm Hg) and the septum is concave to the LV. RVVO and RVPO, however, which cause a reduction (and, in some cases, a reversal) in TSP, result in a leftward shift, and in some cases a complete inversion of the septum (as depicted in Figure 1.7b, in contrast to control). This shift was progressive and proportional to the magnitude of the alteration in TSP. It was suggested that paradoxical septal motion was a result of a septum, displaced leftward during diastole by an abnormal TSP, being restored to its normal configuration when the greater systolic LVP

caused TSP to become more positive. The more leftward the septum is shifted at end-diastole secondary to a decreased (or reversed) TSP, the more prominent the paradoxical motion during systole (results which confirm previous studies by Pearlman et al[116] and by Laurenceau and Dumesnil[83]). Meyer et al[95] proposed another explanation for the occurrence of paradoxical septal motion during RVVO. They suggested that the dilated RV displaces the LV posteriorly in the thorax during diastole and ejects its large volume of blood during systole, resulting in an anterior movement of the heart which exceeds the normal posterior motion of the septum. Consequently, a net anterior motion of the septum results. The results reported by Kingma et al[78] were compatible with those in conscious dogs of Visner et al[158] and, later, of Feneley et al.[41] Both of these studies emphasized the role of septal distortion during RVPO. In addition, Thompson et al[151] verified the principle that TSP determines septal position and showed that, in patients, the position of the septum is a function of the instantaneous TSP throughout diastole. These studies[78,151] seem to suggest that the septum behaves like a passive compliant membrane between two liquid-filled chambers and that its position is assumed to be determined solely by a continuous monotonic function of the diastolic TSP.

In a more recent study, Dong et al[34] related simultaneous measurements of the septal short-axis radius of curvature, R_{septal} (2-D echo), and septal midwall segment length, L_{septal} (sonomicrometry), to LVP, RVP and ventricular septum-to-free wall diameter (2-D echo) during alternating PA constriction and aortic constriction in anaesthetized dogs. They demonstrated that, over a wide range of TSP (0 ± 7 mm Hg), changes in ventricular

diameters measured previously by Kingma et al[78] (described above) were proportional to the changes in L_{septal}, which they also showed was a linear function of TSP. Based on this information, it was concluded that echo-measured changes in ventricular diameters really do reflect changes in the length of the septum. Second, by using a plot of curvature ($1/R_{septal}$) versus TSP, they confirmed that the septum becomes flat only when TSP ≈ -5 mm Hg. This result was consistent with the results of other studies in patients by Lima et al[86] and by Agata et al,[3] which have shown that the septum flattened, but remained slightly concave toward the LV as TSP decreased to 0 mm Hg. The authors discussed a number of factors thought to be associated with the requirement of a significantly negative TSP to make the septum flat: (i) the observation that an excised septum suspended in isodensity liquid continues to be concave toward the LV, i.e., this is the natural configuration of the septum; (ii) the septum is a thick, complex structure and that thin-wall theory should not be expected to describe its behaviour; (iii) residual stress is thought to exist in the LV myocardium (Omens and Fung[110] reported that residual stresses can help maintain a more circular LV – and hence a more circular septum). Another contribution made by this study was that it demonstrated that the R_{septal} was not unique when TSP = 0 mm Hg. Rather, the R_{septal} changed with changes in the absolute ventricular intracavitary pressures. When TSP = 0 mm Hg, the R_{septal} increased with increasing LVP and RVP (i.e., TSP = 0 mm Hg was maintained, but at higher absolute intracavitary pressures). It was speculated that the increased ventricular pressures circumferentially and longitudinally stretched the septum from its junctions with the free walls, even though the net force acting on the septum in the

radial direction was relatively constant. This result seems to indicate that the TSP = 0 mm Hg state is not the unloaded state for the septum unless the ventricular pressures are also 0. The final contribution made by this study was that it demonstrated that septal curvature was dependent on LV transmural pressure (LVTMP = LVP - LVP_{peri}), as well as on TSP. During PA constriction, R_{septal} increased (i.e., the septum flattened) with decreasing TSP, whereas during aortic constriction, R_{septal} increased with increasing TSP. These results indicated that the mechanisms involved in changing R_{septal} were different during PA constriction and aortic constriction; the difference being the response of the pressures in either constriction. During PA constriction, the decrease in TSP caused a leftward shift of the septum and an increase in the R_{septal} until TSP ≈-5 mm Hg (the septum was flat). As TSP decreased below -5 mm Hg, the septum inverted with its curvature becoming negative and convex toward the LV. It was explained that in aortic constriction, however, the increase in R_{septal} was mainly caused by the symmetrical enlargement of the LV cavity (radii of both the septum and LV free wall increased by a similar amount) secondary to the combined effect of increased TSP and LVTMP. (Although LVTMP was not measured, aortic constriction increased LVP dramatically and therefore LVTMP would have also increased). The increase in the TSP gradient displaced the septum rightward, increasing the LV septum-to-free wall diameter. The increase in LVTMP distended the LV free walls, and also increased the LV septum-to-free wall diameter, resulting in a stretching of the septum at its junctions with the LV free wall. The combined effect of the increase in both TSP and LVTMP was an increase in R_{septal} (the distension pulled the septum toward the midline of

the two ventricles).

Earlier work by Kent et al[75] had suggested the importance of LVTMP on septal function. They implanted ultrasound crystals in the septum, and then measured strain produced by increasing LV end-diastolic pressure (LVEDP). Stiffness was assessed based on the relationship between LVEDP and strain (calculated stiffness coefficient). Based on their results, the authors suggested that segment-length strain in the septum is not solely dependent on the TSP (although their protocol did not vary TSP substantially), but probably depends in a more complicated fashion, on the stress distribution in the right and left ventricular free wall as well as the chamber pressures. Dong et al[33] defined the exact dependence of end-diastolic L_{septal} on TSP and LVTMP. They measured L_{septal} (sonomicrometry), LVP, RVP and LV pericardial pressure (in order to calculate LVTMP). LVTMP was increased through volume loading, whereas TSP was maintained constant at 10, 5, 0, -5, -10, and -15 mm Hg by adjusting the degree of constriction of the PA or aorta. Using a multiple second-order regression technique, they showed that the data were fit satisfactorily by an equation linear with respect to LVTMP and second-order with respect to TSP. A 3-D plot (see Figure 1.8) showing the combined effects of TSP and LVTMP on L_{septal} was constructed in this study. At any given level of TSP, L_{septal} increased with increasing LVTMP, and at any given level of LVTMP, L_{septal} increased with increasing TSP. The results of this study demonstrate that the end-diastolic L_{septal} depends both on LVTMP, which determines the stretching forces acting on the septum-ventricular free wall junctions, and on TSP, which determines the radial force on the septum. Moreover, these results

suggest that the septal stiffness and septal stress in an intact heart may not be accurately assessed without considering the effects of both LVTMP and TSP. Beyar et al,[15] in a parallel, modelling study, demonstrated the importance of the fact that the septum is a thick-walled structure, specifically that bending moments are important. Only when their model accounted for bending moments did it duplicate two critical features of the experimental results: (i) that the septum is not flat at TSP = 0 mm Hg and (ii) that L_{septal} continues to become shorter after septal inversion as end-diastolic TSP becomes progressively negative (secondary to PA constriction). The latter feature was surprising – the authors had expected re-extension of L_{septal} at greater negative values of TSP. (Molaug et al[104] had shown that PA constriction reduced end-diastolic segment length but had not made TSP negative). The observed result was consistent with L_{septal} having been measured using midwall crystals and with that midwall segment having been subjected to compressive stress because the extension stress was borne by the LV endocardial septal fibres during inversion. The results of this study contradict those of the previous echo studies,[78,86,148,151] which were important in defining the relationship between TSP and septal position, but were perhaps wrong in suggesting that during diastole the septum behaves like a passive compliant membrane. Rather, the septum may be behaving more like a thick-walled structure subject to lateral pressure and end-bending moments.

Although the aim of this dissertation is primarily to define the mechanics of the septum during diastole (also true of the studies described previously), it is helpful to consider studies which have helped to define the mechanics of the septum during systole.

In the presence of RVPO, numerous studies have shown that the septum remains displaced (flattened) leftward at end-systole.[10,108,143,148,158] As is the case with end-diastole, TSP is the main determinant of septal shape and motion at end-systole.[40,77,88,138,143] Smith and Tyberg,[138] in a study using chronically instrumented dogs, plotted (see Figure 1.9) RV septum-to-free wall diameters at end-diastole and at end-systole (measured by sonomicrometry) against the TSP gradient from 18 consecutive cardiac cycles during progressive RVPO (obtained by PA constriction). Although there was a tight linear relationship between TSP and both end-diastolic and end-systolic RV diameter, the slopes of these relationships were dramatically different. As expected, a much greater change in TSP was required to produce a given change in RV dimension during systole than during diastole – the greater end-systolic slope attributable to the greater stiffness of the myocardium during systole. Other intrinsic factors of the septum may be involved in systolic flattening. King et al,[77] in a study of normal children, found that during systole there was a progressive leftward shift in septal position with a resultant flattening and decrease in curvature of the septum. The authors explained that this systolic flattening of the septum resulted from the active effect of muscular contraction which was independent of ventricular pressures and tended to pull the septum toward a mid-line position since the shift occurred in the opposite direction to the increasing TSP gradient. Other investigators have noted that when the septum becomes flattened during diastole in response to the Mueller manoeuver, it remains flattened throughout systole with no response to the increased TSP.[21,54] It was suggested that muscular contraction caused an increase in

stiffness in the initially flattened septum and was sufficient to counterbalance the increase in TSP (which normally would push the septum toward the RV).[86]

Abnormal septal motion may influence the systolic performance of both the RV and the LV. Molaug et al,[103] in an experimental RVVO study, noticed that the stroke volume of the RV increased more than could be accounted for by the change in RV free wall segment length. They speculated that the increased stroke volume was primarily due to an increase in RV septum-to-free wall axis shortening. This observation was consistent with there having been paradoxical septal motion: leftward displacement of the septum at end-diastole resulting in rightward motion of the septum during systole. In this study, systolic performance of the LV was not affected. However, in a study by Feneley et al,[41] RVPO increased LV work at a given end-diastolic volume – direct systolic ventricular interaction (i.e., systolic displacement of the septum into the LV cavity) was accounted for the increase.

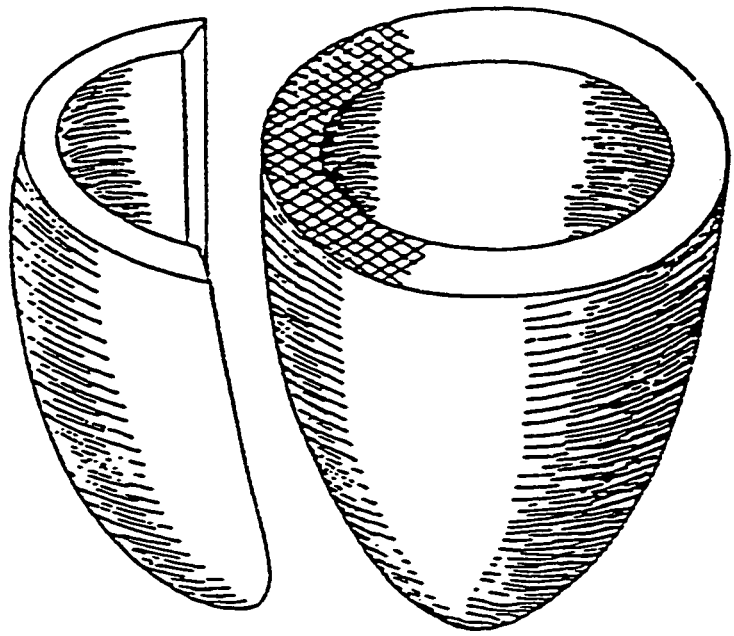

Figure 1.1 Illustration of the traditional view of the ventricles. The RV wraps around approximately one-third of the comparatively thicker LV. The zone of the interventricular septum is defined by the cross hatching.[138]

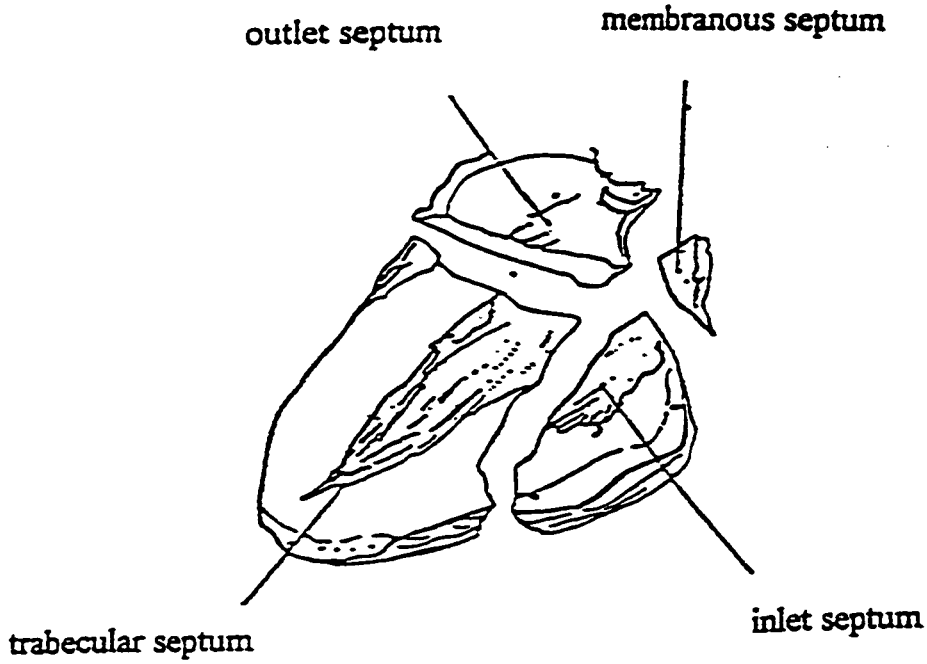

Figure 1.2 The interventricular septum viewed from the LV after division into its membranous and muscular (inlet, trabecular, and outlet) components.[6]

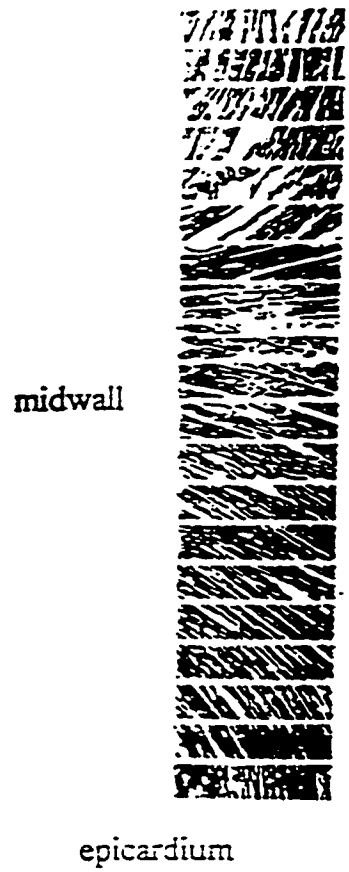

Figure 1.3 Orientation of muscle fibres across the LV free wall (endocardium, interior surface of the ventricle; epicardium, exterior surface of the ventricle). The middle 60% have a nearly circumferential fibre orientation, with fibres becoming increasingly oblique on either side of this central zone.[145]

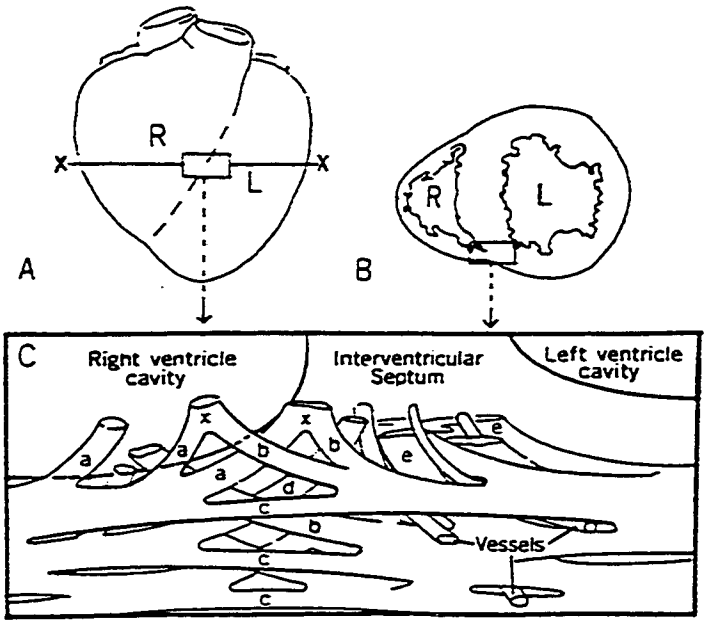

Figure 1.4 Bifurcation of myocardial fibres at anterior interventricular sulcus, regions shown by *box* in A. B: cross section of A (X —— X). Region shown in box in A is also shown in B. C: details of typical fibre branchings in box shown in A and B. a, RV fibre groups branching into RV trabeculae, x; c, superficial fibre paths of the RV and LV walls; d, fibre groups from RV wall branching into septum; e, fibre groups from LV wall branching into septum.[42]

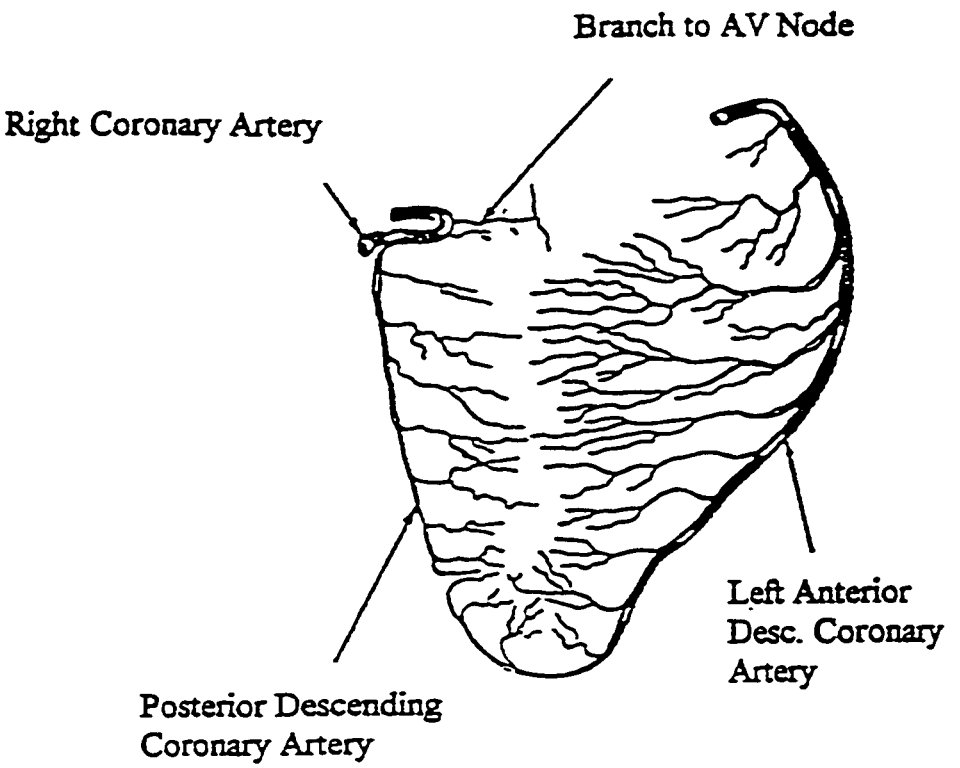

Figure 1.5 Schematic diagram depicting the coronary arteries responsible for blood supply of the normal human interventricular septum.[69]

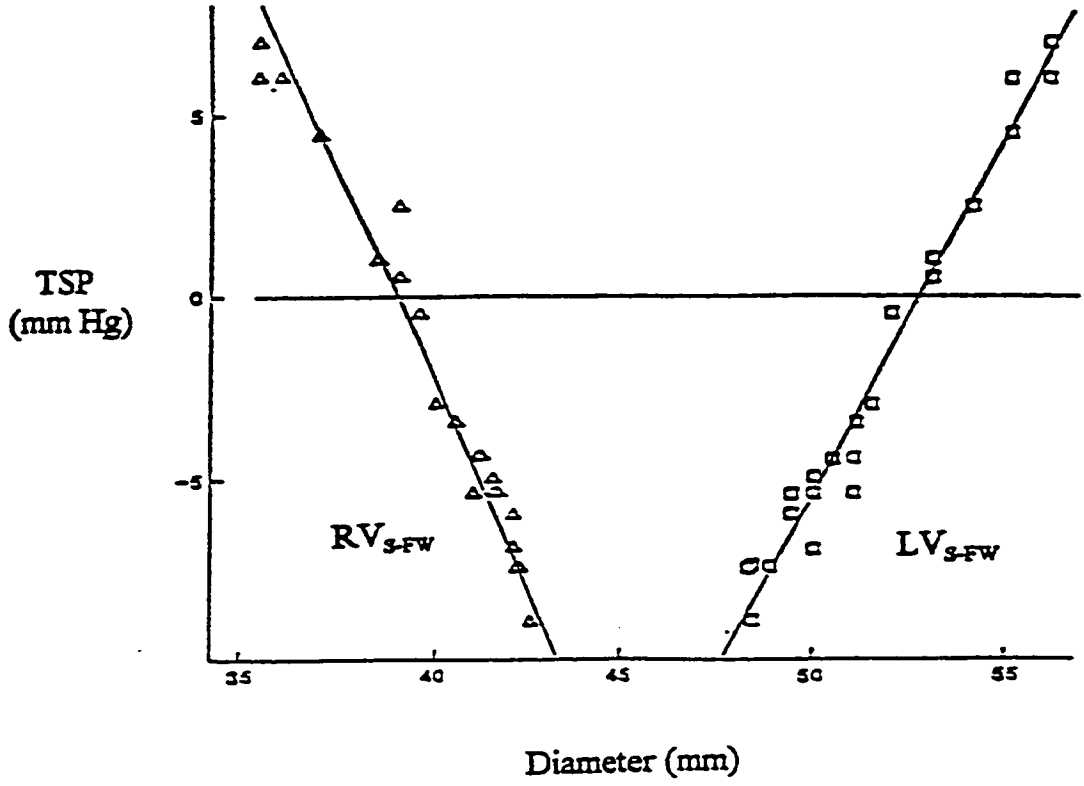

Figure 1.6 Plot of transseptal pressure (TSP) gradient and end-diastolic RV (triangles) and LV (squares) septum-to-free wall (S-FW) diameters.[78]

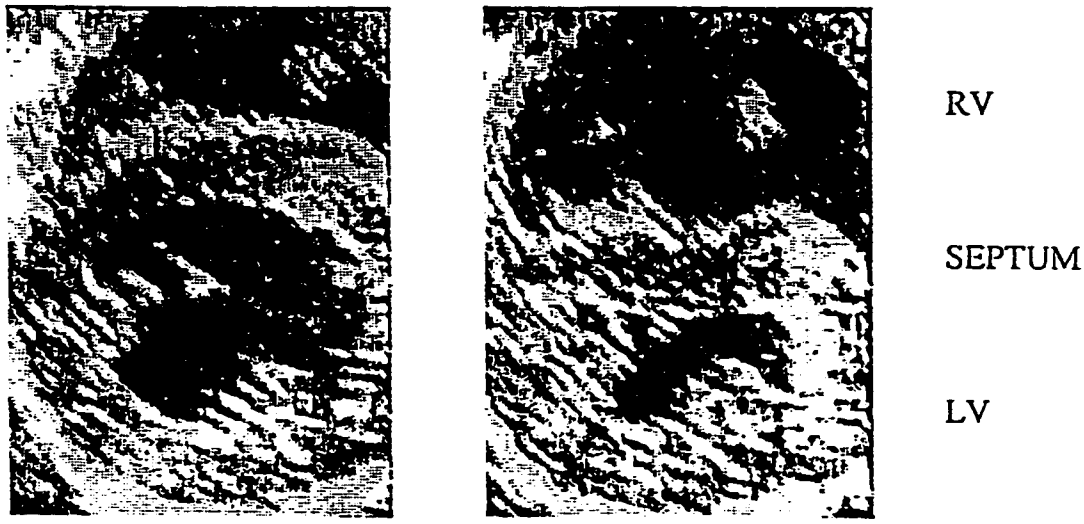

(a) Control (b) PA constriction

Figure 1.7 Cross-sectional echocardiograms of the heart during both control (a) and PA-constriction (b) loading conditions in diastole.

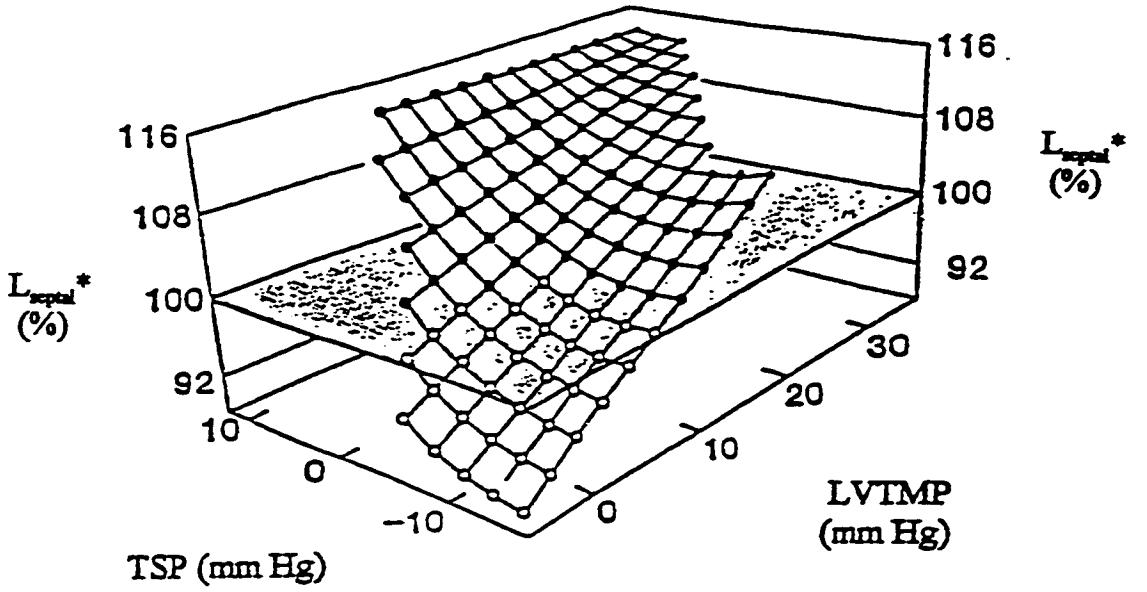

Figure 1.8 3-D plot showing the combined effects of the transseptal pressure (TSP) gradient and the LV transmural pressure (LVTMP) on segment length of the interventricular septum (L_{septal}*: normalized to unstressed L_{septal}, i.e., L_{septal} when both LVTMP and TSP were zero).[33]

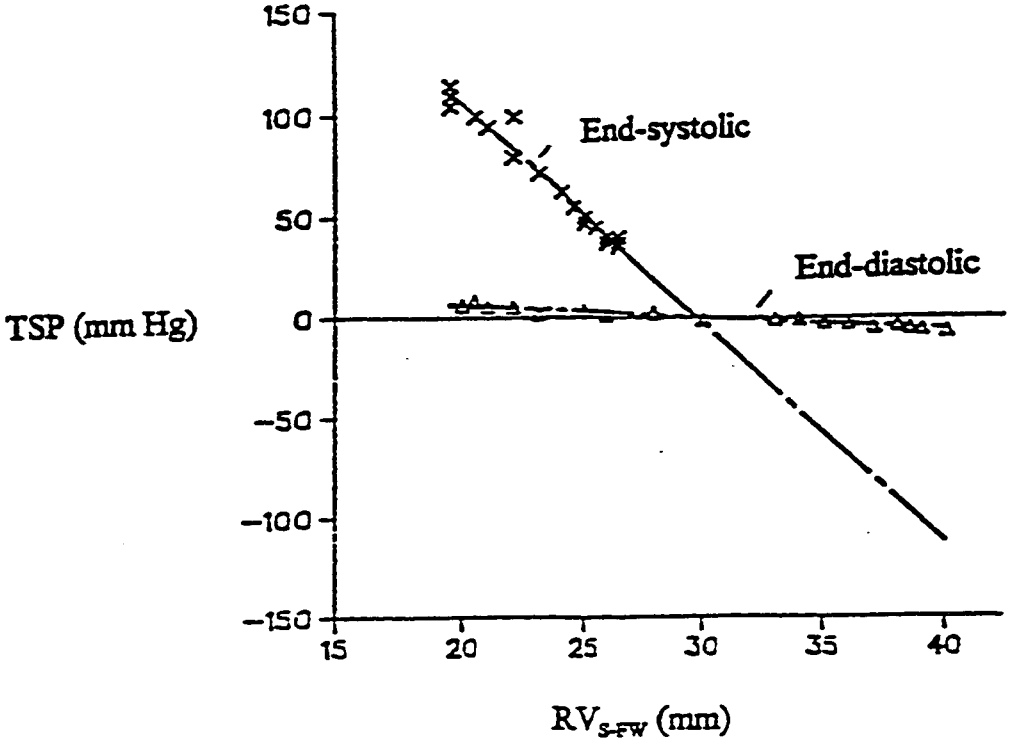

Figure 1.9 Plot of transseptal pressure (TSP) gradient and end-diastolic (triangles) and end-systolic (crosses) RV septum-to-free wall (S-FW) diameters.[138]

CHAPTER 2

ANALYSIS OF STRESS IN THE HEART

Various analytical and finite element models which researchers have used in attempts to quantify ventricular wall stress are reviewed. The goal is not to provide an exhaustive list of all models developed to date, but rather, to give the reader a frame of reference within which the model and results described in this dissertation can be compared.

2.1 Wall Stress and Cardiac Function

A fundamental requirement for the assessment of cardiac function in both health and disease is knowledge of the distribution of stresses in the walls of the heart.[25] Since Woods[163] began studying tension in the walls of the LV just over a century ago, characterization of forces and stresses in the heart has been of great interest to clinicians, physiologists, and biomedical engineers.[164] This interest derives from: (i) Ventricular wall stress has been postulated to have a bearing on coronary blood flow[70,98,142] and (ii) has been shown to be a primary determinant of underlying oxygen demand.[16,132] (iii) An accurate description of stress (and strain) across the ventricular wall is required in order to interpret the localized contractile disorders caused by myocardial infarction[17,18] and ischemia[84,150] successfully. (iv) Alterations in wall stress, which accompany diseases characterized by abnormal loading of the heart, influence growth and hypertrophy of the ventricular wall.[5,43,99] (v) There is a growing desire to "bridge the gap" between isolated muscle mechanics and the mechanics of the intact heart. With respect to this, Yin[51] has stated:

> "The tension-velocity-time relationships of isolated cardiac muscle form the cornerstone of our understanding of cardiac muscle mechanics.[100,119,140,141] For example, the load dependence of shortening, the length dependence of tension

development, and the contractility are thought to be intrinsic properties of heart muscle. In the intact heart, many different measures, most of which are based on pressure and volume or derivatives of these, have been proposed to characterize its function.[36,128] The function of the intact heart must in the end be referable to the function of the muscle which comprises the wall. However, to bridge the gap from isolated muscle mechanics, where stresses and deformations are well defined, to the intact heart is difficult because of the complex structure of the ventricular wall, its highly nonlinear material properties, the large deformations involved, the complex geometry of the ventricle, and the inherent difficulty in accurately measuring most of these parameters."

2.2 Measurement of Wall Stress *In Vivo*

Although preferable (to the calculation of stress), measurement of wall stress *in vivo* is not practical.[25] Attempts to measure wall force in the intact heart using strain-gauge transducers coupled directly to the myocardium have not been entirely successful.[22,38,51,58,64,65,85,93,124,164] Huisman et al[64] investigated the reliability of such techniques and showed that errors as high as 50% could easily be obtained. They concluded that the uncertainty was related to the degree of coupling between the transducer and the ventricular wall and that there did not appear to be a simple way to correct for these errors. Recently, however, Halperin et al[55] have developed a dynamic indentation system (which requires minimal surface contact) whereby in-plane stresses are estimated from the ratio of indentation stress to indentation strain (transverse stiffness).

2.3 Thin- and Thick-Walled Models Used to Calculate Ventricular Wall Stress

Many early attempts[23,37,129,130,159,163] to calculate ventricular wall stress were based

on LaPlace's law,[82] which relates the pressure inside a membrane to the radii of curvature and wall tension (analogous to the stress in a structure which has no thickness[164]):

$$P = \frac{T_1}{R_1} + \frac{T_2}{R_2}$$

where R_1 and R_2 are the two principal radii of curvature and T_1 and T_2 are the principal wall tensions. (It should be noted that although developed by LaPlace, this relation was in fact suggested a year earlier by Young,[168] and is sometimes referred to as the Young-LaPlace law.)

Woods[163] used LaPlace's law, and assumed spherical geometry for the heart (i.e., $T_1 = T_2$; $R_1 = R_2$) thus expressing ventricular wall tension as a function of the internal pressure and radius:

$$T = \frac{PR}{2}.$$

This model, although simplistic, has provided some important insight into the mechanics of the heart.[164] Woods[163] hypothesized that, because tension is directly proportional to radius, the *trabeculae carneae* reduced the tension on each fibre in the wall since the local radius of the *trabeculae* is somewhat less than the chamber radius. Burton[23] used Woods' approach to explain the great variation of thickness in the ventricular wall. He indicated that in regions of the LV characterized by high curvature (i.e., small R), such as at the apex,

the wall can be thin and still produce sufficient tension to develop enough intracavitary pressure, because the tension is at a "mechanical advantage." However, midway up the free wall, where the curvature is much less (i.e., high R), the tension developed must be much greater to produce the same intracavitary pressure, and hence the wall must be correspondingly thicker.

Sandler and Dodge[129] and Sandler and Ghista[130] modelled the LV as a thin-walled ellipsoid and emphasized stress rather than tension because of the finite thickness of the ventricular wall. Rewriting LaPlace's law in terms of stresses, they obtained:

$$\frac{P}{t} = \frac{\sigma_{long}}{R_1} + \frac{\sigma_{circ}}{R_2}$$

where σ_{long} is the longitudinal or tangential stress, σ_{circ} is the circumferential or hoop stress, R_1 and R_2 are the principal radii of curvature, and t is the wall thickness. For semi-major and semi-minor axis dimensions of a and b respectively, the expressions for the stresses are given by:

$$\sigma_{long} = \frac{Pb}{t}\left[\frac{b}{2b+t}\right]$$

and

$$\sigma_{circ} = \frac{Pb}{t}\left[1 - \frac{b^2}{a^2}\left(\frac{b}{2b+t}\right)\right].$$

When a is equal to b (such as for a sphere), σ_{long} should equal σ_{circ}. However, for the above two expressions, this is not true, except when $h << b$, i.e., the expression for σ_{circ} is based on the assumption that the ventricular wall is negligibly thin.[164] Falsetti et al[37] and Walker et al[159] presented the correct derivation of σ_{circ} as:

$$\sigma_{circ} = \frac{Pb}{t}\left[\frac{2a^2 - b^2}{2a^2 + bt}\right].$$

Thin-walled membrane models (such as those just described), while attractive from a computational standpoint, are based on rather limiting assumptions: (i) They are based on a global force balance (i.e., LaPlace's law) and therefore knowledge of material properties is not required [51] It follows, then, that thin-walled models implicitly assume the ventricular myocardium to be homogeneous and isotropic. (ii) Small deformation theory is assumed (i.e., strains of less than 1.0%).[165] (iii) Thin-walled models only predict the stress acting in the plane of the surface; this stress is either circumferential or longitudinal in direction (i.e., there are no radial or transverse shear components, therefore also no bending stresses).[164] (iv) The stresses which develop are due to internal pressure loading only, and computation is based on the instantaneous pressure and geometry (i.e., quasi-static analysis).[25] (v) In order for thin-walled approximations to be valid, the thickness-to-radius ratio should be less than 1:10.[164] For an LV with an internal diameter of 5 cm and thickness equal to 1 cm, the thickness-to-radius ratio is 1:2.5. Strictly speaking, then, thin-walled models are not appropriate for analysis of the LV (and septum). (vi) Finally, the transmural variation in

stress, which is of interest to many investigators, cannot be obtained with these formulations. Thin-walled models only predict the average stress across the wall thickness.[51] For a more extensive review of the limitations of LaPlace's law, see Moriarity.[105]

Only 60 years after the development of LaPlace's relation did Lamé predict a variation in radial stress across the wall of a pressurized thick-walled sphere.[81] Wong and Rautaharju[162] modelled the LV as a thick-walled ellipsoid with linearly elastic material properties. Although their formulation included many of the assumptions described for the thin-walled models, they were the first to show a variation in stress across the wall of the LV. Figure 2.1 shows the general trend of their results, that the calculated stresses (circumferential, longitudinal, and radial) decreased from endocardium to epicardium.

Ghista and Sandler[45] modelled the LV as a thick-walled quasi-ellipsoid. The ventricular myocardium was assumed to be homogeneous, isotropic, and linearly elastic; they also allowed for incompressibility. The distribution of stress components across the wall was similar to that described by Wong and Rautaharju.[162] Shear stresses, however, could be accounted by the model, but only because of the inexact geometry (i.e., the model was not mathematically an exact ellipsoid).[164]

Mirsky[96] modelled the LV as a prolate spheroid (ellipsoid of revolution) and assumed homogeneity, isotropy, linear elasticity, and incompressibility. Figure 2.2 shows the variation in stress calculated by Mirsky across the ventricular wall. The results are similar to those presented by Wong and Rautaharju[162] and Ghista and Sandler[45] except that the longitudinal stress at the equator increased rather than decreased from endocardium to

epicardium.

All the models just described have assumed that the myocardium behaves as an isotropic, homogeneous medium. However, as described in Chapter 1, Streeter et al[144,145,147] have shown that the muscle fibre direction varies across the wall of the ventricle. Streeter et al[146] developed a model based on the known fibre orientation and calculated the ventricular wall stress distribution at end-diastole and end-systole (see Figure 2.3). According to their results, for both end-diastole and end-systole, the peak circumferential stresses occurred in the mid-wall region (consistent with the finding that mid-wall fibres are circumferentially oriented) whereas the peak longitudinal stresses occurred in the outer regions of the wall (consistent with the fibres in the outer regions being oriented perpendicularly to those at the mid-wall). The radial stress distribution (not shown) was similar to that computed in the models[45,96,162] described above, suggesting an insensitivity to fibre orientation. It should be noted that Streeter et al[146] and others[39,154] have assumed that muscle fibres only carry axial tension. However, Demer and Yin,[31] and Yin et al[167] have shown that load may also be carried in directions transverse to the fibres.

Mirsky[97] extended the model of Wong and Rautaharju[162] and assumed a parabolic variation in circumferential elastic modulus[145] chosen to mimic the roughly parabolic variation in fibre angle proposed previously. As would be expected, the model predicted peak circumferential stresses at the mid-wall, consistent with the results of Streeter et al.[146]

Additional complexities which have not been included in the formulations described thus far, are large (finite) deformation theory (myocardial stretches as great as 20% or

higher during diastolic filling are thought to occur[51,101]) and the nonlinearity of cardiac muscle which has been previously described.[92,139] Mirsky[97] assumed spherical geometry for the LV and used large deformation theory to predict ventricular wall stress. Figure 2.4 shows that the circumferential stress distribution across the wall was markedly different depending on whether classic theory or large deformation theory was utilized. Furthermore, Mirsky[98] and Moriarity[105] have investigated the effect of nonlinear constitutive relationships on wall stress. In both studies, the endocardial wall stress (at diastolic pressure) calculated using nonlinear stress-strain properties was substantially higher than that when linear elastic material properties were assumed.

2.4 The Finite Element Method

Although thick-walled models may account for such complexities as muscle fibre orientation, large deformations, and nonlinear constitutive relations for the myocardium, these models are still relatively simple in that the LV geometry is approximated by using a simple geometric figure (e.g., sphere, spheroid, or ellipsoid) that is everywhere concave toward the LV cavity.[164] For these analytical models, this basic assumption is required such that mathematical governing equations can be derived and solutions can be obtained.[25] When studying more complicated geometry, however, particularly those involving complex changes in curvature (e.g., flattening and inversion of the interventricular septum which is discussed in Chapter 1), a more complex method must be employed.[164] Because we particularly wanted to study such complex changes in curvature, we chose the finite-element

method of analysis.[169]

Solution of the mechanics of a continuous structure by discretization (i.e., subdivision) of the structure into a finite number of well-defined components was suggested as early as 1906, when researchers modelled an elastic body with a lattice of elastic bars and employed frame analysis methods.[26,51] It wasn't until the late 1950's, however, with the advent of high-speed digital computers, that use of the FE method became widespread, particularly as need for analysis of complex problems in the aerospace industry arose (e.g., Turner et al[156] and Argyris[7]).[164] FE analysis was soon adapted by the biomechanics community because it offers a general procedure of numerical approximation for the solution of physical problems whose "closed form" solutions are often impractical.[25,170] (A more detailed description of the FE method will be provided in Chapter 4.)

2.5 FE Analysis of Ventricular Wall Stress

Gould et al[47] and Janz and Grimm[71] in 1972, were the first to employ the FE method for analysis of stress in the LV. Using single plane, antero-posterior projections of ventriculograms to approximate geometry, Gould et al[47] constructed a 3-D FE model of the LV comprised of 13 shell ring elements (irregular shell chambers of revolution obtained by revolving each half of the irregular geometry of the LV). Bending and transverse shear stresses were taken into account, the effects of the RV were ignored (i.e., LV pressure loading only), and the myocardium was assumed to be linearly elastic. This study showed an important result which would not have been obtained had the LV been approximated by

a simple geometric figure (as is the case with the earlier analytical models described above): the linear distribution of both the circumferential and longitudinal tensile stresses across the wall thickness reversed in regions of the wall whose curvature changed signs.

Janz and Grimm[71] modelled the LV of a rat (the geometry was approximated using serial sections obtained *in situ* after potassium arrest and formalin fixation) using 198 quadrilateral ring elements. Like Gould et al,[47] they assumed linear elasticity for the myocardium, and ignored the effect of fibres, but attempted to account for heterogeneity of wall structure. They made the inner third of the ventricular wall transversely isotropic (to model the effect of sinusoidal interstices in the endocardial surface) while making the outer two thirds isotropic. Close agreement between model-derived deformations and measured deformations was obtained up to diastolic pressures of approximately 9 mm Hg. Above this level, however, model-derived deformations were greater than those which were measured and it was postulated that the discrepancy was a result of not incorporating a nonlinear stress-strain relationship into the model. Further comparison between the deformations predicted by the heterogeneous model and those of a completely isotropic model revealed that heterogeneity of wall structure contributed marginally to the model (the isotropic model predicted deformations at the equator which were 8% less than those predicted by the heterogeneous model). The authors extended their model to allow for a nonlinear material relationship,[164] and compared the predicted deformations when nonlinear material properties were included in the model and when they were ignored, i.e., when linear elasticity was assumed (no attempts were made to compare predicted and

experimentally measured deformations in this study). Figure 2.5 shows that above diastolic pressures of approximately 4.5 mm Hg (i.e., 6 cm H_2O), the predicted diastolic pressure-volume curves ceased to match, implying that a stiffening of the chamber above this value was accounted for by the nonlinear model.

Janz et al[72] demonstrated the effect of allowing for nonlinear geometric effects when modelling the LV. Their model was axisymmetric, heterogeneous, and nonlinearly elastic, but also allowed for large deformation theory by retaining the nonlinear terms in the strain-displacement relations. Their model showed that incorporation of such nonlinear geometric effects (see Figure 2.6) produced a lower chamber stiffness (opposite to what occurred when nonlinear material properties were assumed) than when these effects were ignored, i.e., when small deformation theory was employed.

Pao et al[113] modelled the LV using triangular cross-section ring elements, in a manner similar to Gould et al,[47] but allowed for variable wall thickness. Unlike Gould's model (and other uniform thickness models[45,96,162]) which predicted a roughly linear variation in stresses across the wall, this model demonstrated a nonlinear variation of stresses across the wall.

Panda and Natarajan[111] modelled the LV using thick-shell elements and investigated the effects of fibre orientation on ventricular wall stress. Fibre directions in the inner, middle, and outer wall were assumed to be 40, -5, and -50 degrees respectively (measured from horizontal). The myocardium was assumed to be linearly elastic, but they assumed that the material properties along the fibre direction were transversely isotropic and that the

transverse properties were a percentage of those in the fibre direction. Circumferential stress values predicted by the model in the *absence* of fibres were higher than those reported by previous investigators using closed form solutions in the absence of fibres,[45,96,162] but the longitudinal stress values were lower. When fibres were accounted for, mid-wall circumferential stresses increased, while longitudinal endocardial and epicardial stresses decreased as the ratio of stiffness in the fibres (longitudinal vs. transverse) increased.

The sampling of FE models just described illustrate the effects of heterogeneity of wall structure, finite deformation theory, and fibre orientation on ventricular wall stress. More recent three-dimensional models[27-29,50] have included in their design these effects, but, just as those models described above, these models neglect the effect of the RV on the loading of the LV chamber, and thus, by definition, ignore the septum. The next two studies are of particular relevance to this dissertation, as they support the idea, perhaps first suggested in the study of Gould et al (see above),[47] that stress patterns are highly dependent on local ventricular wall curvature.

Using a 3-D reconstruction technique, Heethaar et al[57] studied the stress gradients in both a single LV and in a combined RV and LV model (7000 tetrahedral elements were used and the myocardium was assumed to be isotropic, homogeneous, and linearly elastic). As described previously, the circumferential stresses in the single LV model were highest at the endocardium and decreased transmurally. In the combined ventricle model, the largest stresses were also found at the endocardium. Slight compression was also found in

the septum – a result which had not previously been predicted.[164]

Pao et al[114] used 308 triangular plane-strain elements to model a cross section of an isolated LV in diastole reconstructed from roentgenographic recordings (use of plane-strain elements implies the LV is a long irregular cylinder). Although the myocardium was assumed to be homogeneous, isotropic, and linearly elastic, some very interesting results were obtained. Endocardial to epicardial circumferential stress gradients (as predicted by the axisymmetric models) occurred only in the anterior and posterior walls. In the septum (although the RV was not connected, curvature of the septum was taken into account) and LV free wall, the gradient was reversed, but of smaller magnitude. Furthermore, the model showed that some circumferential compressive stresses developed near the LV-septal surface (i.e., the LV endocardial surface of the septum) where the wall curvatures were small or convex inward.

As emphasized in Chapter 1, TSP is normally positive during diastole and the septum seems anatomically and functionally a part of the LV. However, under conditions such as pulmonary hypertension, TSP decreases and may become negative. The septum may then flatten or invert. At present, the septum is generally considered by most cardiologists and cardiac physiologists to be an unstressed membrane (in contrast to that shown by Heethaar et al[57] and Pao et al[114]), in that its position is assumed to be determined primarily by the TSP.[78,86,148,151] However, the shape of the distorted septum suggests a more complex behaviour, specifically that of a thick-walled structure subject to lateral pressure and end-bending moments. The goal of the dissertation described herein was to provide a

comprehensive FE analysis of the septum under both control and PA-constriction loading conditions during diastole (no other study of this kind exists), and, to test the hypothesis that, secondary to PA constriction, substantial compression and bending moments develop in the septum.

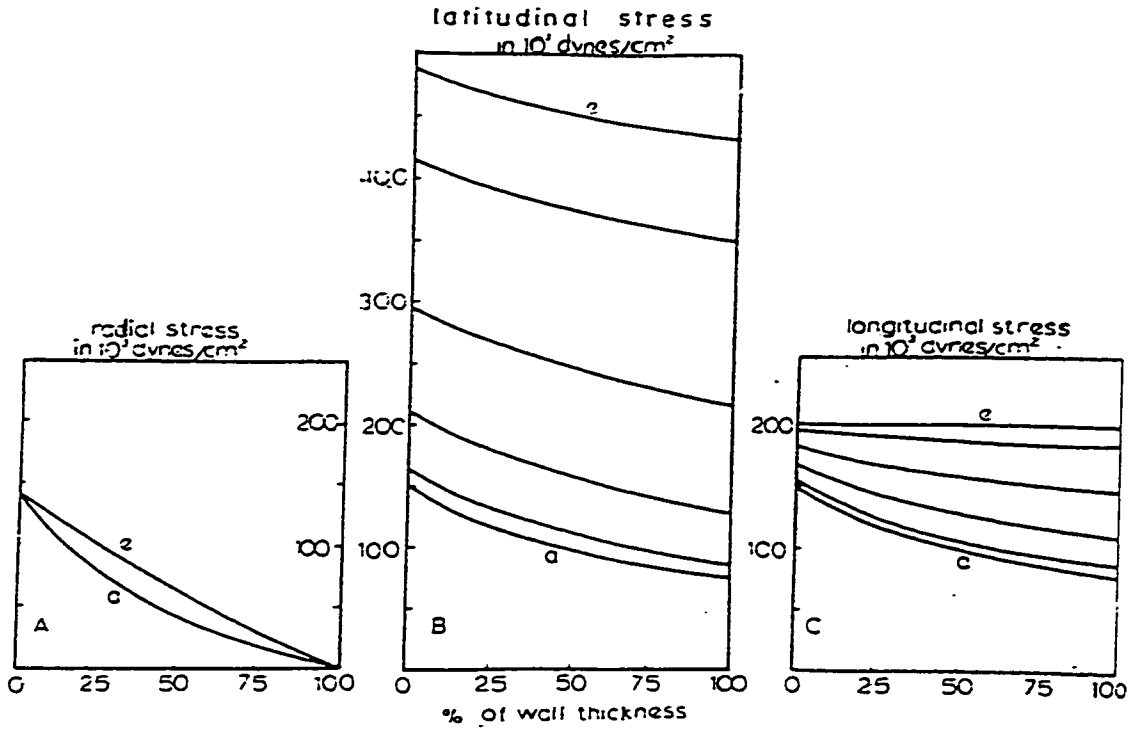

Figure 2.1 Distribution of radial, latitudinal (i.e., circumferential), and longitudinal stress from endocardium (0%) to epicardium (100%) in the wall of an ellipsoidal ventricle. The curves show the stress profiles at the equatorial (*e*) and apical (*a*) cross sections and at five intermediate sections between apex and equator. The values were computed for an intraventricular pressure of 144 (10^3) dynes • cm^{-2} (approximately 110 mm Hg), wall thickness of 7.3 mm, and the ratio of major axis to minor axis = 2.[162]

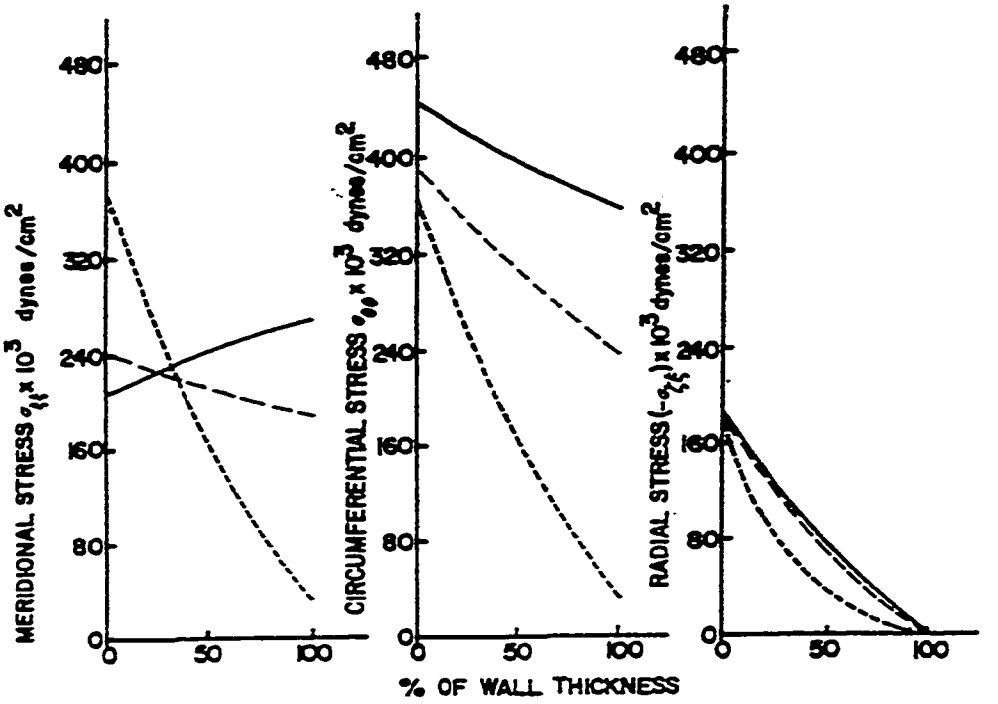

Figure 2.2 Stress distribution in the myocardium based on a thick-walled model. Solid line: at the equator; dotted line: at the apex; dashed line: approximately mid-way between the equator and the apex.[96]

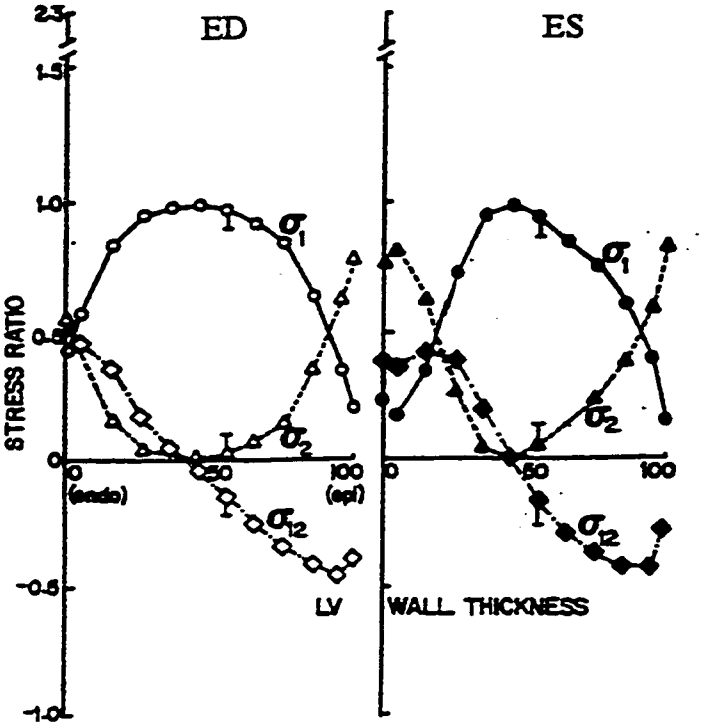

Figure 2.3 Myocardial wall stress distribution at end-diastole (ED) and at end-systole (ES) computed with fibre orientation incorporated in the model: σ_1 - circumferential stress; σ_2 - longitudinal stress and σ_{12} - shear stress in the longitudinal direction in a plane perpendicular to the circumferential direction.[146]

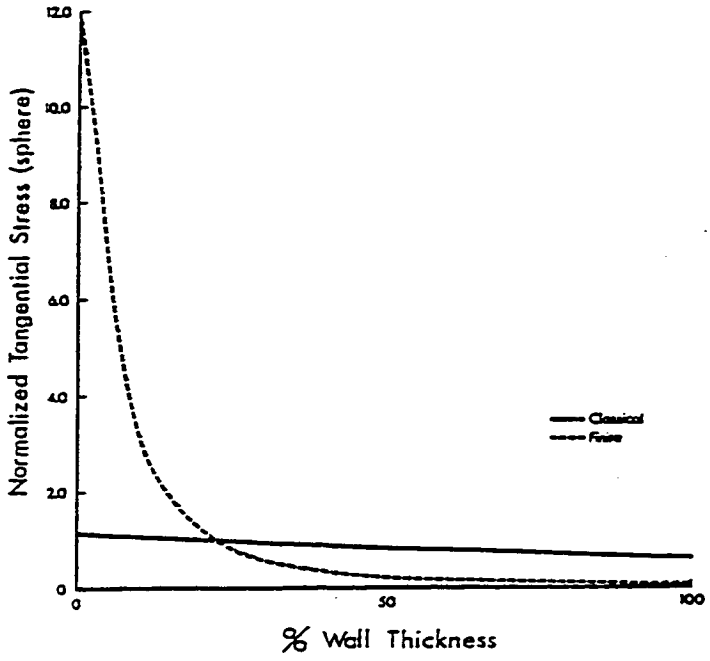

Figure 2.4 Tangential (i.e., circumferential) stress (normalized to the LaPlace stress), based on classical theory (i.e., small deformation theory) and finite deformation theory (i.e., large deformation theory) is shown plotted as a function of wall thickness (0% - endocardium; 100% - epicardium).[97]

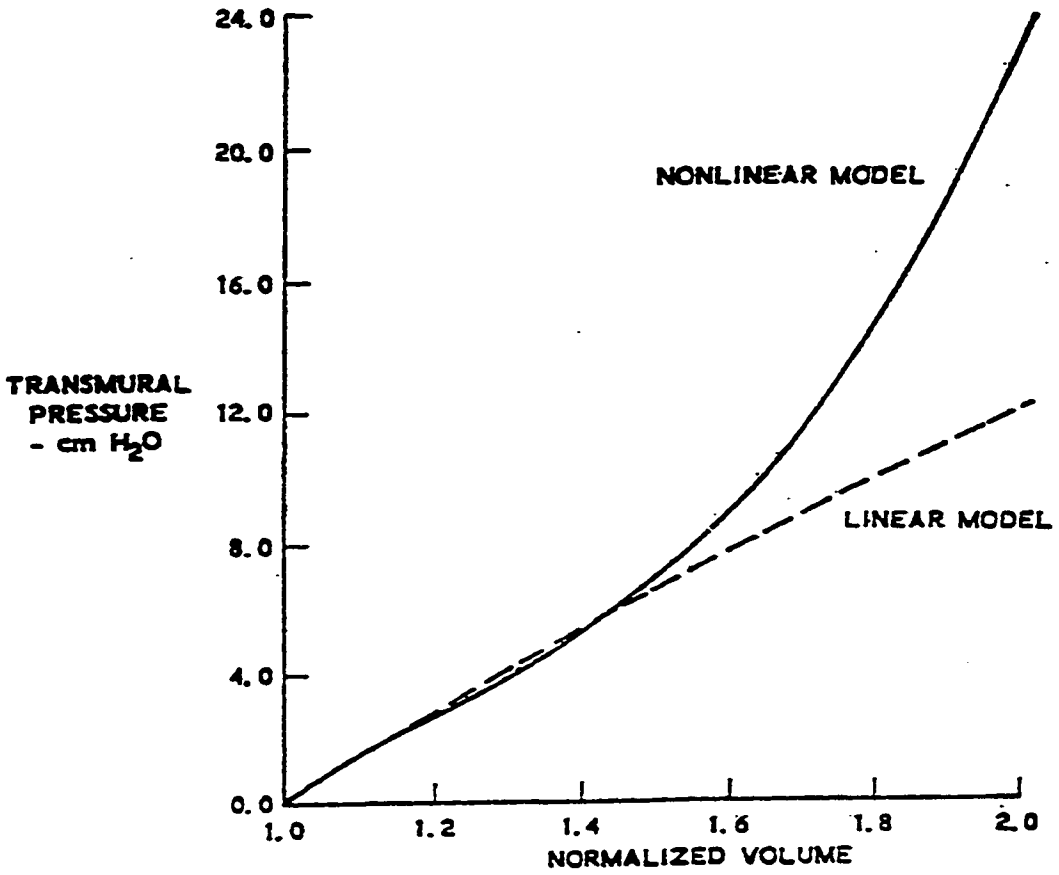

Figure 2.5 Comparison of the passive pressure-volume curves predicted by a finite element model when the material of the wall was composed of nonlinear (i.e., exponential relationship between stress and strain) as compared with a linear constitutive relationship.[71]

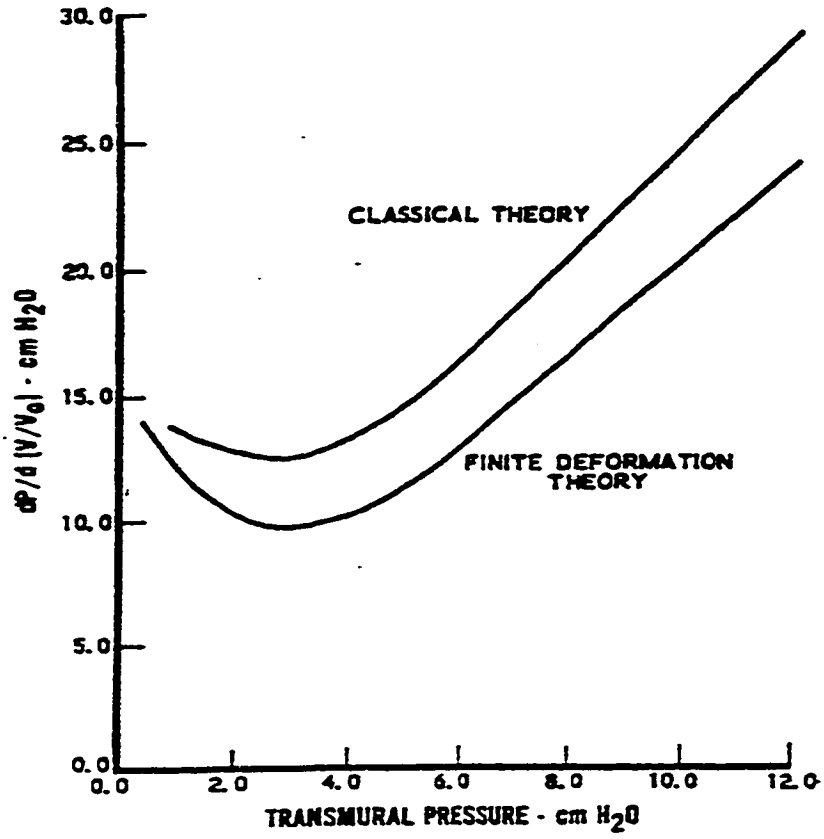

Figure 2.6 Comparison of the chamber stiffnesses expressed as a function of the pressure when classical theory (i.e., small deformation theory) vs. finite deformation theory (i.e., large deformation theory) was used for a finite element model.[72]

CHAPTER 3

EXPERIMENTAL METHODS

3.1 Animal Preparation

Six mongrel dogs of either sex were anaesthetized, initially with sodium thiopental (25 mg • kg^{-1} i.v.) and subsequently with an infusion of fentanyl citrate (25 mg • kg^{-1} • hr^{-1}), intubated, and ventilated (70% nitrous oxide-30% oxygen mixture) using a constant-volume respirator (model 607, Harvard Apparatus, Millis, Mass.). A large-bore cannula was introduced into the external jugular vein for administration of fluids. A midline sternotomy was performed, and the ventrolateral surface of the pericardium was incised transversely (~5 cm long) along the base of the heart and retracted for instrumentation.

To manipulate TSP (and achieve septal flattening and inversion), an inflatable silicone occluder (In Vivo Metric, Healdsburg, Calif.) was placed around the main PA. To measure pericardial pressures, flat liquid-containing Silastic balloons (3 x 3 cm) were tethered by two individual sutures to the anterolateral surface of the RV and the lateral surface of the LV.[135,136] Each balloon had a 3-F micromanometer-tipped catheter (model SPR-524, Millar Instruments, Houston, Tex.) positioned internally to provide a high-fidelity measurement of balloon pressure (diminishes sensitivity to artifacts and oscillations generated from transmission and catheter motion).[56] Calibration curves for both balloons were described before and after each experiment using techniques developed by McMahon et al.[94] The heart was then repositioned into the pericardium, and the pericardial margins were reapproximated with several sutures, taking care to avoid decreasing the pericardial volume.[135]

LV and RV pressures were measured with 8-F micromanometer-tipped catheters

with reference lumina (model SPC-485, Millar Instruments, Houston, Tex.) inserted through a carotid artery and internal jugular vein, respectively. A liquid-filled catheter was inserted into the aorta via a femoral artery to monitor pressure. The liquid-filled catheters were attached to transducers (model P23 ID, Statham Gould, Inc., Oxnard, Calif.) and referenced to the level of the right atrium. Before each data collection, pressures measured by the micromanometers were matched to those measured from the liquid-filled catheters to correct for baseline drift. After surgical preparation, the animals were allowed to stabilize for 30 min. Throughout the experiment, body temperature was maintained by a heating pad, and the ECG (lead II) was recorded to monitor cardiac rhythm and rate. All conditioned hemodynamic signals were amplified (model VR16, Electronics for Medicine/Honeywell, White Plains, N.Y.), passed through a low-pass filter (100 Hz), and digitized at 200 Hz.

3.2 Echocardiographic Frame Acquisition

The interventricular septum was imaged (30 frames • s^{-1}) echocardiographically (Diasonics V3400, Salt Lake City, Utah) in an LV minor-axis view (at the level of the tips of the papillary muscles) using a 5.0 MHz transesophageal probe held on the surface of the RV free wall. A video frame synchronizer (Odessa Computer Systems, Calgary, Alberta, Canada) was used to match the echocardiographic frames (recorded on ½-in. videotape) to be analysed with the corresponding hemodynamic data.

3.3 Experimental Protocol

Hemodynamic and echocardiographic data were obtained simultaneously and continuously for 30 s (including a 10-s control period) with the respirator turned off to eliminate the effects of respiration. Attempts were made to obtain complete flattening or inversion of the septum in each PA-constriction run. Between interventions, an interval of 10 to 15 min was allowed to elapse for hemodynamic stabilization.

3.4 Hemodynamic Data Analysis

The hemodynamic data were subsequently analysed using commercial software (CVSOFT, Odessa Computer Systems).

3.5 Echocardiographic Frame Analysis

Using image-analysis software developed in our laboratory (CVIMAGE5, Odessa Computer Systems), septal mid-wall points were identified (see Figure 3.1). By connecting these points and smoothing,[4] a mid-wall line was constructed. From this line, radius-of-curvature measurements could be made. Finally, thickness (normal to the mid-wall line) and the insertion-point length (L_{IP}) were measured.

3.6 Statistical Analysis

In this dissertation, the hemodynamic and geometric data were plotted (using SigmaPlot 3.0 for Windows, Jandel Scientific, San Rafael, Calif.) as a function of time in

order to illustrate the general trends of these parameters during and between control and PA constriction. Because many of these parameters were used as inputs to the model, statistical testing was not performed in these situations. However, for certain output values, one-way repeated-measures ANOVA (analysis of variance) was performed in order to determine if differences in the values between the two loading conditions were statistically significant. All statistical testing was performed using SigmaStat 2.0 (for Windows) statistical software (Jandel Scientific, San Rafael, Calif.) on a Pentium 166 IBM clone computer. A probability of less than 0.05 was considered to be statistically significant. Finally, some data were expressed in tabular form, as the mean plus and minus the standard deviation (SD).

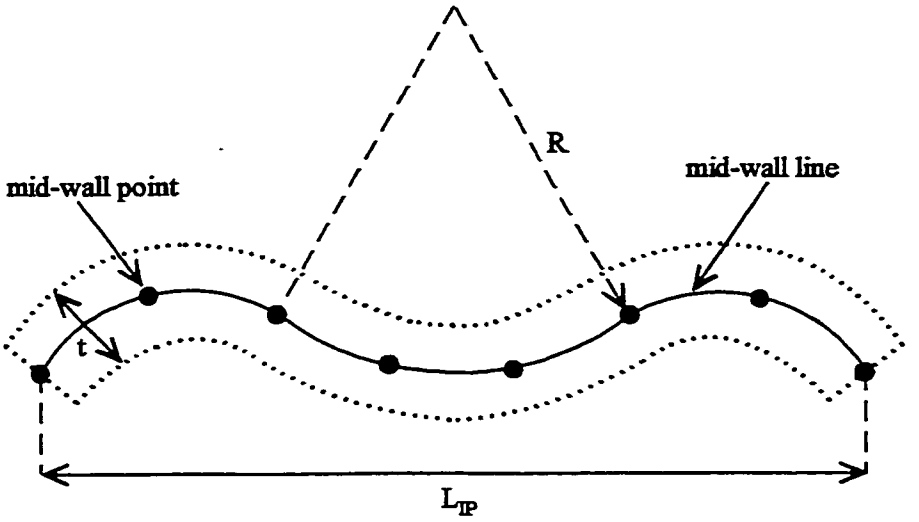

Figure 3.1 Geometric analysis of the interventricular septum. Septal mid-wall points were first identified. By connecting these points and smoothing, a mid-wall line was constructed. From this line, radius-of-curvature measurements (R_{septal}) were made (in this instance, for an inverted septum, three were required). Finally, thickness (t, normal to mid-wall line) and insertion-point length (L_{IP}) were measured.

CHAPTER 4

FE MODEL AND FE ANALYSIS DESCRIPTION

4.1 Use of the FE Method to Model the Interventricular Septum

When faced with the challenge of analysing the mechanics of the interventricular septum during PA constriction, the question arises: which method should one use? The answer to this question becomes apparent if one considers the complexity of deformation and uniqueness of loading which the septum undergoes during PA constriction. Figure 4.1a shows a schematic diagram of a cross-sectional (minor-axis) view of the heart during PA constriction. When TSP becomes negative, the septum (dashed lines) flattens and may invert, moving leftward towards the centre of the LV cavity. Even though thick-walled models have incorporated large deformation analysis, effects of fibre orientation, and nonlinear constitutive relations for the myocardium, a basic assumption is still inherent in these models: a simple geometric figure must be assumed for the ventricle in order to keep the mathematical equations tractable.[25] It follows then, that flattening and inversion of the septum, as occurs in Figure 4.1a, immediately precludes any thick-walled theory from being used for analysis of this structure. Furthermore, Figure 4.1b shows a free-body diagram of the septum which illustrates the complex loading of the septum during PA constriction. Not only is the septum subject to both LV and RV pressures, but also to end-bending moments, and shear and axial forces at the RV-insertion points. The RV free wall also exerts tension at the insertions, an effect which is undoubtedly increased with increasing RV pressure (it is possible that the RV free wall also applies shear forces and bending moments at the insertions, if treated as a thick-walled, rather than thin-walled, structure). Because of the complex geometry and loading of the septum, particularly that which occurs during PA

constriction, the FE method of analysis was chosen to model the septum.

4.2 FE Method Description

Before describing in detail the FE mesh and constitutive relations which have been employed to model the interventricular septum in this dissertation, a general description of the FE method is outlined below (for a detailed description of the method, see Zienkiewicz[169]):

(i) Figure 4.2a shows a planar structure subject to a specific loading condition.[25] The structure is discretized (divided) into a "finite" number of smaller regions, called "elements" (see Figure 4.2b), which are joined to one another by "nodes" (only corner nodes are shown, depending on the type of element used, nodes can also join elements at mid-regions). The FE method contrasts with the continuum approach where concepts of stress and strain are defined at a "point," and the material is assumed to be continuously the same for the entire entity. Through discretization, the FE method attempts to overcome the intractability of many continuum problems, whereby a satisfactory approximation to the continuum solution is desired.

(ii) The FE method uses the so-called *stiffness* method of solution. Element equations are derived in terms of unknowns at the nodal points and are commonly expressed as:

$$\left[K_{element}\right]\{\delta\} = \{F\}$$

where $[K_{element}]$ is the element stiffness matrix, $\{\delta\}$ is the nodal deformation vector, and $\{F\}$ is the nodal force vector. Individual element stiffness matrices are constructed through numerical integration (Gaussian integration being the integration scheme of choice). For displacement-based elements (the most common, and the type used in the model described in this dissertation), shape functions (i.e., mathematical expressions) are specified which define the displacement of any point in the element given a unit displacement in one direction at one node.

(iii) The equations derived for each element are then assembled (according to the laws of compatibility and continuity) to generate the global governing equations (i.e., for the entire model) of the form described above.[19]

(iv) Boundary conditions are specified which describe how the body is supported in space.

(v) The governing equations are solved to yield nodal displacements using a computer-aided numerical solution technique.

(vi) By making use of the strains obtained in the solution (the derivative of the displacement function provides the strain) and the constitutive relationship assumed for the material, stresses in the elements are computed.[25]

4.3 FE Software/Computer Hardware

The FE program ABAQUS (version 5.6, Hibbitt, Karlsson & Sorenson, Inc., Pawtucket, R.I.) was used for all stages of the analysis and was run on a SGI computer

(Origin 2000, Silicon Graphics Inc., Mountain View, Calif.).

4.4 FE Mesh

The mesh consisted of 120 8-node (parabolic shape function) plane-stress elements (using 3x3 integration, i.e., 9 Gauss points for each element) arranged in 6 layers of 20 elements (see Figure 4.3). [Use of plane-stress elements implies that the only stresses which develop are those parallel to the plane (or surface) of the element, σ_x and σ_y. The stress perpendicular to the element plane, σ_z, is zero. Strains in all three directions (ε_x, ε_y, and ε_z), however, are permitted to develop.] Six truss elements were used at each boundary to allow for the application of end-bending moments, applied in the form of equal and opposite force couples. The truss elements were assigned a Young's Modulus of 2.0 MPa in an attempt to obtain rigid-body rotation about the mid-nodes (i.e., the equivalent of the RV insertion points) of each boundary (attempts were made to stiffen the truss elements even more, but numerical instabilities resulted).

4.5 Constitutive Relations

The potentially large (finite) strains associated with the PA-constriction cycle were partly accounted for by utilizing a model of hyperelasticity. Hyperelastic materials are described in terms of a strain-energy function which defines the strain energy stored in the material per unit of reference volume (volume in the stress-free natural state). For the simplest hyperelastic material, as used in ABAQUS, the strain energy, $U(\varepsilon)$, is defined by

the incompressible form of the neo-Hookean law:

$$U(\varepsilon) = \frac{G}{2}(\bar{I}_1 - 3)$$

where G is the initial shear modulus and $\bar{I}_1$ is the first deviatoric stretch invariant defined as

$$\bar{I}_1 = \bar{\lambda}_1^2 + \bar{\lambda}_2^2 + \bar{\lambda}_3^2.$$

The deviatoric stretches, $\bar{\lambda}_i$, are given by

$$\bar{\lambda}_i = J^{-\frac{1}{3}}\lambda_i$$

where J is the volumetric strain and λ_i are the principal stretches, related to the principal normal strains, ε_i, by

$$\lambda_i = 1 + \varepsilon_i.$$

$U(\varepsilon)$ can therefore be expressed in terms of G, J and ε_i, giving the form:

$$U(\varepsilon) = \frac{G}{2} J^{-\frac{2}{3}}[3 + 2(\varepsilon_1 + \varepsilon_2 + \varepsilon_3) + \varepsilon_1^2 + \varepsilon_2^2 + \varepsilon_3^2] - 3\frac{G}{2}.$$

4.6 Geometric Nonlinearity

To account for large deformation, geometric nonlinearity was included in the model.

Equilibrium equations are written with respect to the deformed geometry. Although equilibrium equations of the deformed configuration might be written for all problems, in so-called linear geometric problems, the original configuration may be used because the deformations are minimal.[26] In this case here, the effect of axial stresses on reducing the overall structural stiffness, (i.e., the "pδ" effect), was considered. In Figure 4.4, an axially loaded (p) column is subject to lateral load which produces an internal (primary) bending moment distribution (M_{pri}). The column deforms (δ) laterally under this loading, causing a secondary moment to develop – the axial applied load multiplied by the deformation, pδ $= M_{sec}$. M_{sec} in turn increases the deformation, δ. The column thus appears more flexible (the deflections are greater) than due to the primary loading alone. In traditional structural analysis, this effect is accounted for by increasing the primary internal bending moment by the secondary moment while keeping the structural bending stiffness (K_{bend}) constant. In the FE method, rather than keeping K_{bend} constant and determining M_{sec}, M_{pri} is kept constant and the structural stiffness matrix is reduced:

$$\left[K_{struct-red}\right] = \left[K_{struct}\right] - \{\sigma\}\left[K_{geom}\right],$$

where $[K_{struct}]$ is the structural stiffness matrix, $\{\sigma\}$ is the axial stress vector, $[K_{geom}]$ is the geometric matrix dependent on $\{\sigma\}$ and $[K_{struct-red}]$ is the reduced structural stiffness matrix.

4.7 FE Solution

An iterative technique based on the Modified Newton-Raphson procedure[169] was employed. The total load was added in increments and, for each increment, solution to a specified tolerance was achieved through iterations using the initial structural stiffness matrix.

4.8 Incorporation of Residual Stress

Many previous investigators have ignored the stress of completely relaxed, in-situ, ventricular myocardium. Figure 4.5 shows the hypothetical mesh (solid line) which represents an unloaded (LVP = RVP = 0 mm Hg) and unstressed septum. Equal and opposite force couples were applied at the ends of this mesh (resulting in initial end-bending moments, M_0) such that the resulting stress distribution closely matched (see Figure 4.6) that calculated by Guccione et al.[52] This mesh (dashed lines) is called a residually stressed, or RS mesh. The parameters of the calculated residually stressed state were saved to an input file and incorporated into each loading step in the form of an initial stress condition.

To solve most conventional structural problems, the FE method is implemented using known boundary conditions and material properties and then solving for the deformations and stress under load. Here the reverse is implemented – the "deformations" (as defined by the position of the septal mid-wall line) and loads (LVP and RVP) are measured, and therefore an *initial* RS mesh must be constructed which, when loaded, conforms to the observed configuration of the septum at end-diastole for the control cycle.

Therefore, the unknowns in determining the initial RS mesh are the shear modulus (G), the initial end-bending moments (M_0), and the shape of the unloaded, unstressed mesh.

4.9 Accounting for Sarcomere Length Changes during the Cardiac Cycle

So that images other than those at end-diastole could be analysed, the geometry of the initial RS mesh was adjusted according to values of sarcomere length (SL) idealized from the measurements of Rodriguez et al[125] and Guccione et al.[53] In the cardiac cycle, SL decreases during systole and increases in diastole. Hence, there was a requirement to adjust the geometry of the mesh to account for SL changes. It was assumed that SL increased a total of 17% from its end-systolic value to its end-diastolic value (see Figure 4.7, 15% linearly to the point of minimum LV pressure [due to rapid filling] and a further 2% linearly during diastasis and atrial contraction [due to passive filling]). Figure 4.8 illustrates the manner in which the geometry of the initial RS mesh was adjusted according to SL during the diastolic interval (i.e., adjusted in accordance with % reductions in SL). Note how both the radius of curvature and insertion-point length were changed when a change in SL was applied to the initial RS mesh.

4.10 Loading Conditions

Figure 4.9 shows examples for both the control and PA-constriction cycles. The RS mesh (adjusted for thickness and, for images other than those at end-diastole, for SL as well) was restrained (in both X and Y directions) at the mid-nodes of each boundary (i.e.,

the RV insertion points). The measured values of LVP and RVP were then applied. G and end-bending moments were adjusted until conformity to the observed configuration of the septum was judged to be satisfactory. (A "loading condition" is defined as an information set which describes the current geometry, G for the RS mesh, and the applied loads [LVP, RVP, and bending moments]).

4.11 Mesh Sensitivity Analysis

In order to help determine whether the results obtained from a particular FE model are meaningful, and not simply specific to the mesh selected, a mesh sensitivity analysis must be performed. Figure 4.10 shows a transseptal (mid-septum) circumferential stress (principal stresses obtained at the centroid) profile obtained from three different meshes under the same loading (PA constriction). Each mesh was 20 elements long but differed depending on the number of elements chosen to represent the thickness (3, 6, or 12). In general, the results (see Chapters 5, 6, and 7 for a detailed description of these results) obtained in all three cases were the same. However, the mesh with 3 elements across appeared to be somewhat crude with respect to the resolution of stresses across the wall, whereas the mesh with 12 elements across required 50% more convergence time (38 vs. 25 min) than the mesh with 6 elements across. Thus, the mesh with 6 elements across seemed the sensible choice to model the interventricular septum.

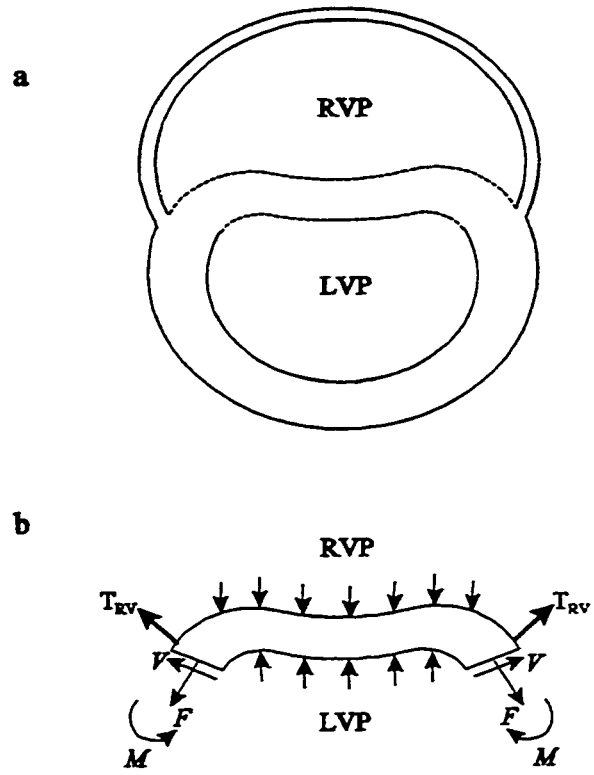

Figure 4.1 Schematic diagrams of (a) a cross-sectional (minor-axis) view of the heart during PA constriction and, (b) the loading on the septum during PA constriction (LV and RV pressures, LVP and RVP; end-bending moment, *M*; shear force, *V*; axial force, *F*; tension due to RV free wall, T_{RV}).

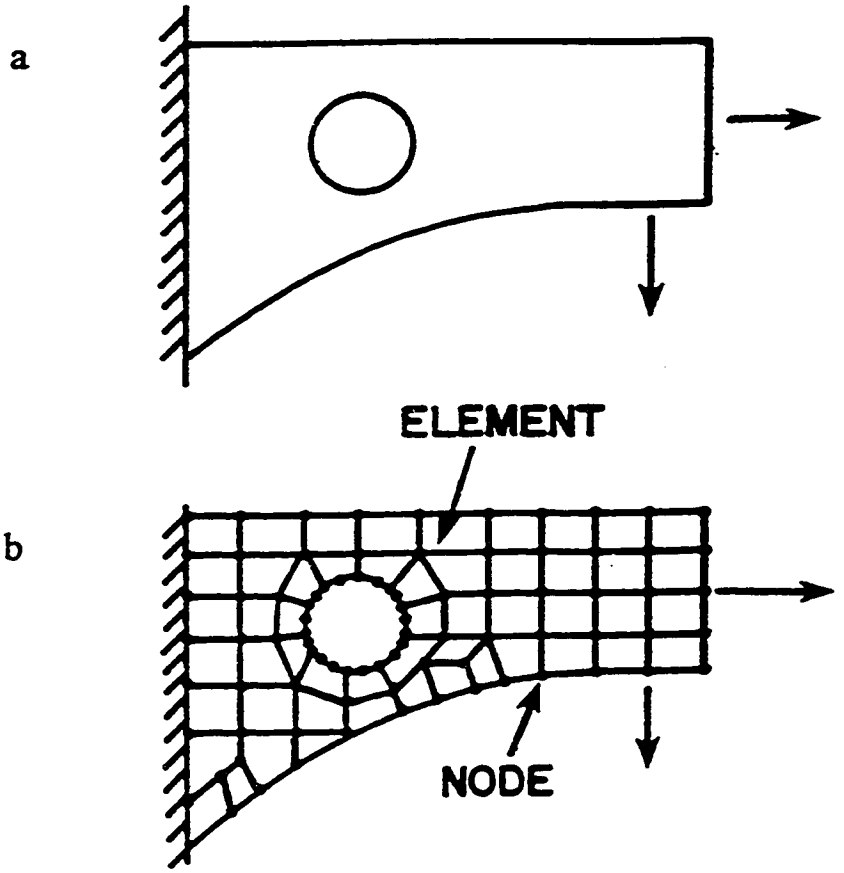

Figure 4.2 A loaded structure (a) and a typical finite element model (b).[25]

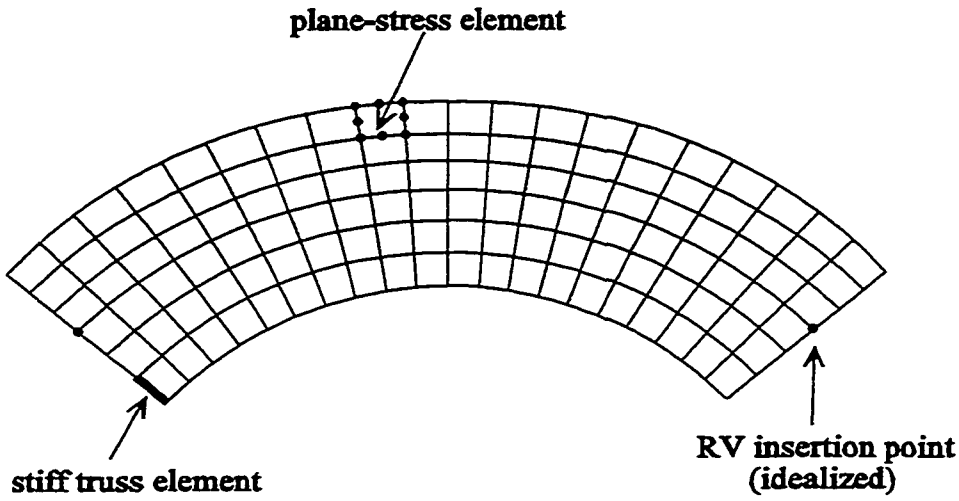

Figure 4.3 2-D finite element mesh used to model the interventricular septum. The mesh consisted of 120 8-node plane-stress elements arranged in 6 layers of 20 elements. In addition, 6 stiff truss elements were used at each boundary (for simplicity, only one is shown) to allow for application of end-bending moments.

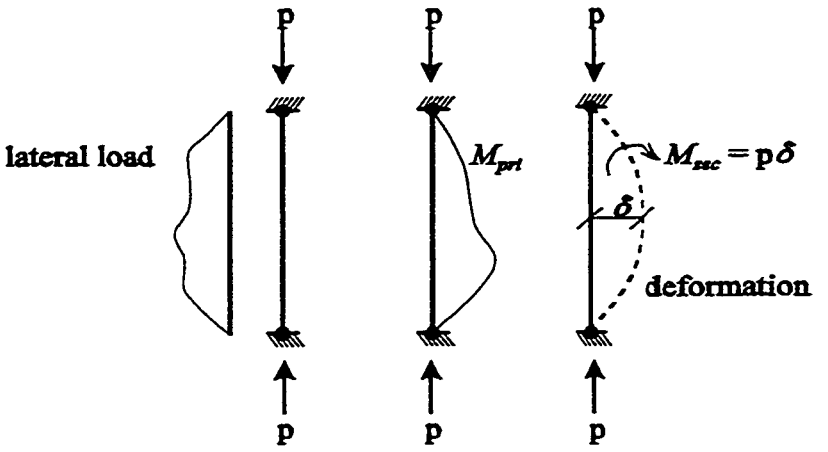

$$M_{tot} = M_{pri} + M_{sec}$$

- M_{pri} due to lateral loading
- M_{sec} additional moment due to "pδ" effect

Figure 4.4 Diagram illustrating the "pδ" effect. The axially loaded (p) column is subject to lateral load which produces an internal (primary) bending moment distribution (M_{pri}). The column deforms (δ) laterally under this loading, causing a secondary moment (M_{sec} = pδ) to develop, which in turn increases the deformation, δ. The total bending moment at any point (M_{tot}) is the sum of the primary and secondary bending moments ($M_{pri} + M_{sec}$).

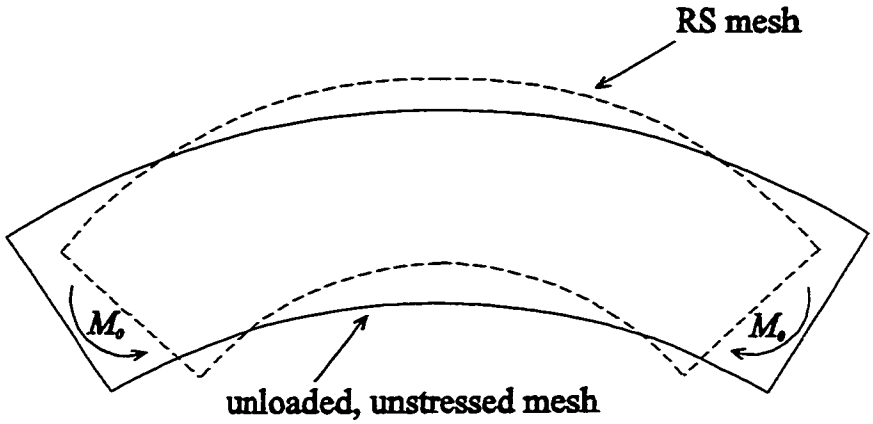

Figure 4.5 Diagram illustrating how the residually stressed mesh (RS mesh, dashed line) was obtained. Equal and opposite force couples (resulting in initial end-bending moments, M_0) were applied at the ends of the unloaded, unstressed mesh (solid line) such that the resulting stress distribution matched that calculated by Guccione et al.[52]

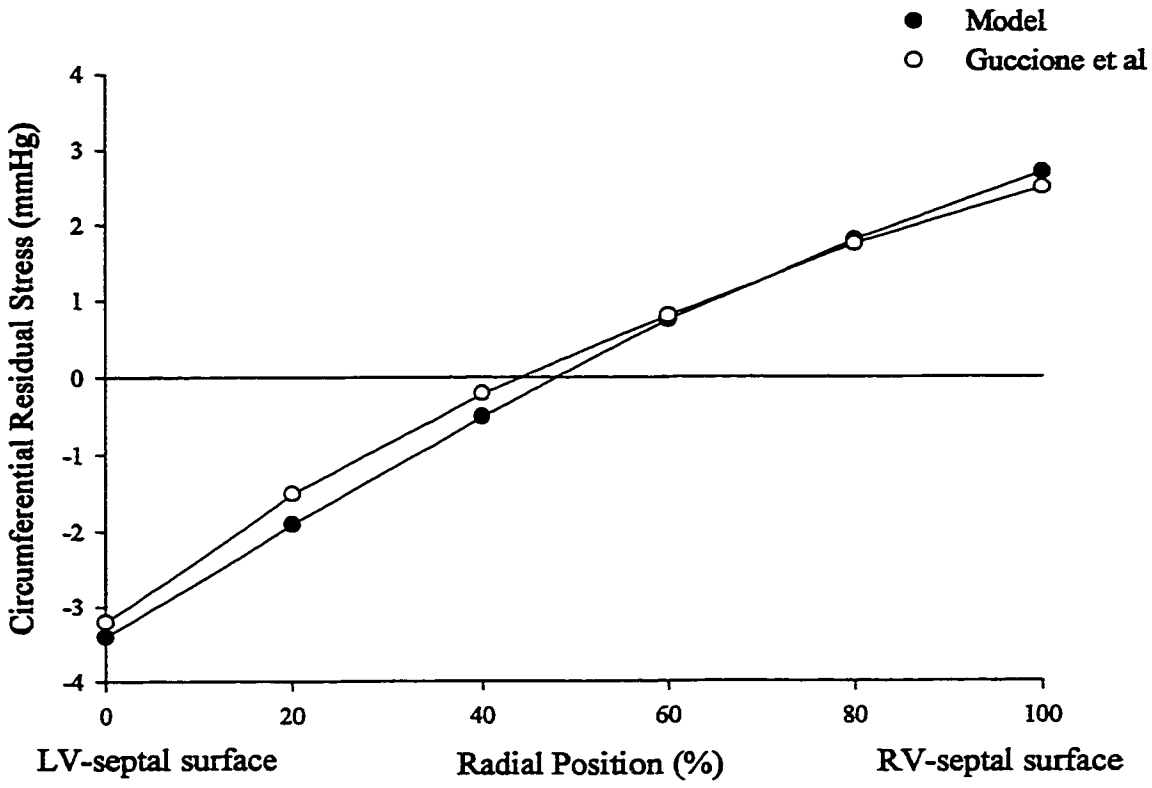

Figure 4.6 A plot of circumferential residual stress as a function of radial position. Note the similarity between the stress distribution in the RS mesh (filled circles) and that calculated by Guccione et al (open circles).[52]

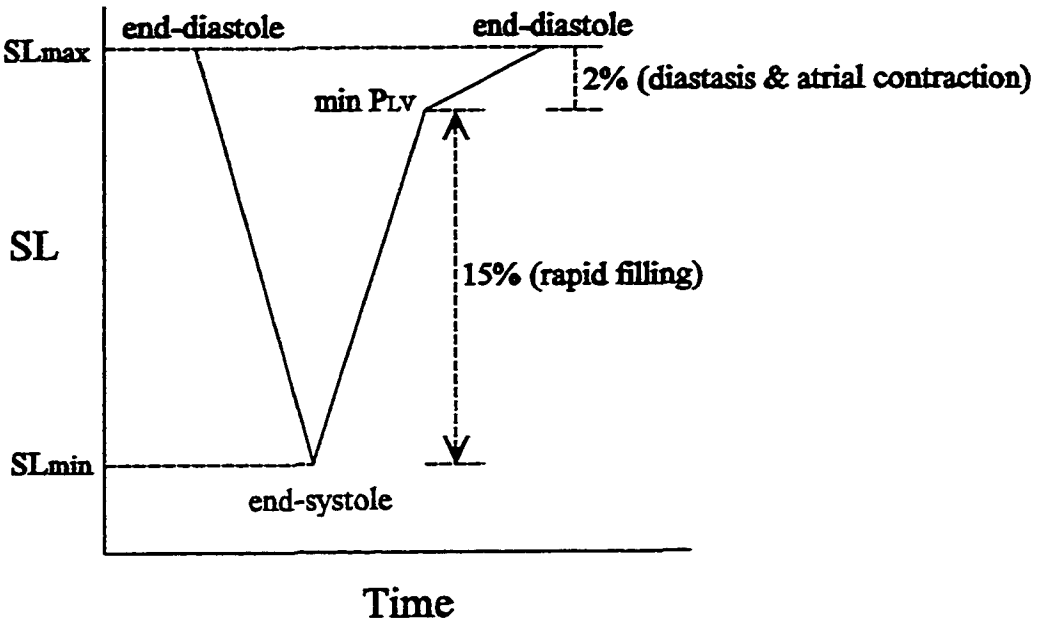

Figure 4.7 Sarcomere length (SL) changes schematized from the measurements of Rodriguez et al[125] and Guccione et al.[53] It was estimated that SL increased during diastole a total of 17% from end-systolic value (15% linearly to the point of minimum LV pressure [SL change due to rapid filling] and a further 2% linearly during diastasis and atrial contraction [SL change due to passive filling]).

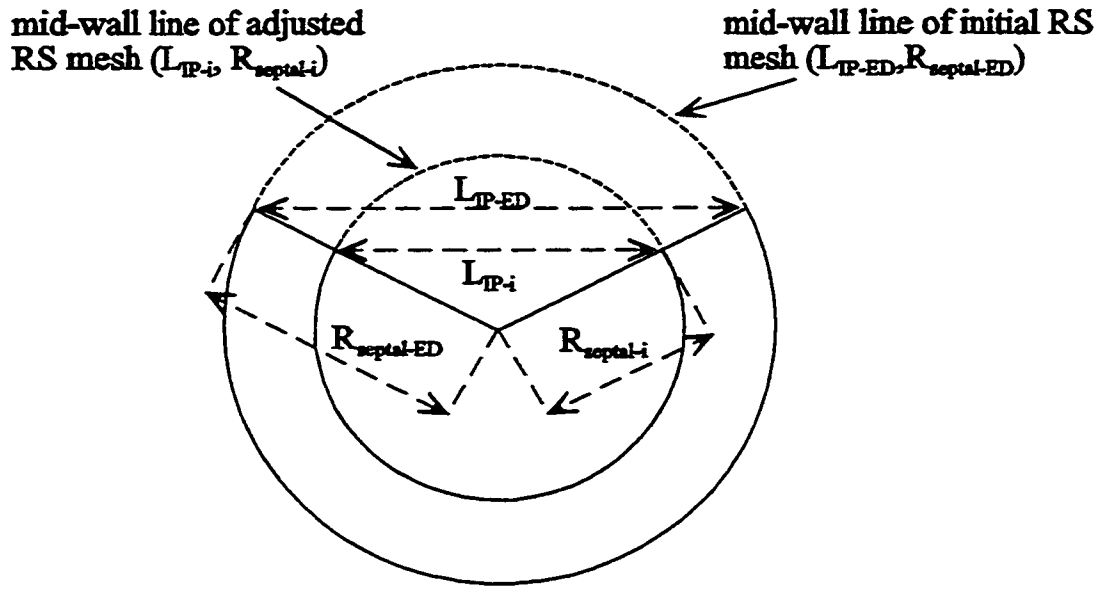

Figure 4.8 Diagram illustrating how the dimensions of the initial RS mesh were adjusted according to sarcomere length during the diastolic interval. Note how both the end-diastolic radius of curvature ($R_{septal-ED}$) and insertion-point length (L_{IP-ED}) are decreased when a decrease in sarcomere length is applied to the initial RS mesh ($R_{septal-i}$, L_{IP-i}). (N.B. Only mid-wall lines shown.)

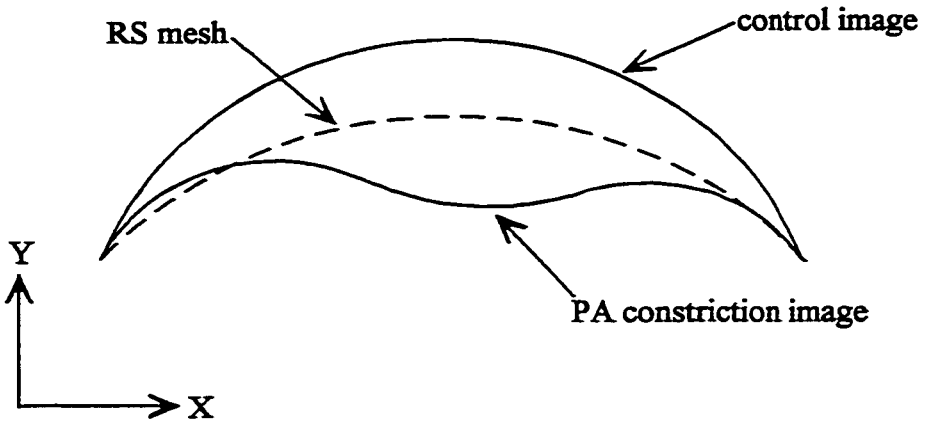

Figure 4.9 Diagram depicting how the RS mesh was loaded for both control and PA-constriction cycles (N.B. only mid-wall lines shown).. The RS mesh (dashed line) was restrained (in both X and Y directions) at the mid-nodes (i.e., at the RV insertion points) of each boundary; the measured LV and RV pressures were then applied. *G* and end-bending moments were adjusted until the loaded RS mesh conformed to the observed septal configuration (solid lines) satisfactorily.

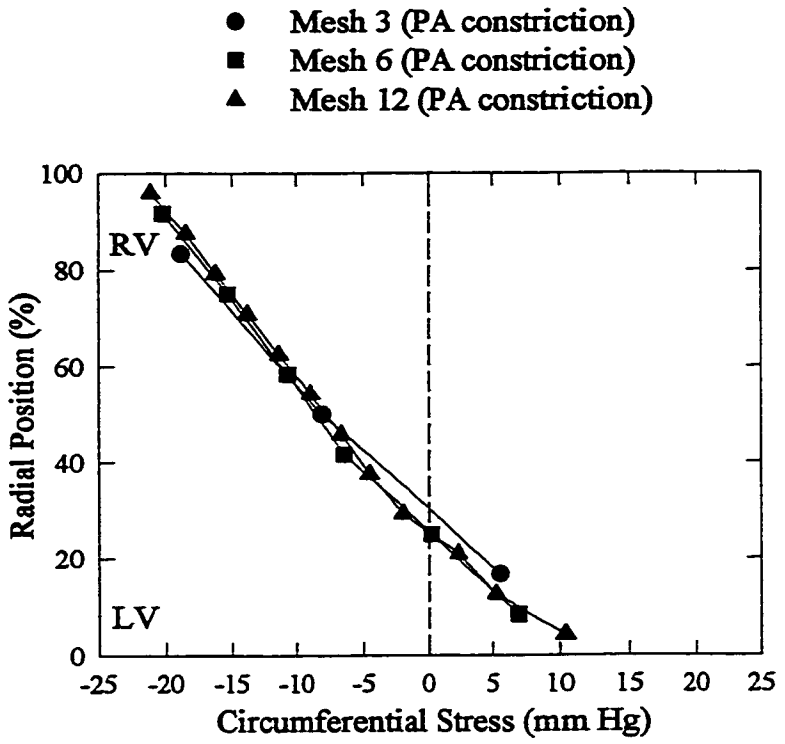

Figure 4.10 Comparison of transseptal (mid-septum) circumferential stress profiles obtained from three different meshes under the same loading (PA constriction). Each mesh was 20 elements long, but differed depending on the number of elements chosen to represent the thickness (3, 6, or 12).

CHAPTER 5

RESULTS

The 6 dogs, from which input data for this model were obtained, were chosen based on *expected* hemodynamics during the control loading conditions. Since temporal changes in many of these variables are well accepted and defined, only a brief description of these temporal trends will be provided. However, the effect of **PA constriction** on a specified variable will be emphasized.

5.1 Hemodynamics and Cardiac Function during Diastole

In Table 5.1, the effect of PA constriction on mean diastolic aortic pressure (AoP) is shown. Compared to control, mean diastolic AoP decreased during PA constriction in all 6 dogs. In Figure 5.1, left ventricular pressure (LVP) is plotted as a function of time for the entire diastolic interval. Each tick on the time axis corresponds to one echo frame. Note that control is denoted by open circles, PA constriction by filled circles. Unless otherwise stated, this code applies for all results presented in this manner. During both control and PA- constriction cycles (for all dogs), LVP decreased from end-systole (ES, see time axis) to a near stable value shortly after, which was maintained until end-diastole (ED, see time axis). Compared to control, LVP during PA constriction was reduced throughout diastole in Dogs 1-4. An opposite effect occurred (i.e., LVP increased during PA constriction) for a few points in Dogs 5 and 6, but in general, the same trend which was observed in Dogs 1-4, was seen in these 2 dogs. Figure 5.2 shows diastolic right ventricular pressure (RVP) for both control and PA-constriction cycles. In general, the same temporal trend in RVP was observed as in LVP (i.e., RVP decreased from ES to ED), and control

RVP values were roughly ⅓ to ½ that of control LVP values. In contrast to Figure 5.1, however, Figure 5.2 shows that, compared to control, RVP increased during PA constriction in all 6 dogs. The difference between the 2 pressures, the transseptal pressure gradient (TSP = LVP - RVP), is plotted in Figure 5.3. Compared to control, TSP for PA constriction was substantially lower (and negative) throughout diastole in all 6 dogs. In particular, TSP was reduced near 0 mm Hg at ES, dropped to a maximum negative value (Max TSP_{neg}; approximately -10 mm Hg in all 6 dogs) shortly after, and then became less negative for the duration of the cycle (in all dogs except Dog 5, TSP was the least negative mid-way through diastole, and then became progressively more negative toward ED).

Cross-sectional area of the LV (CSA_{LV}) was measured echocardiographically and used as an indicator of LV volume (see Figure 5.4). In both control and PA-constriction cycles, an isovolumic period (no or minimal change in CSA_{LV}) after ES was followed by an increase in CSA_{LV} towards a maximum value at ED. Compared to control, CSA_{LV} was substantially reduced during PA constriction in all 6 dogs. In an attempt to characterize the effect of PA constriction on diastolic LV function, LVP - CSA_{LV} curves were constructed and are shown in Figure 5.5. In all 6 dogs, the LVP - CSA_{LV} curve was shifted downward and to the left during PA constriction, as compared to control.

The effect of PA constriction on LV transmural pressure ($LVTMP = LVP - LVP_{peri}$) during diastole is shown in Figure 5.6. Compared to control, LVTMP was reduced during PA constriction in all 6 dogs. In contrast, RV transmural pressure ($RVTMP = RVP - RVP_{peri}$) increased during PA constriction (see Figure 5.7).

5.2 Septal Geometry during Diastole

Curvature ($1/R_{septal}$) of the mid-portion of the septum is plotted against time in Figure 5.8. In all 6 dogs, the curvature of the septum in the control loading condition decreased from ES to ED. During PA constriction, the curvature of the septum was reduced (i.e., the septum was flattened) compared to control. Furthermore, although TSP was lowered to a similar degree during PA constriction in all dogs (see Figure 5.3), Dogs 1, 4 and 6 showed flattening and inversion, while Dogs 2, 3 and 5 only showed flattening. In the 3 dogs which inverted, inversion was first observed mid-way through diastole. In all dogs except Dog 5, flattening or inversion became less severe towards ED.

Insertion-point length (L_{IP}) of the septum is plotted against time for both control and PA constriction in Figure 5.9. In all 6 dogs, L_{IP} increased from ES to ED for both loading conditions. No apparent difference in L_{IP}, however, was observed between control and PA-constriction loading conditions.

In Figure 5.10, the thickness of the septum is plotted for both control and PA constriction cycles during diastole. Thickness decreased from ES to ED in both conditions. Compared to control, there was a trend towards increasing thickness during PA constriction in Dogs 1-5 with essentially no change between the two conditions in Dog 6.

5.3 Structural Mechanics of the Septum during Diastole

5.3.1 Shear Modulus (G) and End-Bending Moments

Having applied LVP (internal pressure loading) and RVP (external pressure loading)

and accounted for geometric changes, 2 other variables, namely the shear modulus (G) and the end-bending moments, were adjusted to make the RS mesh conform satisfactorily to the observed shape of the septum.

In Figure 5.11, the shear modulus (G) is plotted as a function of time for both control and PA-constriction cycles during diastole. G, in both loading conditions, decreased rapidly from ES to a near stable value for the remainder of diastole. During PA constriction, in all dogs except Dog 6, G reached a minimum value mid-way through diastole and then increased until ED. Furthermore, compared to control, a statistically significant ($P < 0.05$) increase in G was required to obtain matches in the post-isovolumic relaxation period (post-IVR period; including dashed line and beyond) during PA constriction in all dogs except Dog 4 (for Dog 4, a greater G was required for control in the post-IVR period). A greater G was also required during PA constriction in the IVR period for Dogs 1, 4, 5 and 6 – some variation of this trend was observed in Dogs 2 and 3. It should be noted that at ES (in Dogs 5 and 6 during PA constriction), and in the region including and subsequent to the post-IVR line (in Dogs 2-6 in control and Dog 6 in PA constriction), "dropout" occurred, at which point a match between the RS mesh and the observed shape of the septum could not be obtained.

End-bending moments are plotted as a function of time in Figure 5.12. Only the end-bending moments required to obtain matches for PA constriction are presented, as no end-bending moments were required to produce the observed shapes in the control cycles. For all 6 dogs, greater end-bending moments were required near ES, as compared to those

required for the rest of diastole. Furthermore, in all 6 dogs, a statistically significant ($P < 0.05$) increase in end-bending moment was required at the anterior insertion point (open triangles; right side of the RS mesh) as compared to that at the posterior insertion point (open squares; left side of the RS mesh).

5.3.2 Principal Stress Vector Plots

To help illustrate the difference in structural behaviour between the septum during control and PA constriction, *principal stress* vector plots are presented. Figure 5.13a shows a plane stress element subject to x- and y-stress components σ_x, and σ_y, and the shear stress τ_{xy}. Rotation of the element through an angle (θ_p) such that τ_{xy} vanishes, results in the *principal stresses* σ_{min} and σ_{max} at point Q (see Figure 5.13b).

In Figures 5.14 through 5.19, principal stress vector plots are shown for a representative dog (Dog 1) during diastole. To minimize end-effects, the 4 columns of elements on either side of each mesh are not shown. All the arrows are equally scaled, the magnitude being represented by the size of the paired arrowheads and the distance between them. Whether the stress is tensile or compressive is represented by the direction of the arrowheads, divergent meaning tensile, convergent meaning compressive. Tension and compression generally also correspond to red and blue, respectively. Three locations in time (Max TSP_{neg}, mid-diastasis, and ED) were chosen to illustrate the difference in structural behaviour of the septum between control and PA constriction. Each vector plot pair (control and PA constriction) is accompanied (on the subsequent page) by transseptal

circumferential stress and corresponding strain plots in order to demonstrate approximate magnitudes. The values shown were averaged from the two middle columns of elements and were calculated at the centroid for each element (from the middle 2 columns) across the wall.

In Figure 5.14, vector stress plots for both control and PA constriction at Max TSP_{neg} (for control, a position equivalent in time to Max TSP_{neg} during PA constriction was chosen, i.e., near completion of IVR period) are shown. For both control and PA constriction, the radial compressive stresses which developed at the LV and RV surfaces were equal to the applied LV and RV pressures (this was true for all dogs, in each loading condition, and at every point in diastole). The circumferential stresses which developed in the control state were all tensile in nature, increasing across the wall from LV to RV (circumferential stress variation of 1 to 15 mm Hg, with a strain value maintained at nearly 5%, see Figure 5.15). Compared to control, during PA constriction, substantial circumferential compressive stresses clearly developed (circumferential stress variation across the septum from 3 to nearly -50 mm Hg, with corresponding strains of 2 to -5%, respectively, see Figure 5.15). Furthermore, these compressive stresses became less regular (i.e., less circumferentially oriented) in elements which were increasingly distant from the mid-portion of the RV-septal surface. In these elements, the compressive stresses appeared to be directed towards the supports of the mesh at the mid-nodes of each end-boundary (not shown).

In Figure 5.16, vector stress plots for both control and PA constriction at mid-

diastasis are shown. In the control case, the circumferential stresses which developed were roughly equivalent to the residual stress distribution (circumferential stress variation of -3 to 5 mm Hg, with a strain value maintained at approximately 3%, see Figure 5.17). In the PA- constriction case, circumferential compressive stresses developed (circumferential stress variation across the septum from 9 to -20 mm Hg, with corresponding strains of 10 to -18%, respectively, see Figure 5.17) which were directed towards the supports of the mesh as described above.

In Figure 5.18, vector stress plots for both control and PA constriction at ED are shown. In the control case, the circumferential stresses which developed were, again, roughly equivalent to the residual stress distribution (circumferential stress variation of -4 to 3 mm Hg, with a strain value maintained at approximately 3%, see Figure 5.19). In the PA constriction case, circumferential compressive stresses developed (circumferential stress variation across the septum from 5 to -28 mm Hg, with corresponding strains of 3 to -8%, respectively, see Figure 5.19) which were directed towards the supports of the mesh as described above.

5.3.3 Structural Bending Stiffness (K_{bend})

The structural bending stiffness, K_{bend}, was calculated as follows:

For a 2-D model with a breadth of unity, K_{bend} is:

$$K_{bend} = E\frac{t^3}{12}$$

where E is Young's Modulus, and t is thickness. E is related to the shear modulus, G, by:

$$E = 2G(1 + \upsilon),$$

where υ is Poisson's ratio. For incompressibility, assume $\upsilon \approx 0.5$, and hence:

$$E = 3G.$$

Substituting in the expression for E, K_{bend} in terms of G is:

$$K_{bend} = 3G\frac{t^3}{12}$$

In Figure 5.20, K_{bend} for both control and PA constriction cycles is plotted as a function of time for all 6 dogs. K_{bend}, in both loading conditions, decreased from ES to a near stable value for the remainder of diastole. Furthermore, compared to control, a statistically significant ($P < 0.05$) increase in K_{bend} was calculated in the post-IVR period during PA constriction in Dogs 1-3, and 5 (in Dog 4, a greater K_{bend} was calculated for the post-IVR period during control; in Dog 6, the increase in K_{bend} for the post-IVR period during PA constriction was not significant, NS). A greater K_{bend} was also calculated during PA constriction in the IVR period for all dogs except Dog 2 in which the control K_{bend} immediately after ES was greater than that for PA constriction.

5.3.4 Axial Force and Bending Moment Diagrams

Axial force and bending moment diagrams were constructed as follows: for element columns numbered 3, 5, 7, 10, 11, 14, 16, and 18, the circumferential stress variation (e.g., see Figure 5.21) was examined. Axial force was calculated at each location using the expression (assuming a breadth of unity):

$$Axial\ Force = \left(\frac{\sigma_{RV} + \sigma_{LV}}{2}\right) t$$

Bending moment was calculated at each location using the expression (assuming a breadth of unity):

$$Bending\ Moment = \left(\frac{\sigma_{RV} - \sigma_{LV}}{2}\right) \frac{t^2}{6}$$

Axial force and bending moment diagrams were then plotted as a function of element position (the average was taken for element columns 10 and 11) for a representative dog (Dog 1) in control (at mid-diastasis and ED), for an inverted septum (PA constriction, mid-diastasis), and for a flattened septum (PA constriction, ED).

In Figure 5.22, axial force for the control septum at mid-diastasis was slightly positive and remained constant through the mesh. Axial force for the control septum at ED was slightly negative and also remained constant through the mesh. Compared to control, the axial force diagrams for the two PA-constriction cases showed substantially negative

axial force which varied through the mesh, the more negative values being observed near the ends. In general, axial force for the flattened septum was more negative than that of the inverted septum.

In Figure 5.23, bending moment for the control septum at mid-diastasis and ED was slightly positive and remained constant through the mesh. Compared to control, the bending moment diagrams for the two PA-constriction cases were substantially different (the axial force diagrams for the two PA-constriction cases, however, were identical). Bending moment at the ends of each of the PA-constriction meshes was positive and of greater magnitude than the control. In both cases, the bending moment was zero near element positions 5 and 14. Maximum negative bending moment was achieved at the mid-length of the mesh in each case.

5.3.5 Strain Energy

Figure 5.24 shows strain energy calculated for the entire mesh (i.e., including the 4 columns of elements on either side of the mesh), SE_{full}, plotted as a function of time in all 6 dogs during both control and PA constriction. In general, greater SE_{full} was calculated for PA constriction during diastole for all dogs (some results opposite to this, however, were observed near ES). Furthermore, during control, maximum SE_{full} was achieved at ES in all 6 dogs, whereas during PA constriction, maximum SE_{full} seemed to reach a peak near Max TSP_{neg}.

SE_{full} and CSA_{LV} during control are plotted against time in Figure 5.25. In all 6

dogs, SE_{full} was reduced to a minimum level before CSA_{LV} began to increase. In contrast, Figure 5.26 shows that during PA constriction, in Dogs 2, 4, 5, and 6, the minimum level of SE_{full} was not achieved until CSA_{LV} began to increase. In Dogs 1 and 3, SE_{full} reached the minimum level as in the controls.

Table 5.2 shows the strain energy calculated for 60% of the mesh (i.e., not including the 4 columns of elements on either side of the mesh), SE_{60}, expressed as a percentage of SE_{full} during control and PA constriction at Max TSP_{neg} (for control, a position equivalent in time to Max TSP_{neg} during PA constriction was chosen) and ED in all 6 dogs. For control, at both the Max TSP_{neg} equivalent and ED, SE_{60} was approximately 60%. For PA constriction, SE_{60} at Max TSP_{neg} was approximately 15% and at ED approximately 20%.

5.4 Model Validation and Evaluation

5.4.1 Comparison of FE Solution with Thick-Walled Cylindrical Solution

A comparison of the stresses calculated with the FE model and stresses calculated with a known analytical model was performed (only control results were compared). For a section through a long hollow thick-walled cylinder subject to uniformly distributed internal and external pressure, the radial (σ_{rad}) and circumferential (σ_{circ}) stresses were calculated as follows:

$$\sigma_{rad} = \frac{P_i R_i^2 - P_o R_o^2}{R_o^2 - R_i^2} - \frac{\left(P_i - P_o\right) R_i^2 R_o^2}{R^2 \left(R_o^2 - R_i^2\right)}$$

and

$$\sigma_{circ} = \frac{P_i R_i^2 - P_o R_o^2}{R_o^2 - R_i^2} + \frac{(P_i - P_o) R_i^2 R_o^2}{R^2 (R_o^2 - R_i^2)}$$

where P_i is the internal pressure, P_o is the external (outer) pressure, R_i is the internal radius of curvature, R_o is the external (outer) radius of curvature, and R is the radius of curvature at a particular point across the thickness. The residual stress distribution across the wall was added in each case.

In Figure 5.27, radial stresses calculated (across the septum and at the centroid of each element) during control with the thick-walled solution and FE model are shown for a representative dog (Dog 1). At all 4 locations during the control cycle (ES, mid-IVR, mid-diastasis, and ED), good agreement was obtained between the 2 solutions.

In Figure 5.28, circumferential stresses calculated (across the septum and at the centroid of each element) at ES and mid-IVR during control with the thick-walled solution and FE model are shown for a representative dog (Dog 1). At both ES and mid-IVR, agreement between the 2 solutions was poor – the FE solution showed a circumferential tensile stress distribution which was greatest at the RV-septal surface, the opposite distribution (of approximately equal magnitude) was predicted by the thick-walled solution.

In Figures 5.29 and 5.30, circumferential stresses calculated (across the septum and at the centroid of each element) at mid-diastasis and ED during control, respectively, with the thick-walled solution and FE model are shown for all 6 dogs. Satisfactory agreement (i.e., the stress distributions had the same trend and magnitude) was obtained between the

2 solutions in all dogs at both locations.

5.4.2 Plane Stress vs. Plane Strain

In Figure 5.31, results at mid-diastasis for control and PA constriction (inverted septum) obtained from the current FE model (constructed using plane stress elements) and one constructed using plane strain elements are shown for a representative dog (Dog1). For both control and PA constriction, the circumferential stress and strain distributions predicted by the plane stress and plane strain models were nearly identical. Furthermore, the plane strain model predicted longitudinal compressive stress for both control (-4 to -2 mm Hg) and PA-constriction (1 to -17 mm Hg) loading conditions.

Table 5.1 Effect of PA constriction on mean diastolic aortic pressure (AoP).

		Mean Diastolic AoP (mm Hg)	
		Control	PA constriction
Dog	1	74.6	43.3
	2	94.5	66.9
	3	105.1	64.9
	4	88.0	58.4
	5	71.3	29.2
	6	103.2	64.7
Mean ± SD		89.5 ± 14.2	54.6 ± 15.1

SD, Standard Deviation

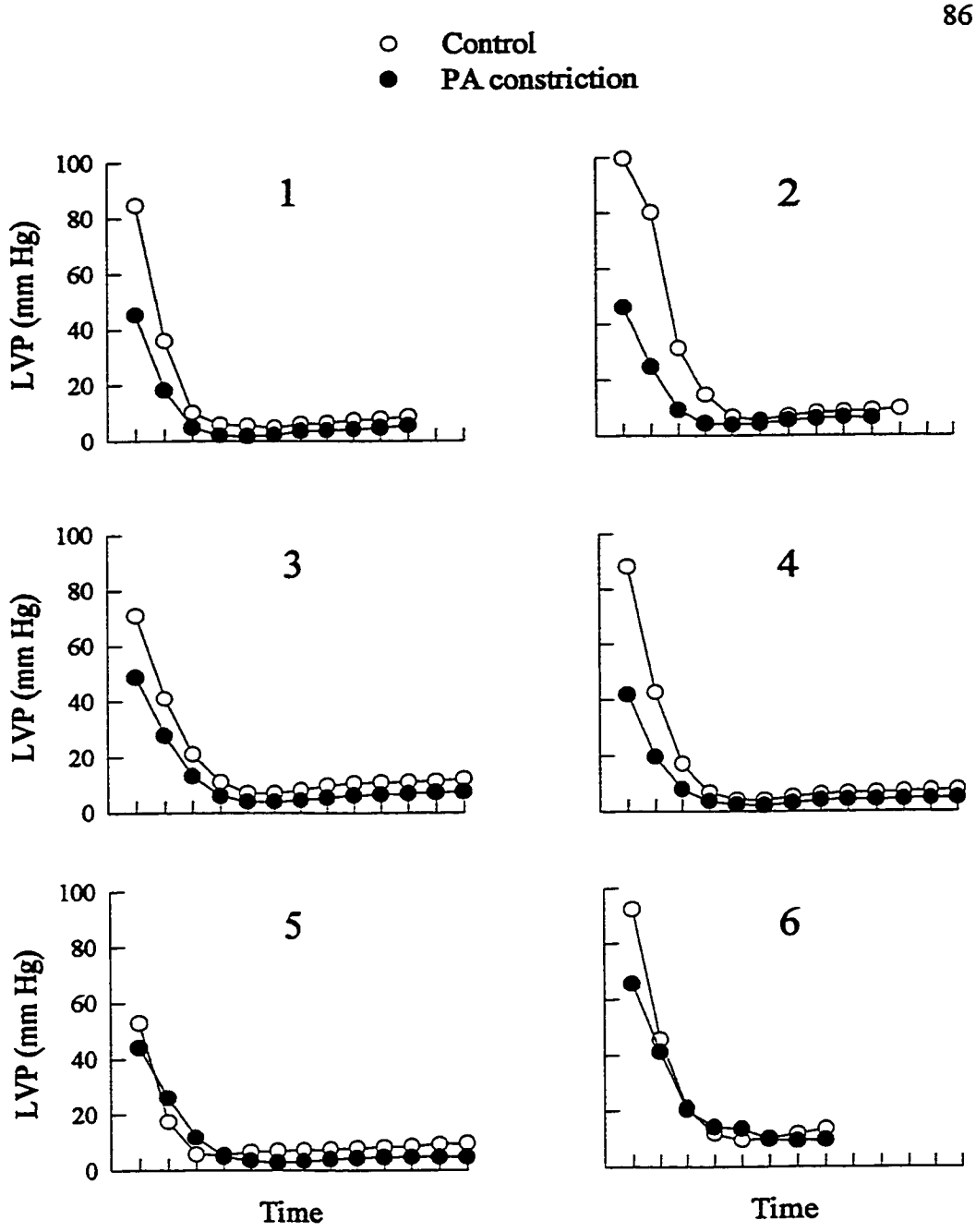

Figure 5.1 Left ventricular pressure (LVP) plotted as a function of time for control (open circles) and PA-constriction (filled circles) cycles during diastole (end-systole to end-diastole) in all 6 dogs. Each tick on the time axis corresponds to one echo frame.

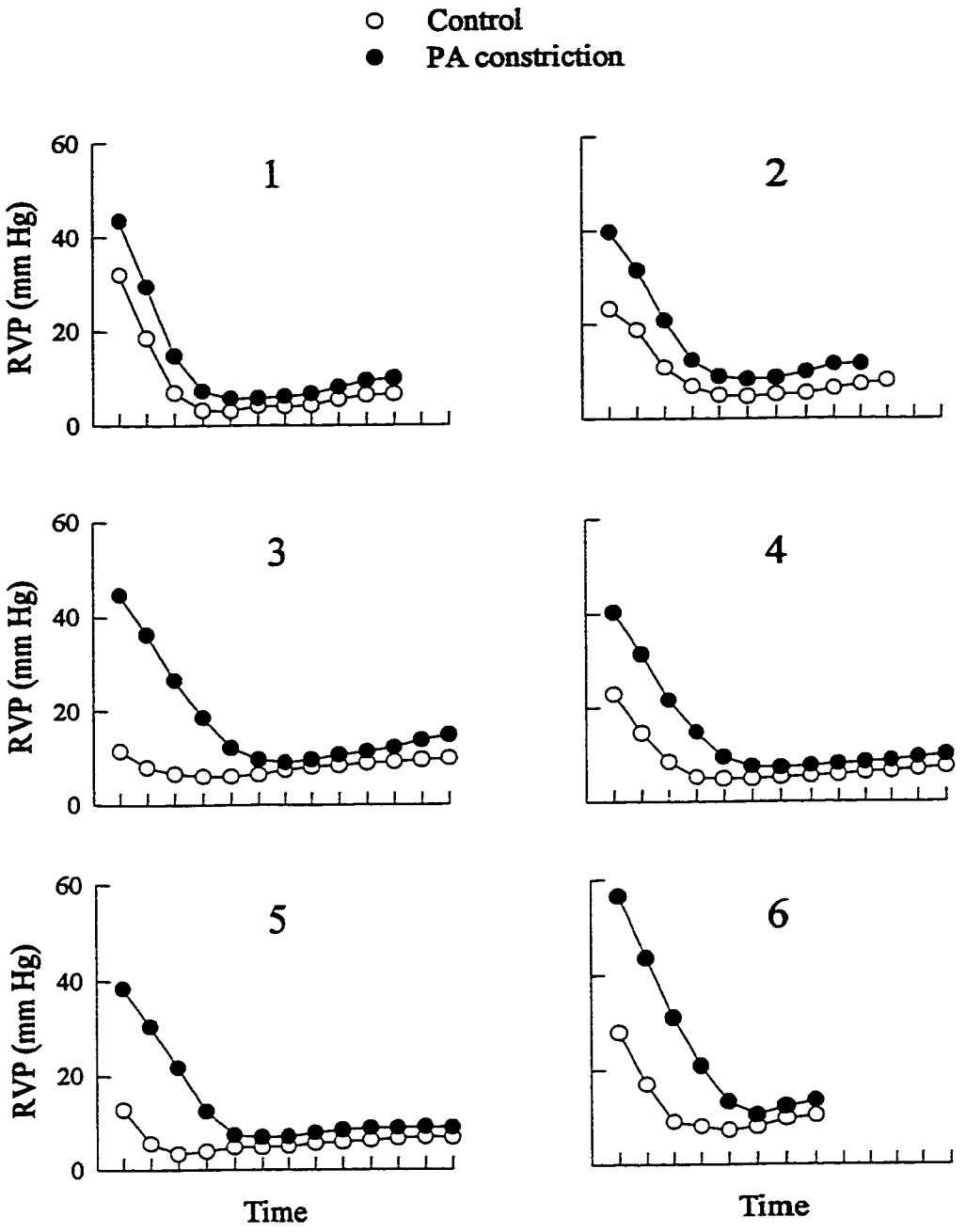

Figure 5.2 Right ventricular pressure (RVP) plotted as a function of time for control (open circles) and PA-constriction (filled circles) cycles during diastole (end-systole to end-diastole) in all 6 dogs. Each tick on the time axis corresponds to one echo frame.

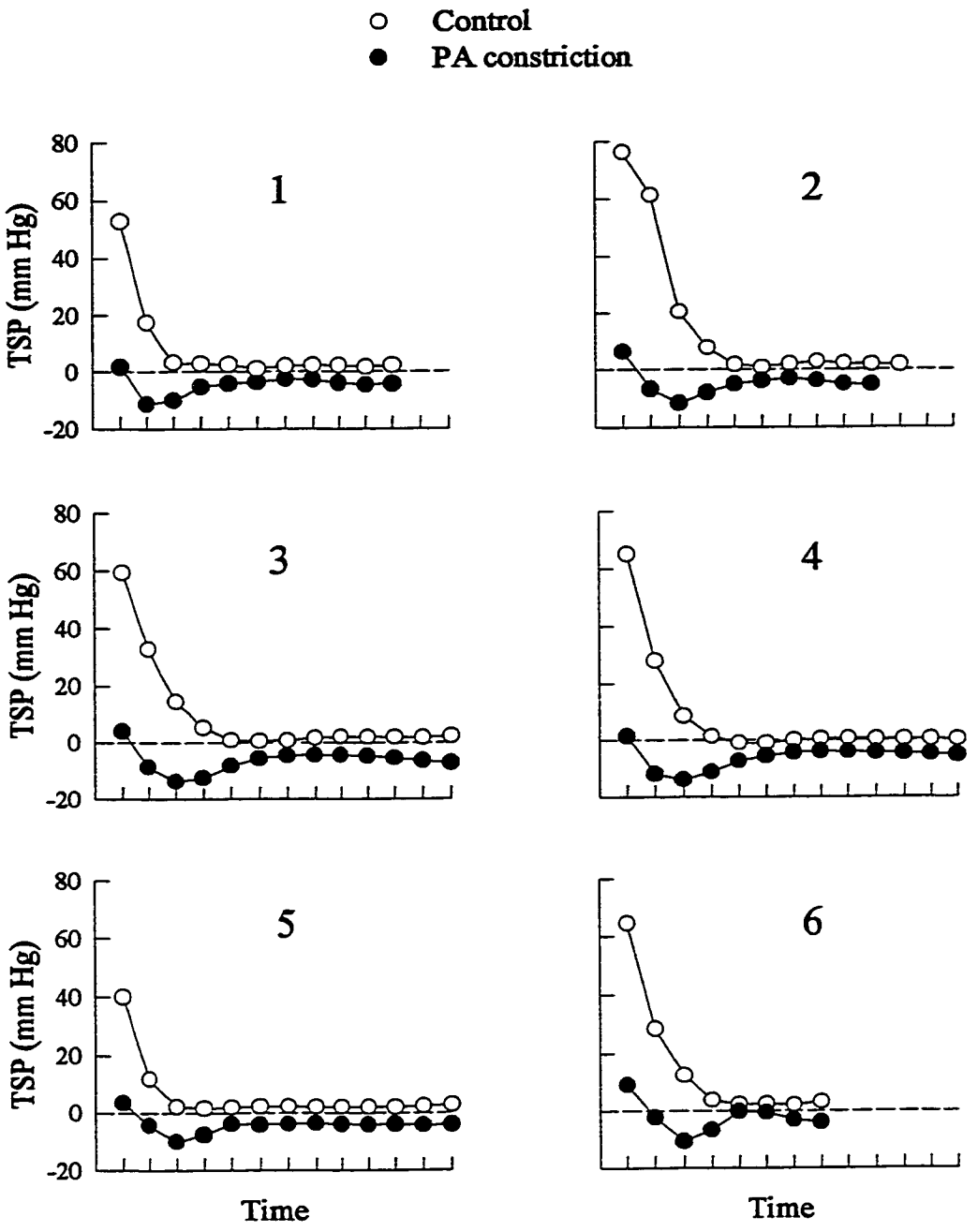

Figure 5.3 Transseptal pressure gradient (TSP = LVP - RVP) plotted as a function of time for control (open circles) and PA-constriction (filled circles) cycles during diastole (end-systole to end-diastole) in all 6 dogs. Each tick on the time axis corresponds to one echo frame.

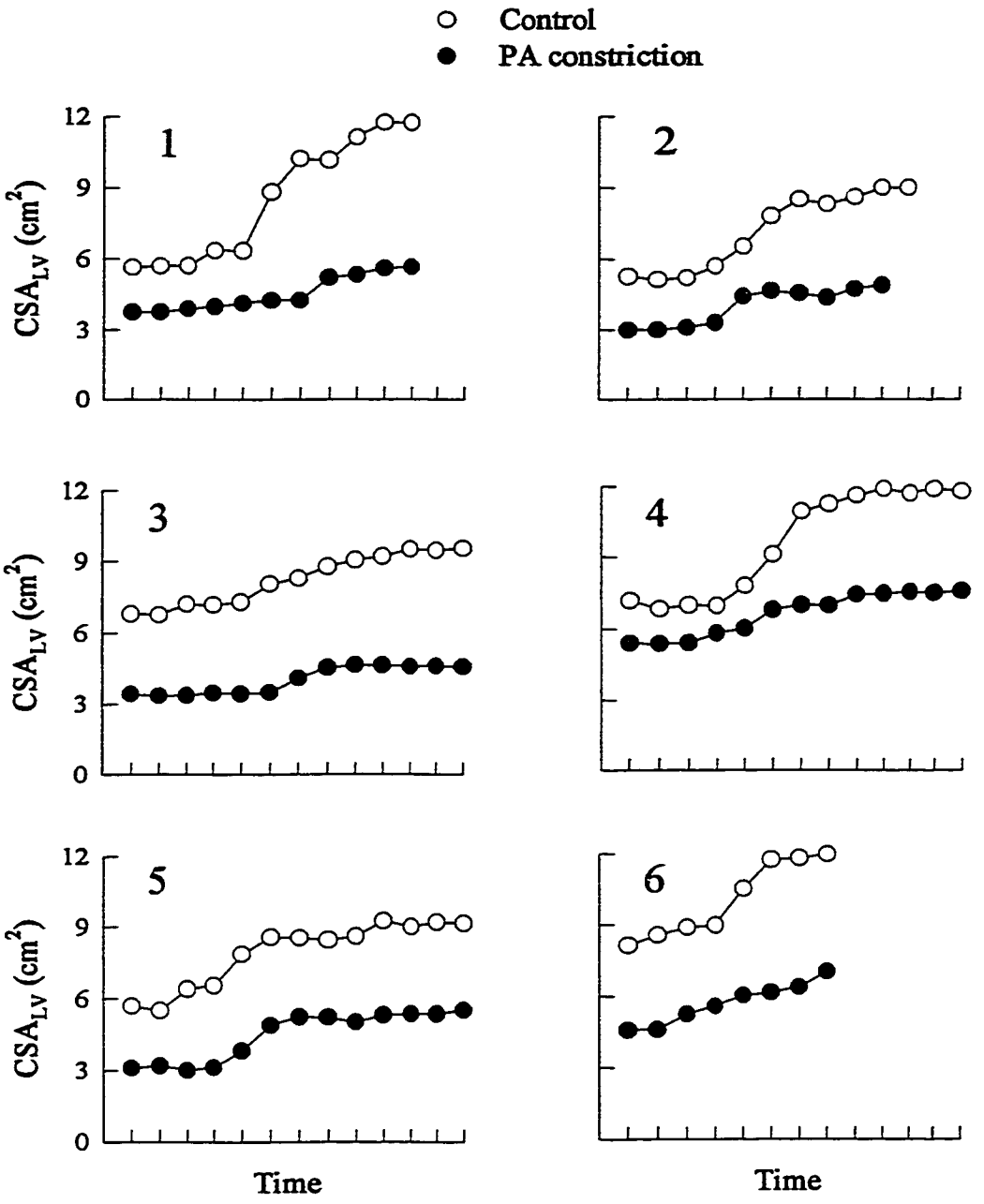

Figure 5.4 Left ventricular cross-sectional area (CSA_{LV}) plotted as a function of time for control (open circles) and PA-constriction (filled circles) cycles during diastole (end-systole to end-diastole) in all 6 dogs. Each tick on the time axis corresponds to one echo frame.

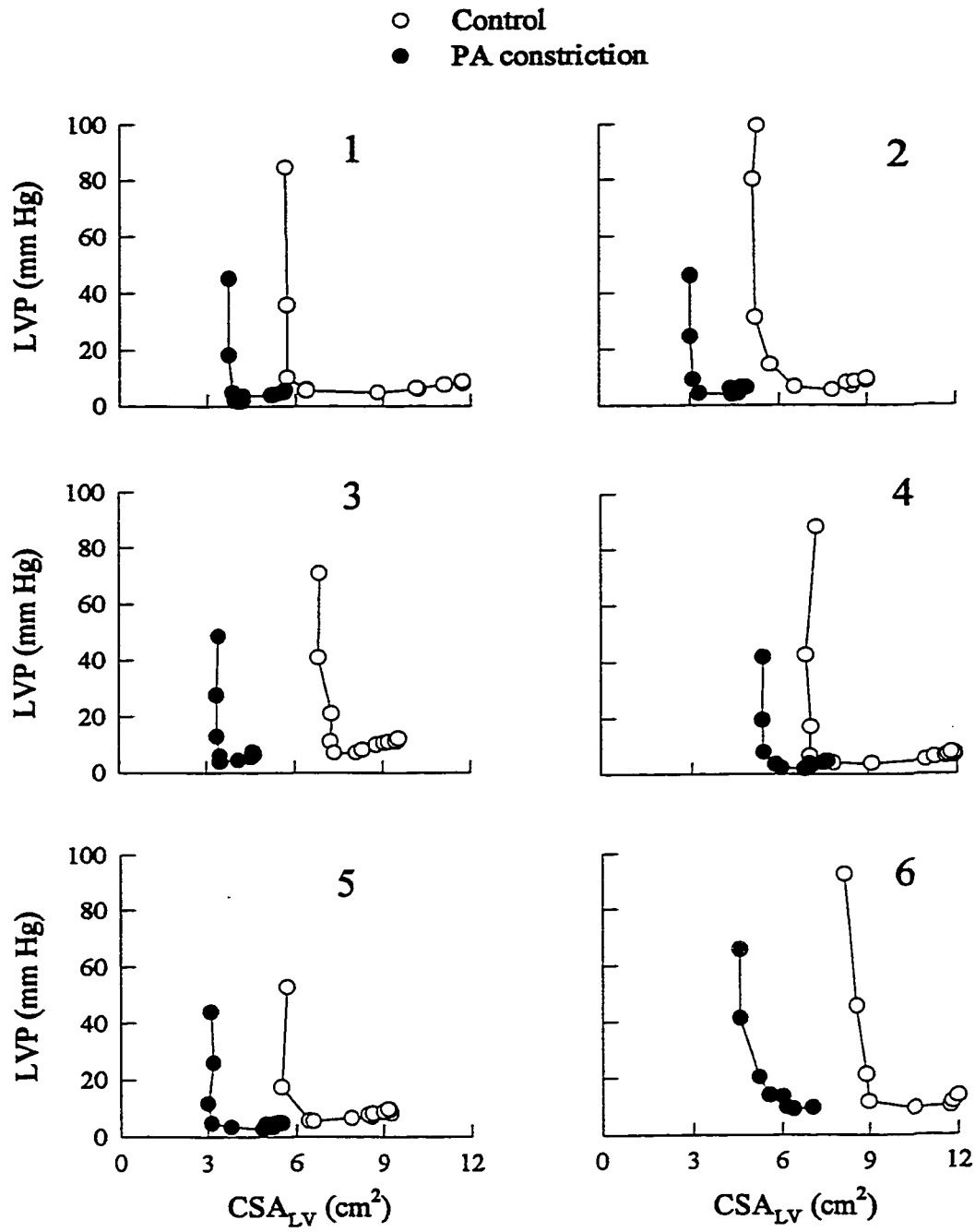

Figure 5.5 Left ventricular pressure (LVP) plotted as a function of left ventricular cross-sectional area (CSA_{LV}) for control (open circles) and PA-constriction (filled circles) cycles during diastole in all 6 dogs.

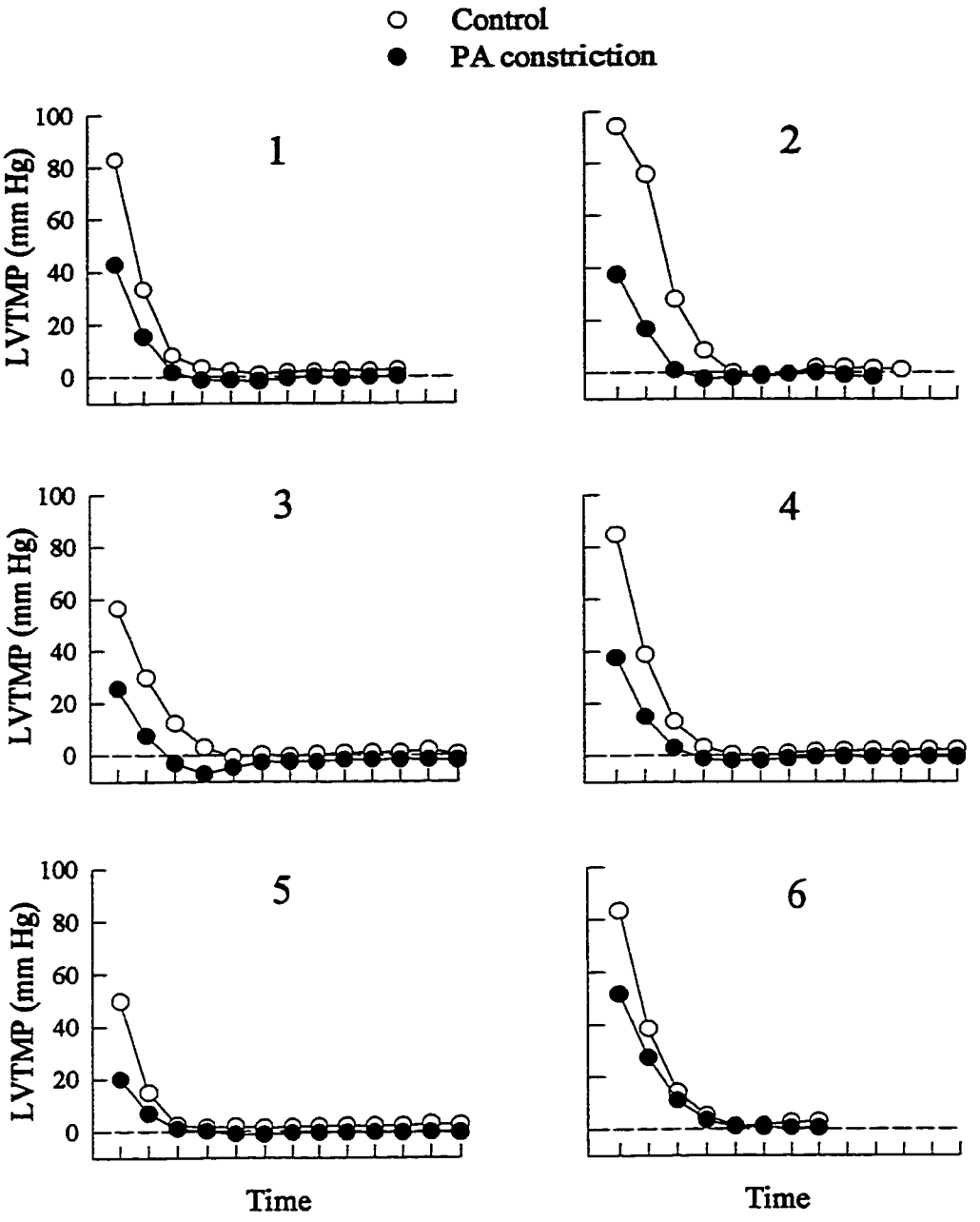

Figure 5.6 Left ventricular transmural pressure (LVTMP = LVP - LVP_{peri}) plotted as a function of time for control (open circles) and PA-constriction (filled circles) cycles during diastole (end-systole to end-diastole) in all 6 dogs. Each tick on the time axis corresponds to one echo frame.

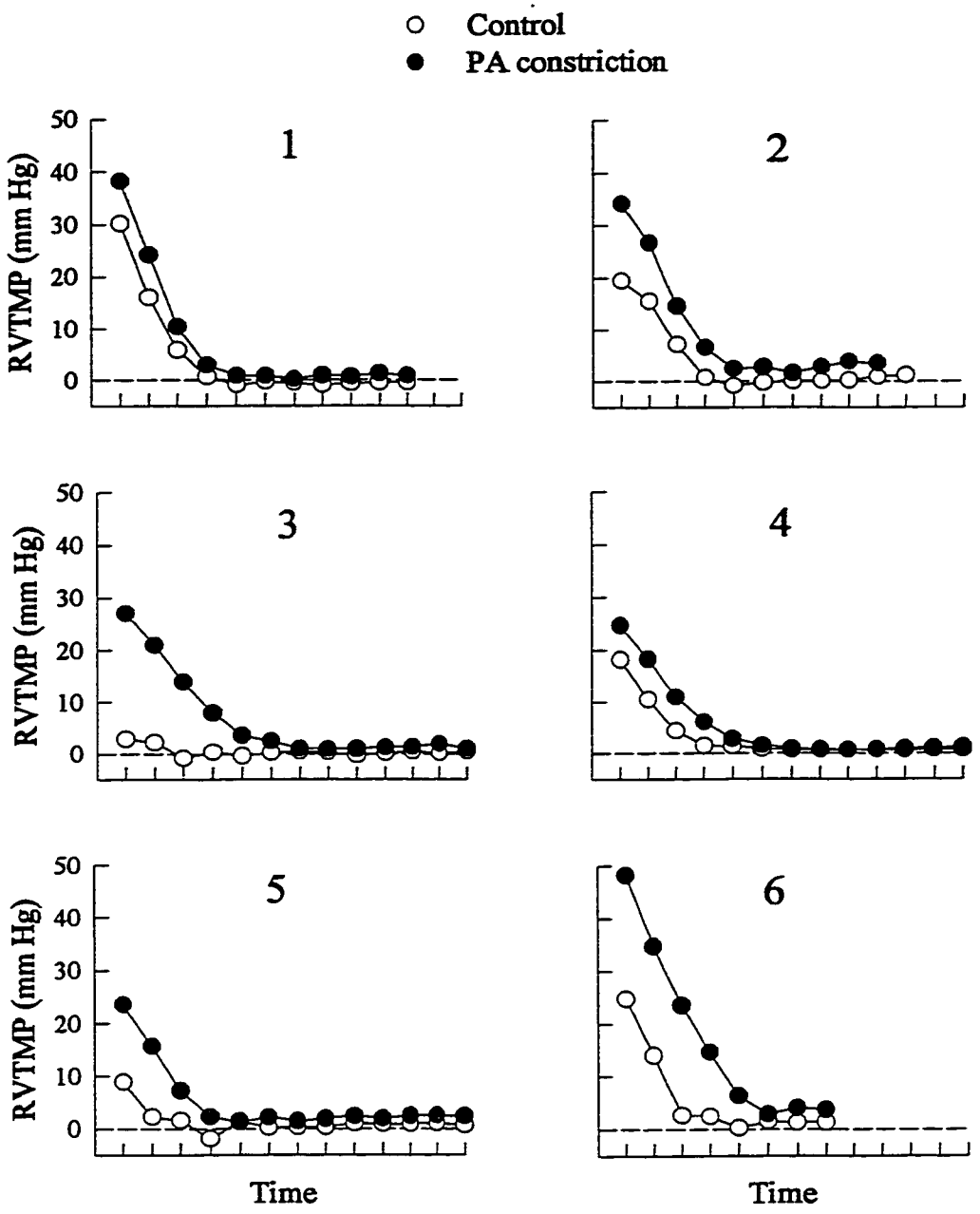

Figure 5.7 Right ventricular transmural pressure (RVTMP = RVP - RVP_{peri}) plotted as a function of time for control (open circles) and PA-constriction (filled circles) cycles during diastole (end-systole to end-diastole) in all 6 dogs. Each tick on the time axis corresponds to one echo frame.

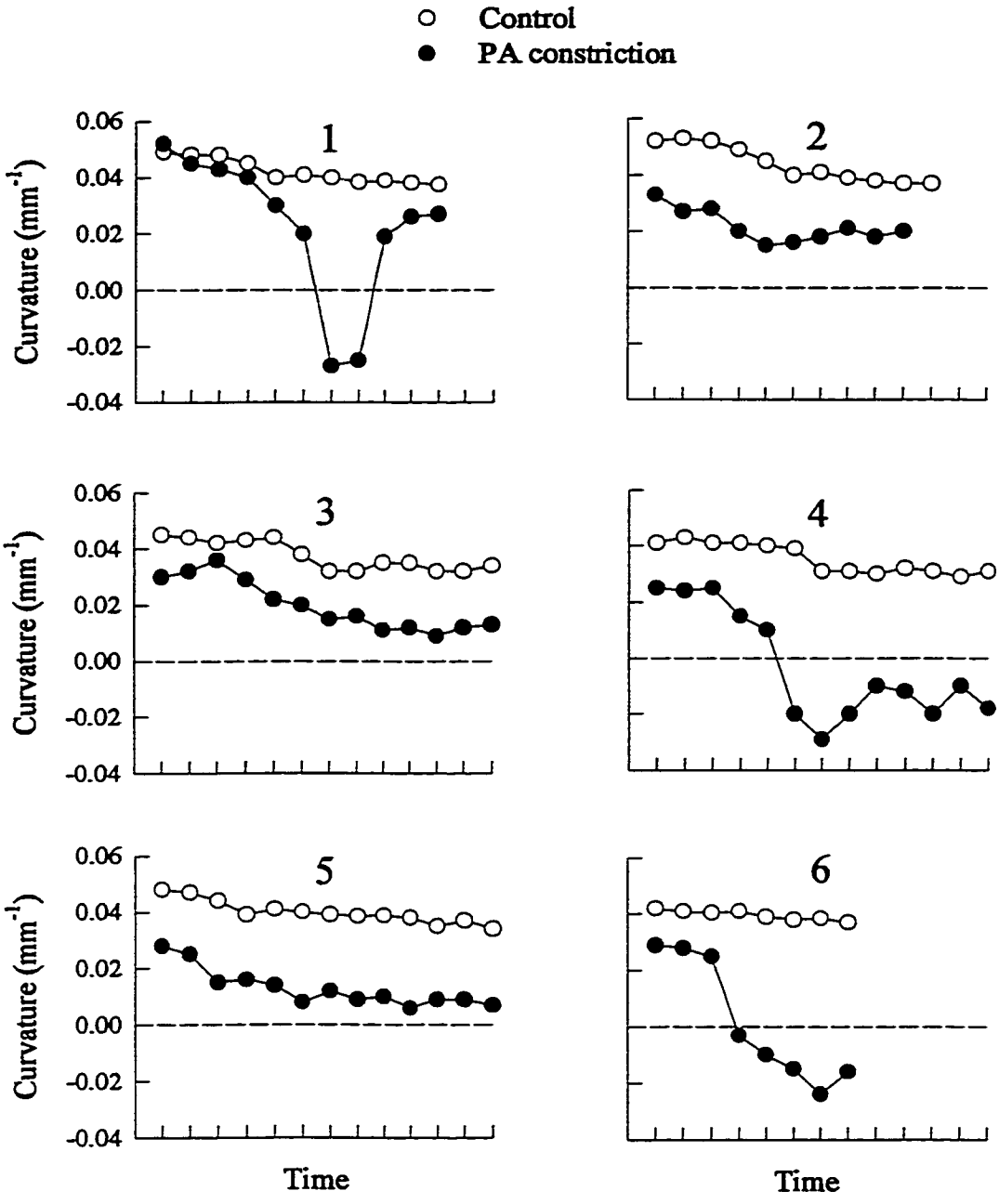

Figure 5.8 Curvature ($1/R_{septal}$) of the mid-portion of the septum plotted as a function of time for control (open circles) and PA-constriction (filled circles) cycles during diastole (end-systole to end-diastole) in all 6 dogs. Each tick on the time axis corresponds to one echo frame.

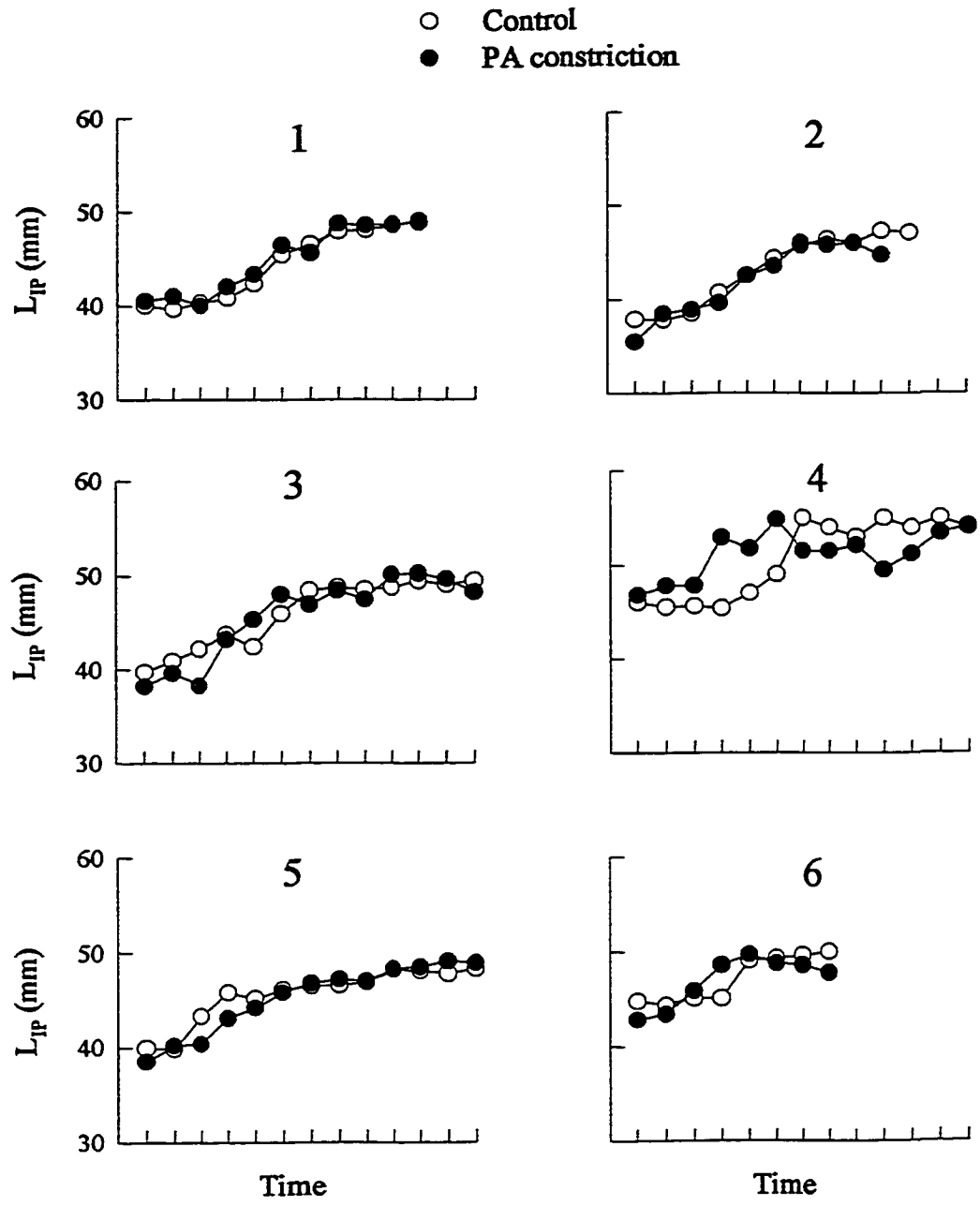

Figure 5.9 Insertion-point length (L_{IP}) of the septum plotted as a function of time for control (open circles) and PA-constriction (filled circles) cycles during diastole (end-systole to end-diastole) in all 6 dogs. Each tick on the time axis corresponds to one echo frame.

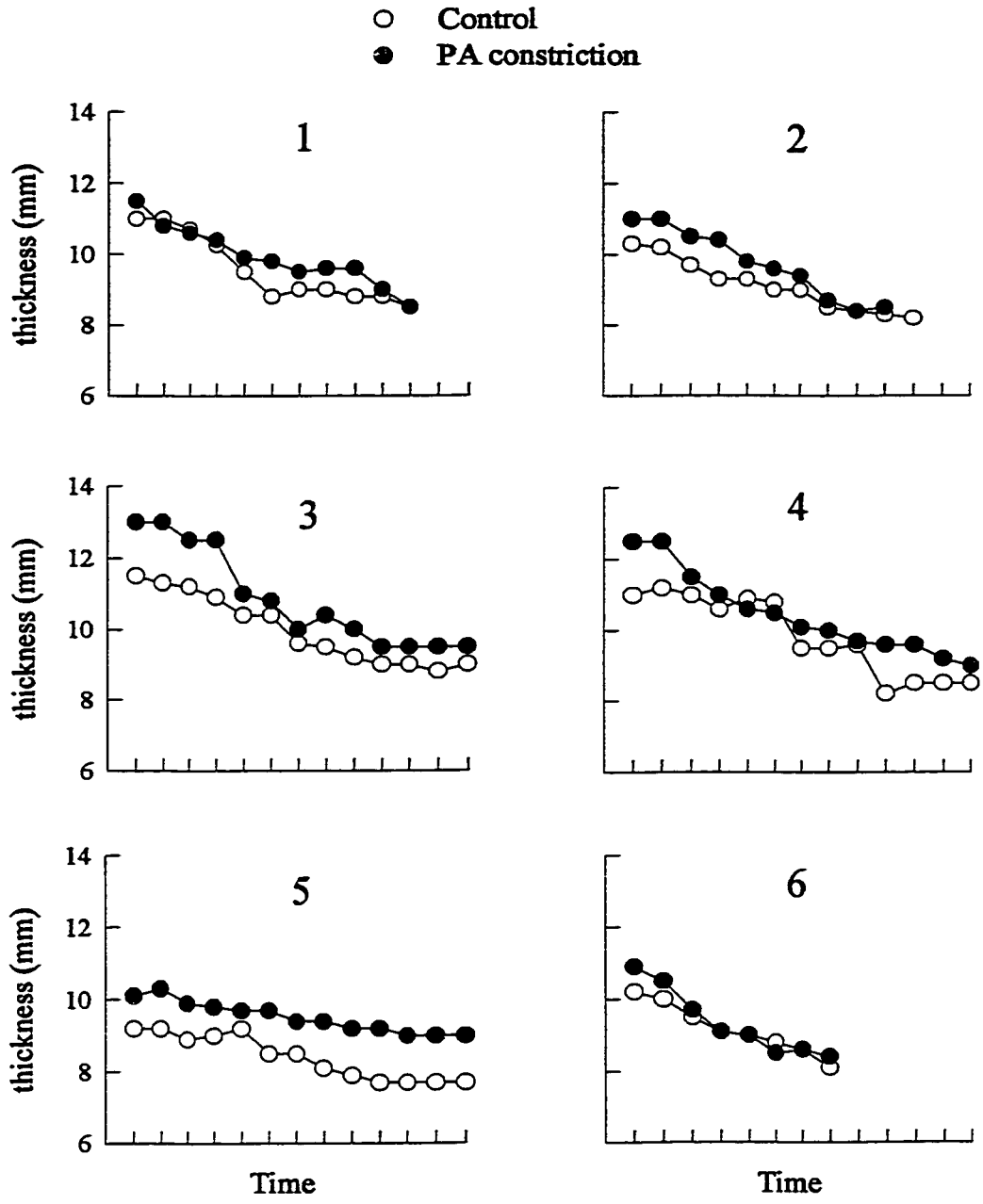

Figure 5.10 Thickness (t) of the septum plotted as a function of time for control (open circles) and PA-constriction (filled circles) cycles during diastole (end-systole to end-diastole) in all 6 dogs. Each tick on the time axis corresponds to one echo frame.

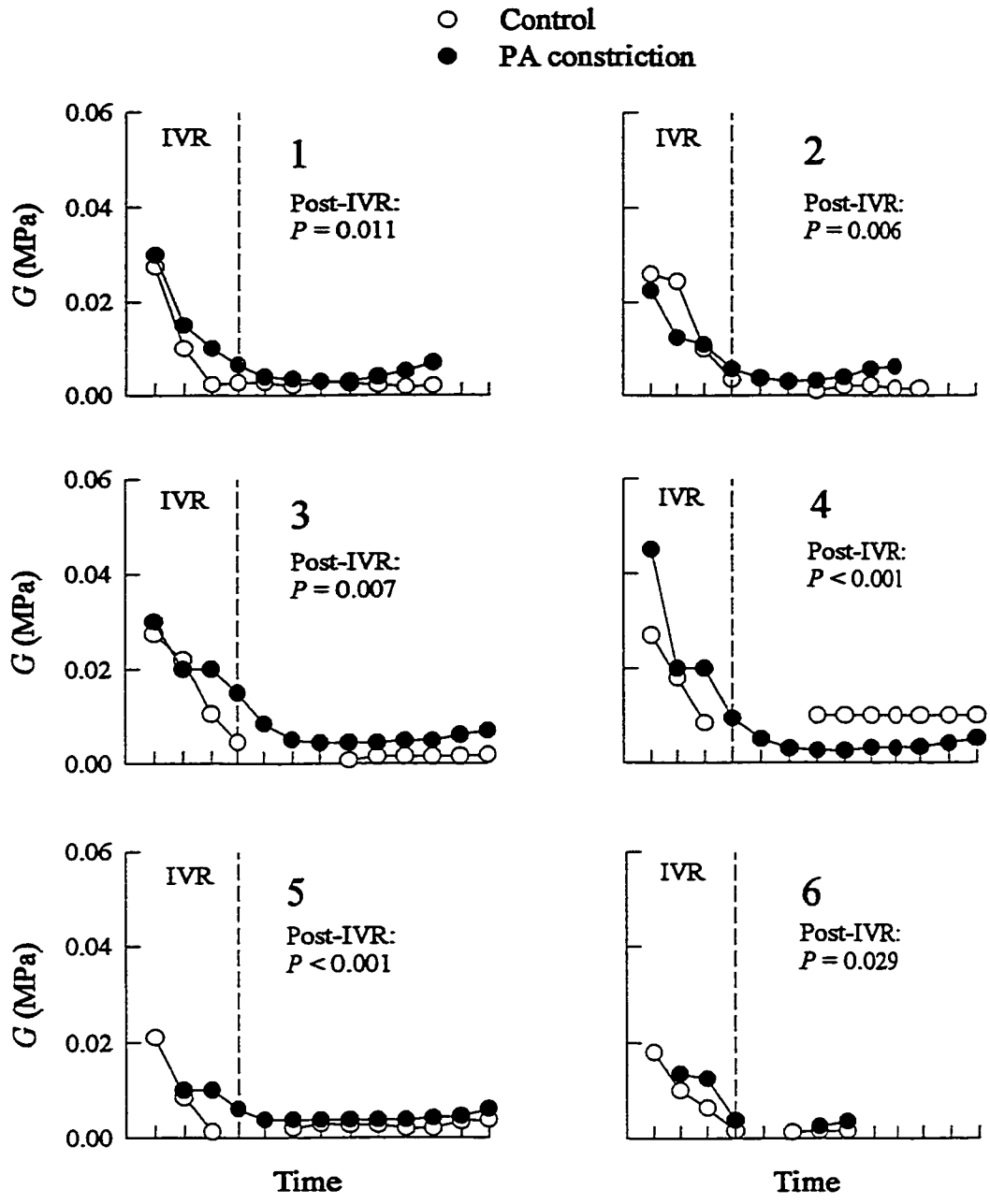

Figure 5.11 Shear modulus (G) of the septum plotted as a function of time for control (open circles) and PA-constriction (filled circles) cycles during diastole (end-systole to end-diastole) in all 6 dogs. Each tick on the time axis corresponds to one echo frame. (IVR: isovolumic relaxation period)

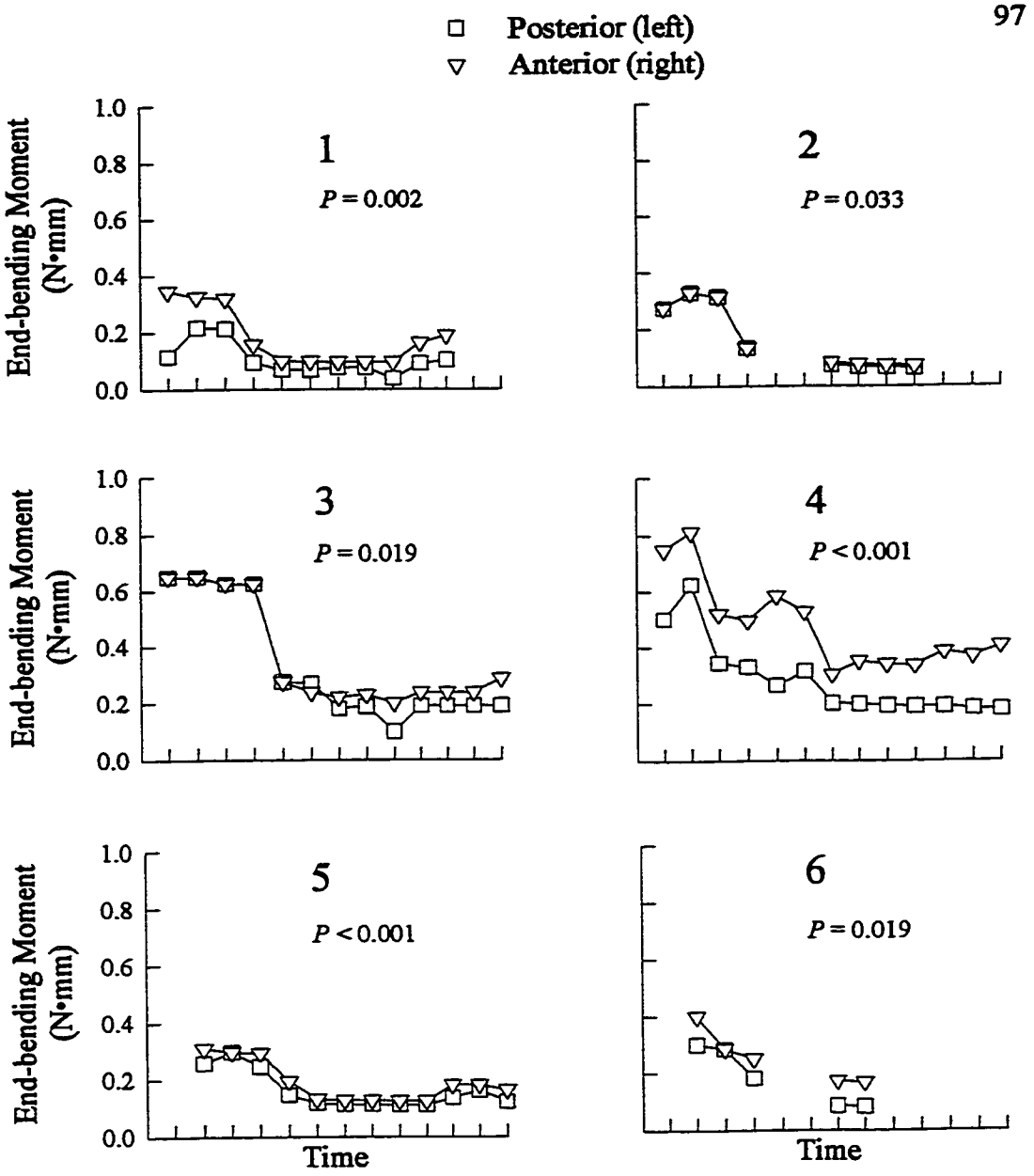

Figure 5.12 End-bending moments plotted as a function of time for the PA-constriction cycle during diastole (end-systole to end-diastole) in all 6 dogs. Each tick on the time axis corresponds to one echo frame. (Squares denote bending moments required at the posterior insertion point, or left side of the RS mesh; triangles denote bending moments required at the anterior insertion point, or right side of the RS mesh.)

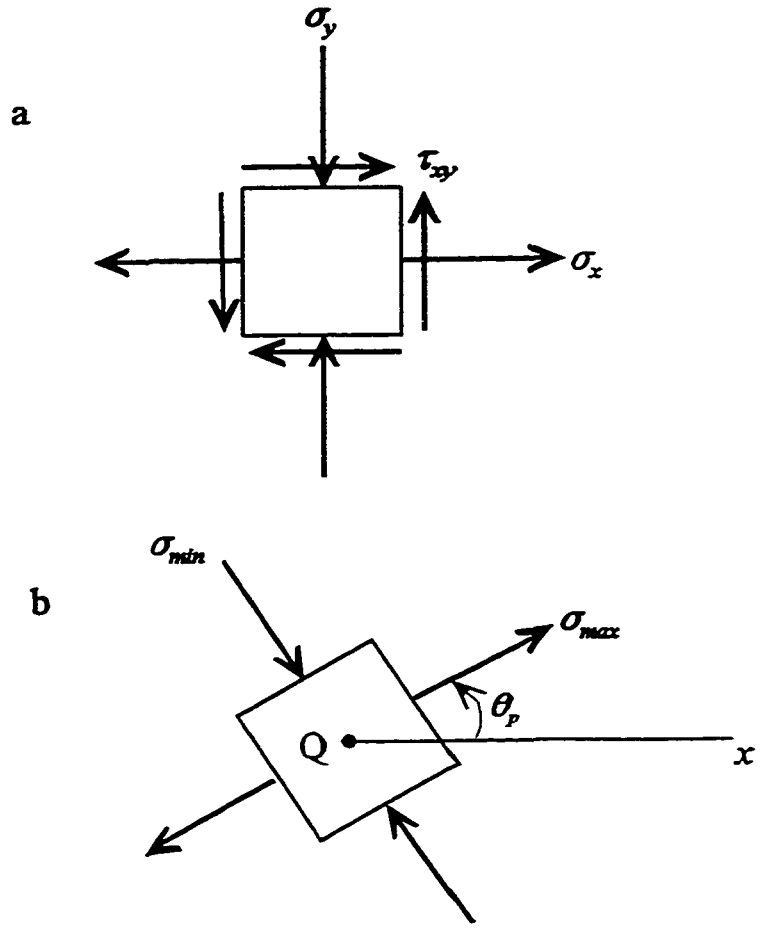

Figure 5.13 Schematic diagram relating (a) x-plane- , y-plane- , and shear-stress (σ_x, σ_y, and τ_{xy}, respectively) to (b) principle stresses (σ_{min} and σ_{max}).

Figure 5.14 Principal stress vector plots for control and PA-constriction loading conditions (representative dog, Dog 1) at the maximum negative transseptal pressure gradient, Max TSP_{neg} (for control, a position equivalent in time to Max TSP_{neg} during PA constriction was chosen, i.e., near completion of IVR period). To minimize end-effects, the 4 columns of elements on either side of each mesh are not shown. All the arrows are equally scaled, the magnitude being represented by the size of the paired arrowheads and the distance between them. Whether the stress is tensile or compressive is represented by the direction of the arrowheads, divergent meaning tensile, convergent meaning compressive. Tension and compression generally also correspond to red and blue, respectively.

Control
(Equivalent)

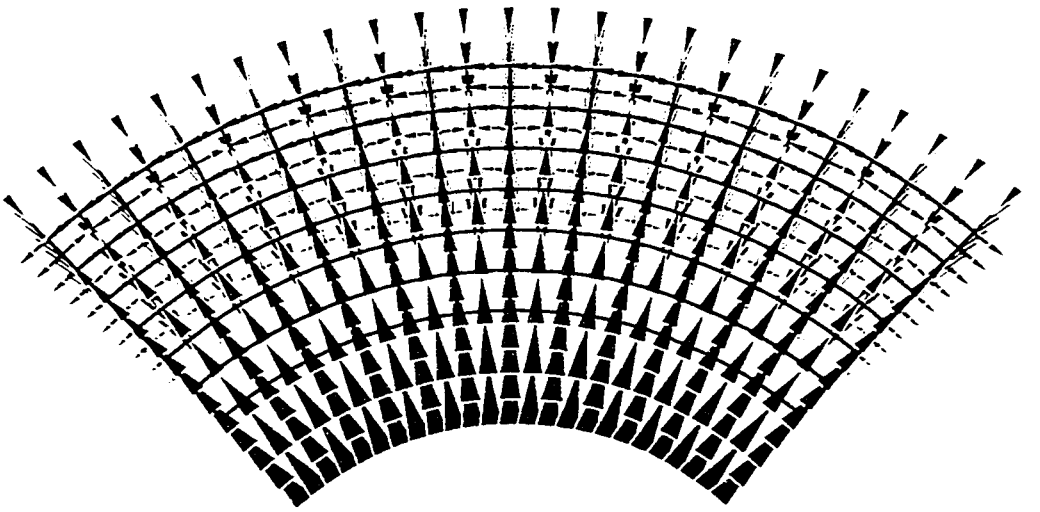

PA constriction
(Max TSP_{neg})

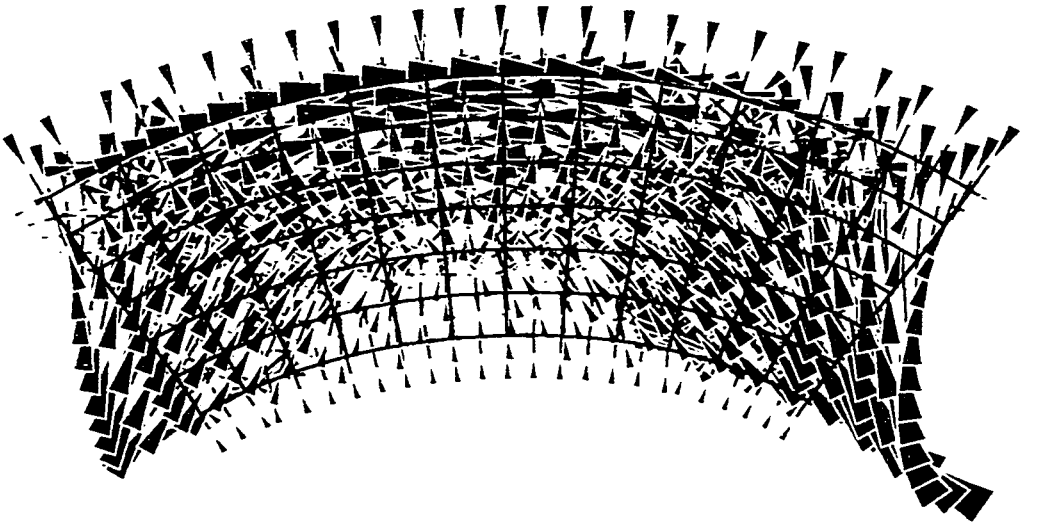

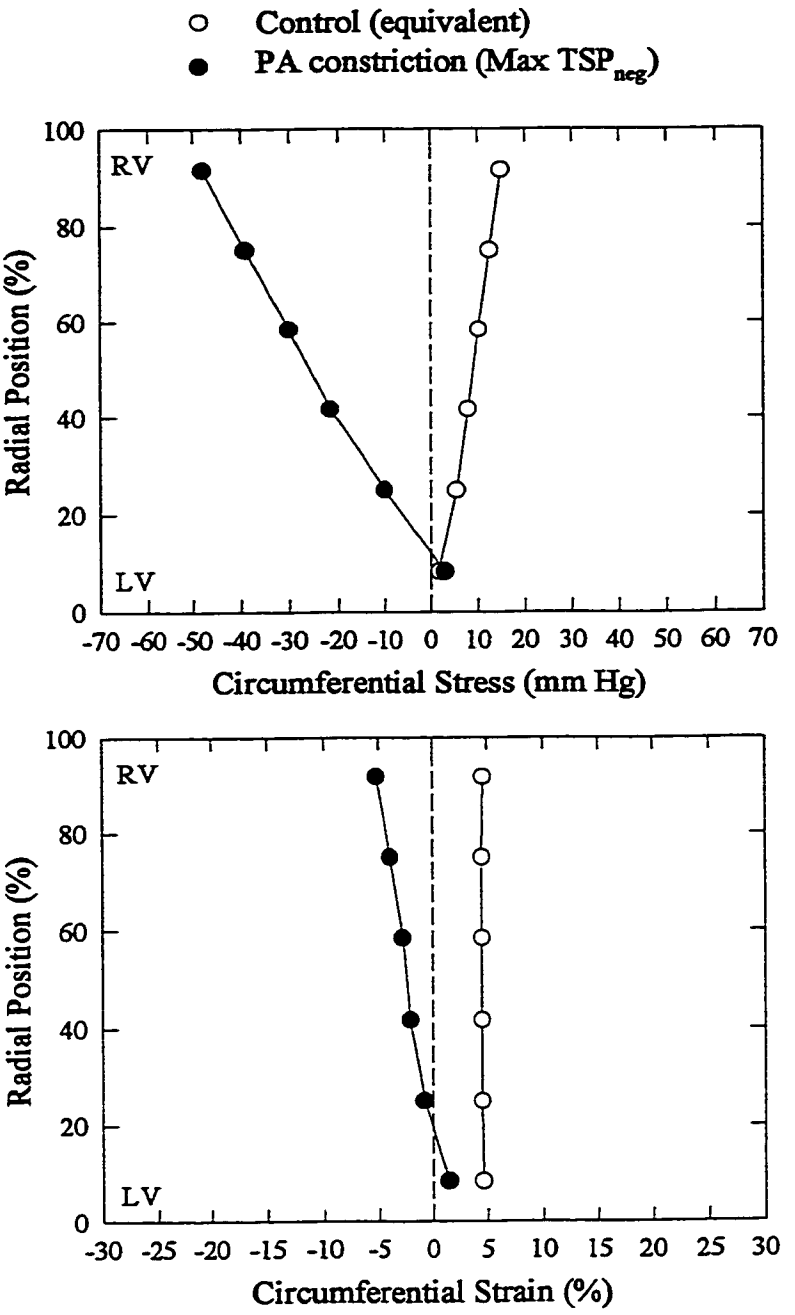

Figure 5.15 Plots of transseptal circumferential stress and strain for control and PA-constriction loading conditions (representative dog, Dog 1) at the maximum negative transseptal pressure gradient, Max TSP_{neg} (for control, a position equivalent in time to Max TSP_{neg} during PA constriction was chosen, i.e., near completion of IVR period).

Figure 5.16 Principal stress vector plots for control and PA-constriction loading conditions (representative dog, Dog 1) at mid-diastasis. To minimize end-effects, the 4 columns of elements on either side of each mesh are not shown. All the arrows are equally scaled, the magnitude being represented by the size of the paired arrowheads and the distance between them. Whether the stress is tensile or compressive is represented by the direction of the arrowheads, divergent meaning tensile, convergent meaning compressive. Tension and compression generally also correspond to red and blue, respectively.

Control
(Mid-diastasis)

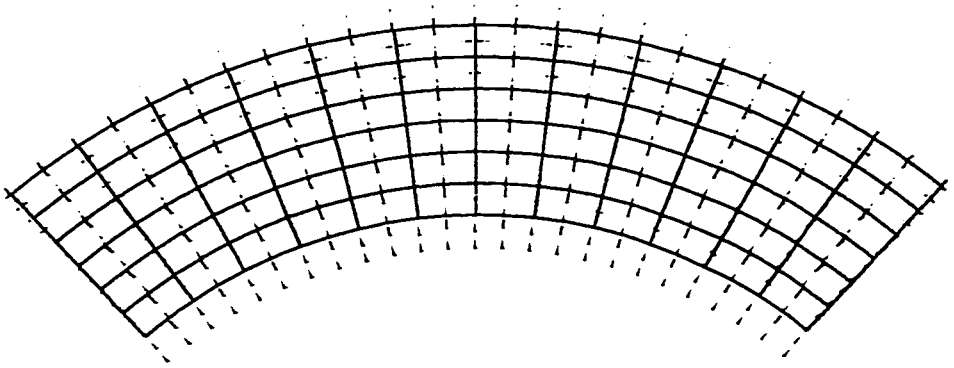

PA constriction
(Mid-diastasis)

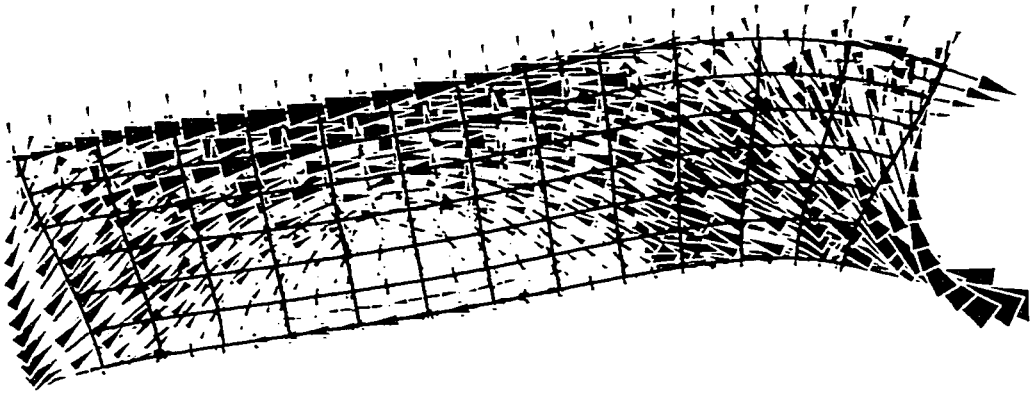

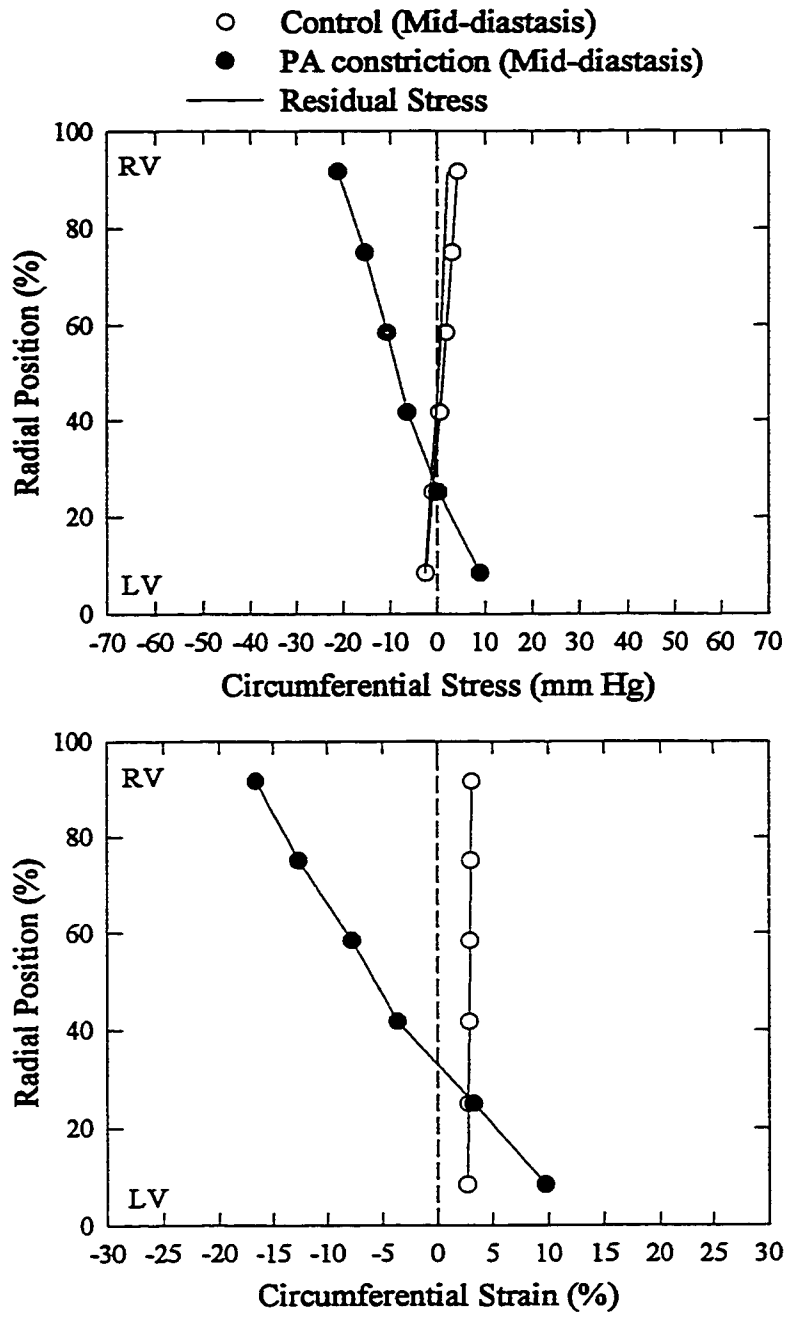

Figure 5.17 Plots of transseptal circumferential stress and strain for control and PA-constriction loading conditions (representative dog, Dog 1) at mid-diastasis.

Figure 5.18 Principal stress vector plots for control and PA-constriction loading conditions (representative dog, Dog 1) at end-diastole (ED). To minimize end-effects, the 4 columns of elements on either side of each mesh are not shown. All the arrows are equally scaled, the magnitude being represented by the size of the paired arrowheads and the distance between them. Whether the stress is tensile or compressive is represented by the direction of the arrowheads, divergent meaning tensile, convergent meaning compressive. Tension and compression generally also correspond to red and blue, respectively.

Control
(End-diastole)

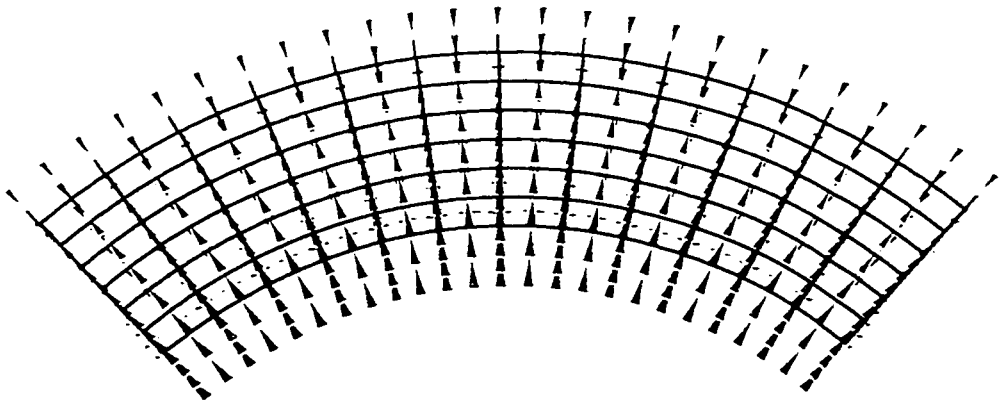

PA constriction
(End-diastole)

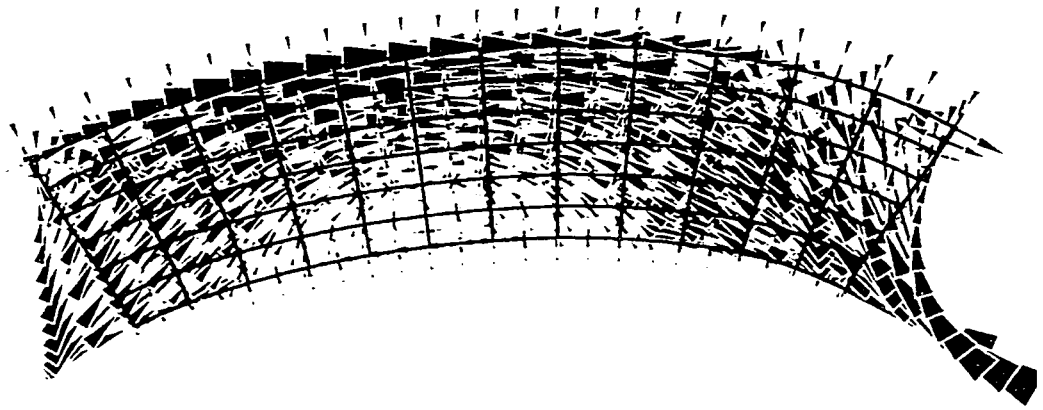

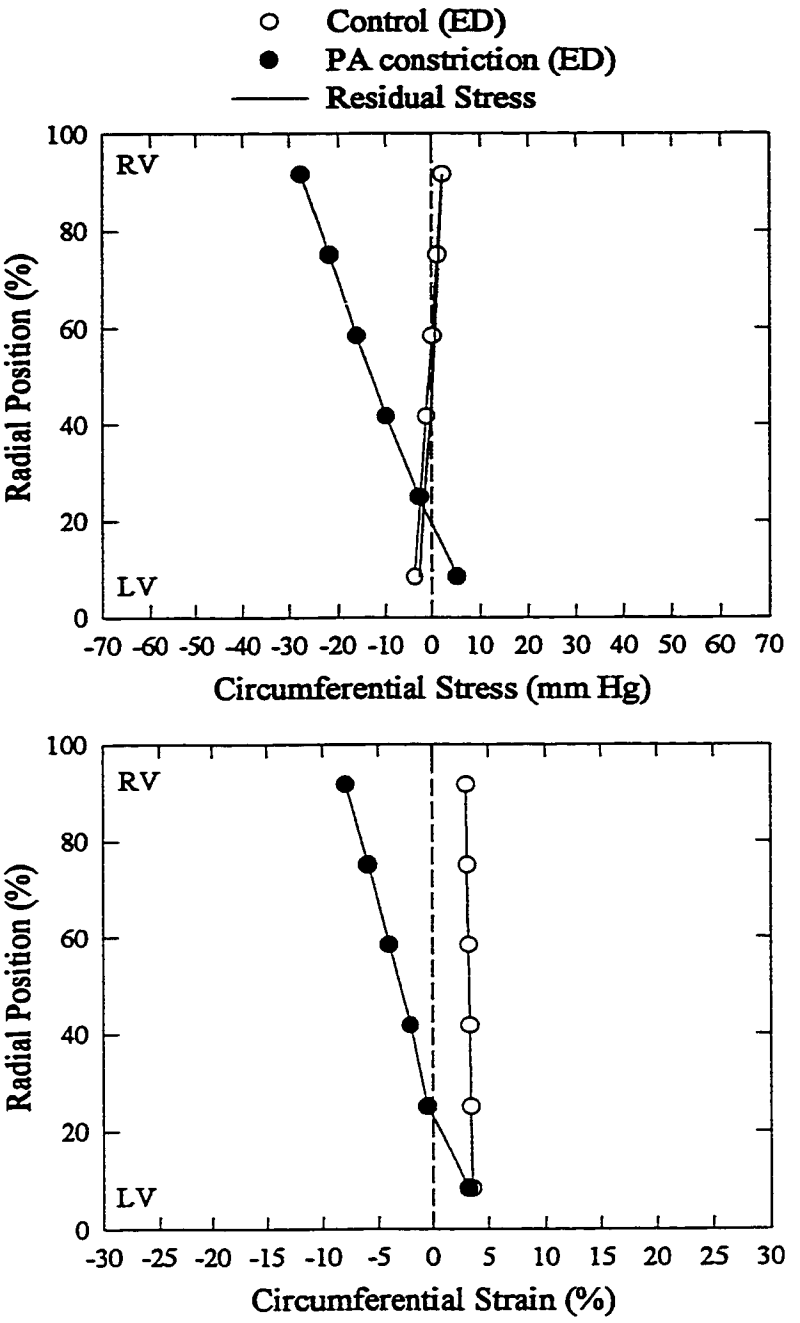

Figure 5.19 Plots of transseptal circumferential stress and strain for control and PA-constriction loading conditions (representative dog, Dog 1) at end-diastole (ED).

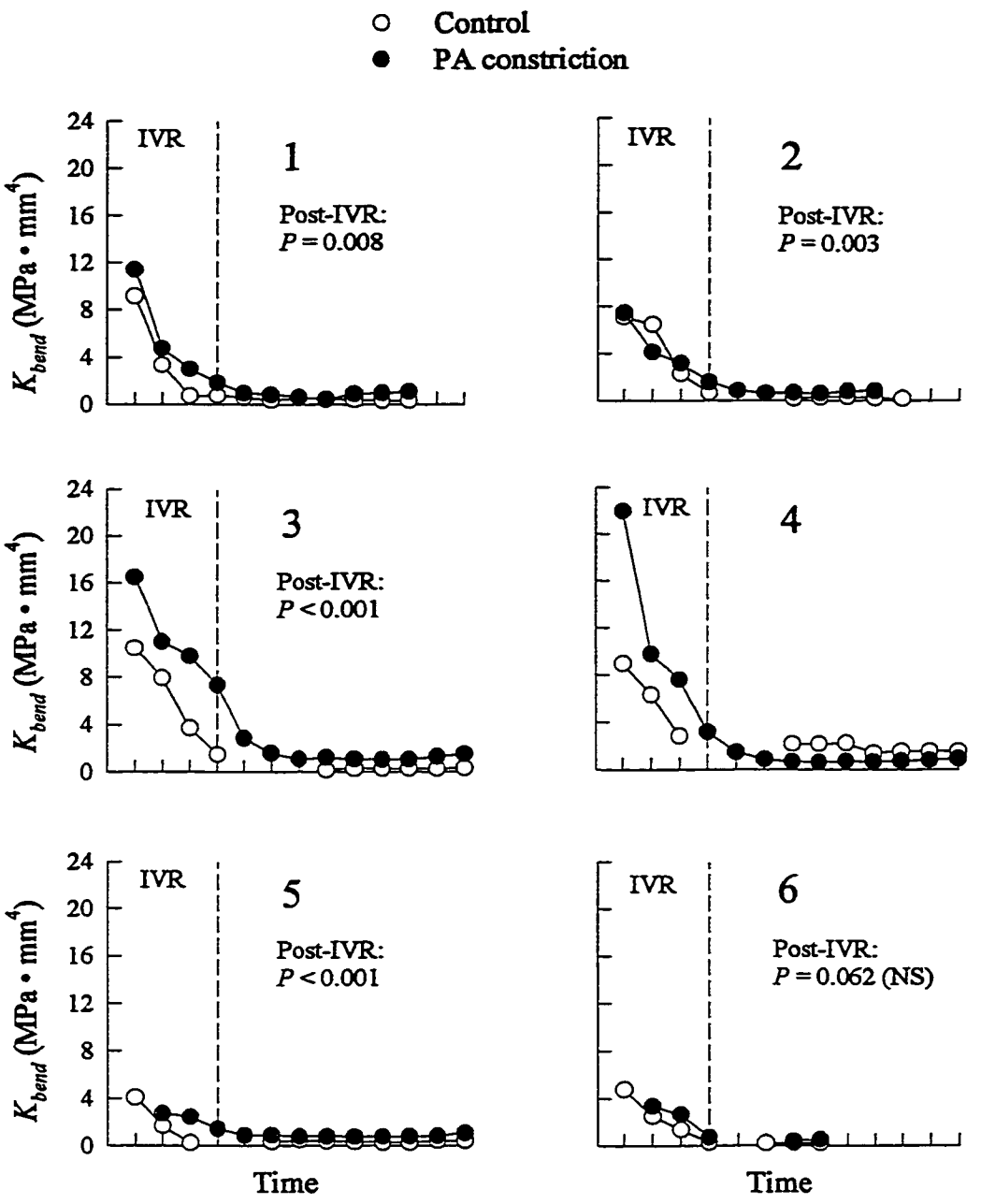

Figure 5.20 Structural bending stiffness (K_{bend}) of the septum plotted as a function of time for control (open circles) and PA-constriction (filled circles) cycles during diastole (end-systole to end-diastole) in all 6 dogs. Each tick on the time axis corresponds to one echo frame. (IVR: isovolumic relaxation period)

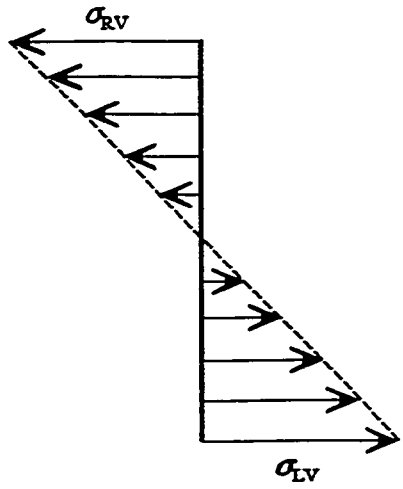

Figure 5.21 Schematic diagram of a circumferential stress distribution across the septum (σ_{RV}, circumferential stress at the RV-septal surface; σ_{LV}, circumferential stress at the LV-septal surface).

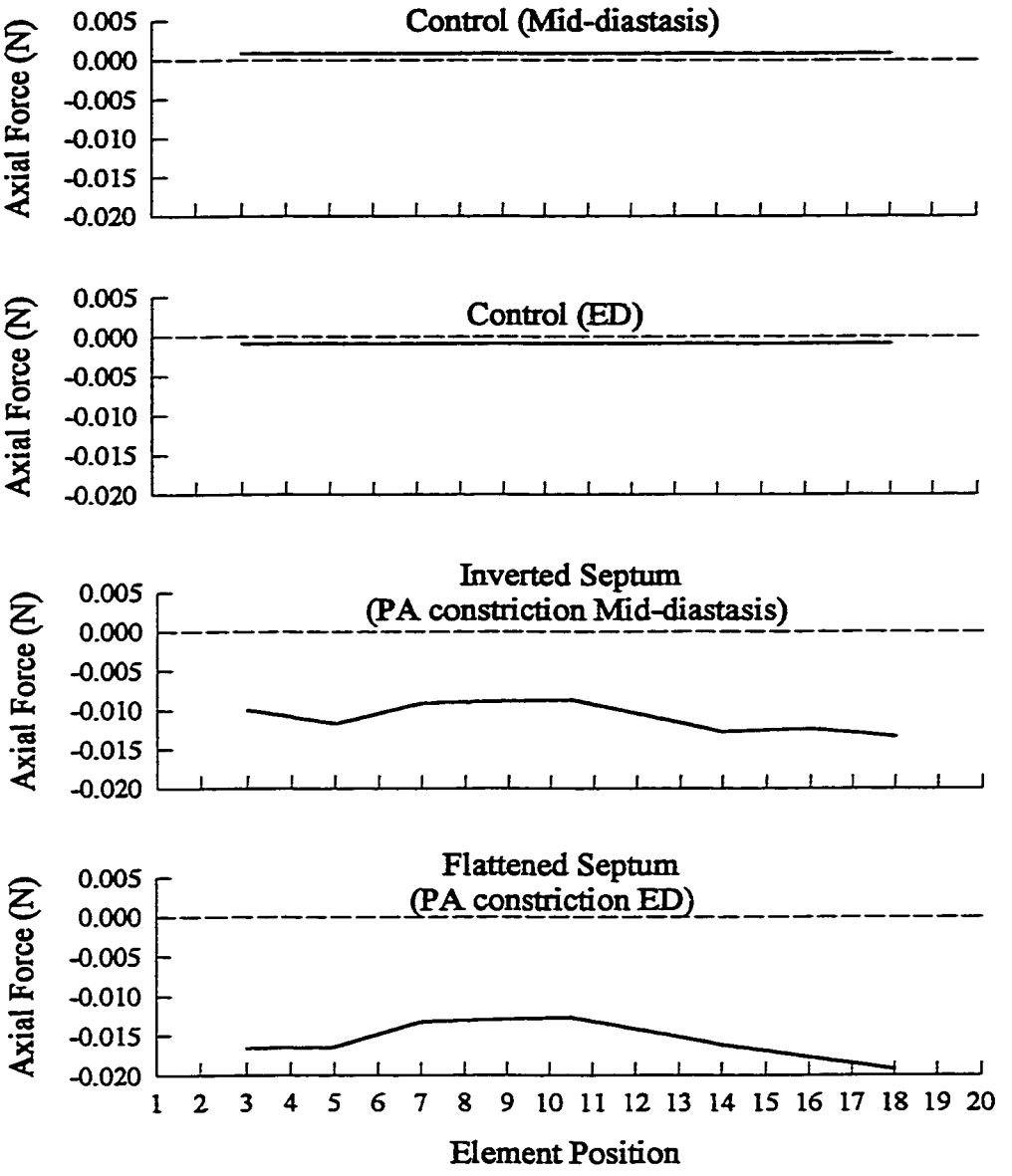

Figure 5.22 Axial force plotted as a function of element column position for control (at mid-diastasis and end-diastole) and PA-constriction (inverted septum and flattened septum) loading conditions (representative dog, Dog 1).

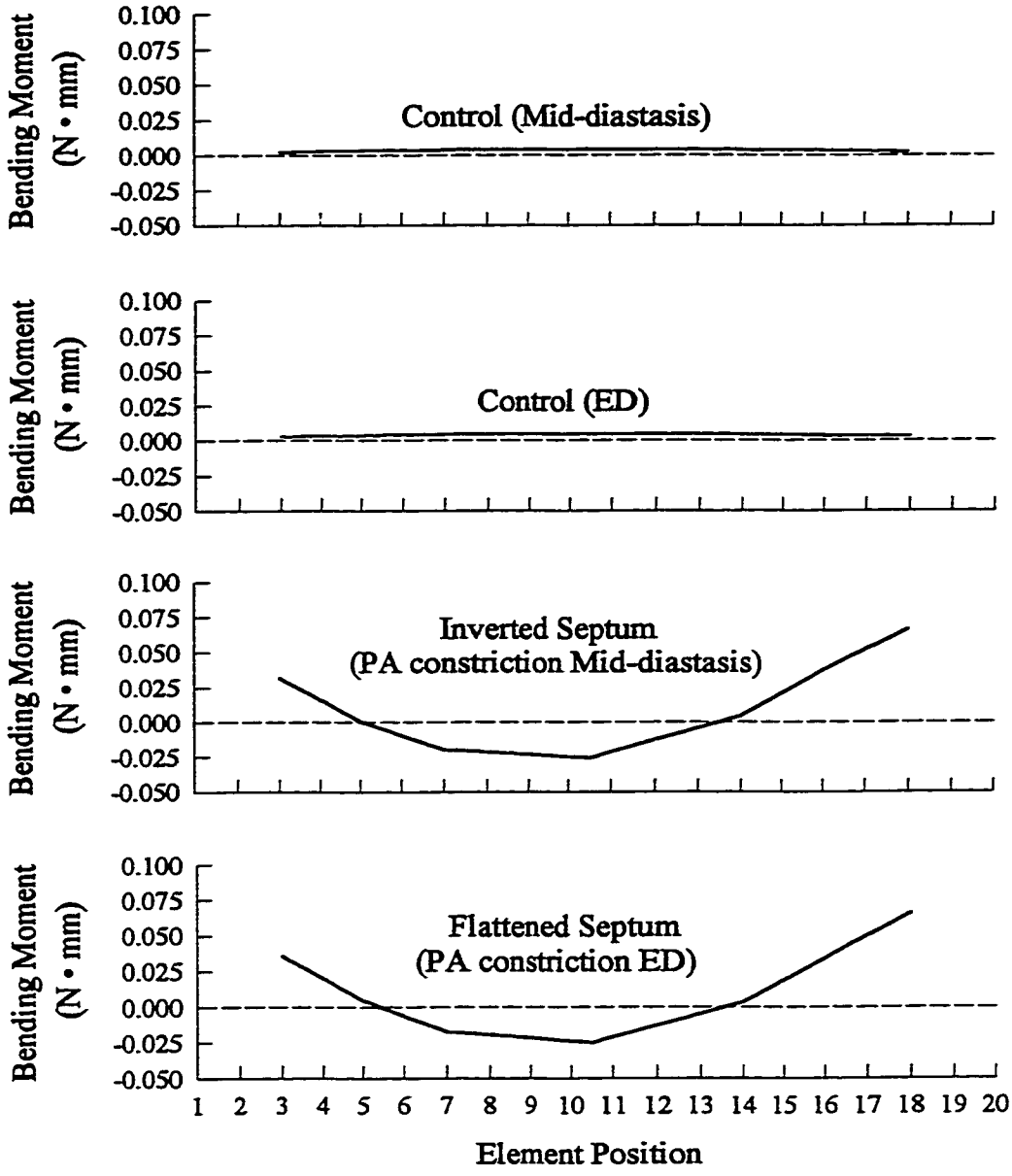

Figure 5.23 Bending moment plotted as a function of element column position for control (at mid-diastasis and end-diastole) and PA-constriction (inverted septum and flattened septum) loading conditions (representative dog, Dog 1).

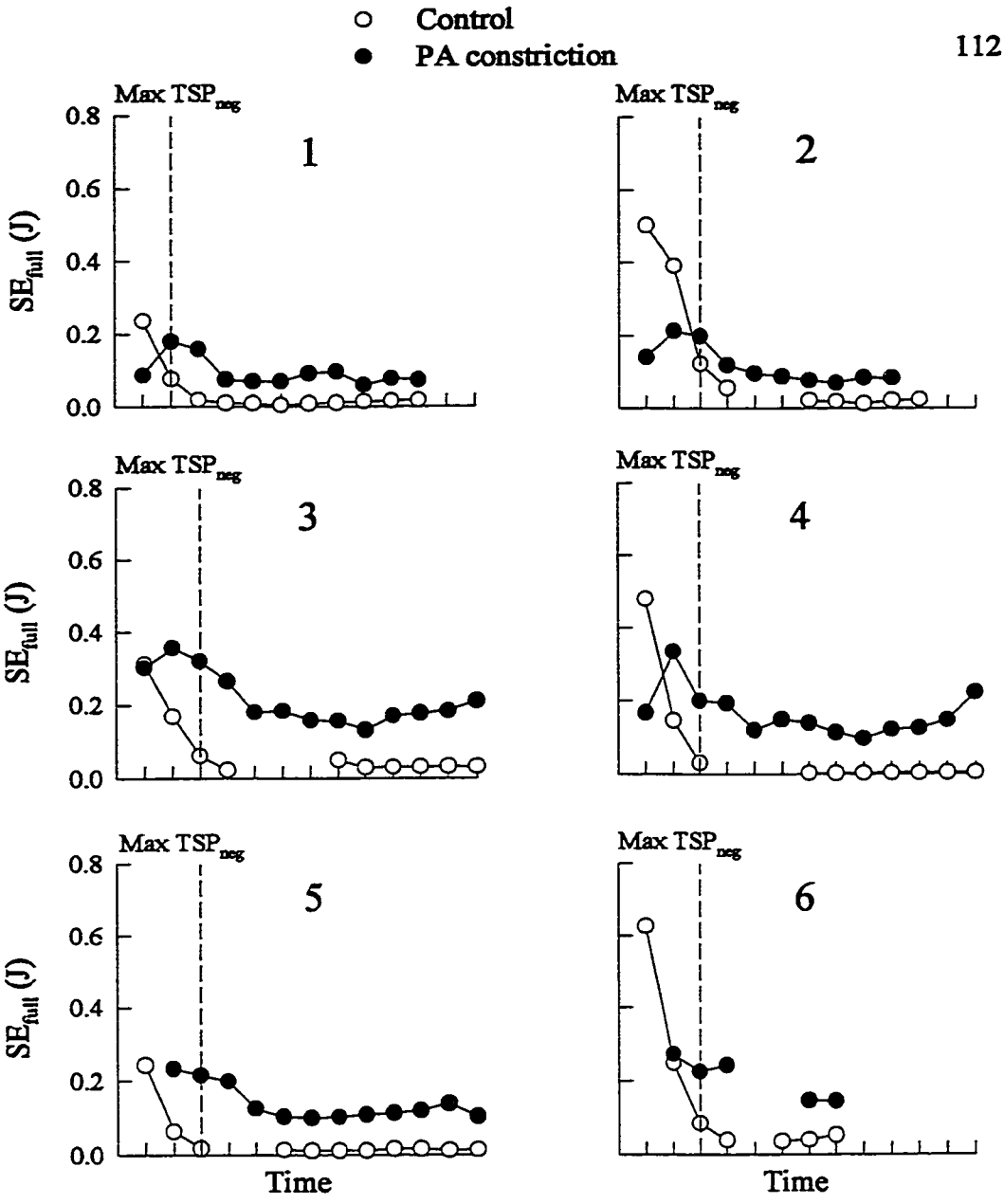

Figure 5.24 Strain energy (SE_{full}, strain energy calculated for the entire mesh) of the septum plotted as a function of time for control (open circles) and PA-constriction (filled circles) cycles during diastole (end-systole to end-diastole) in all 6 dogs. Each tick on the time axis corresponds to one echo frame. (Max TSP_{neg}: maximum negative transseptal pressure gradient)

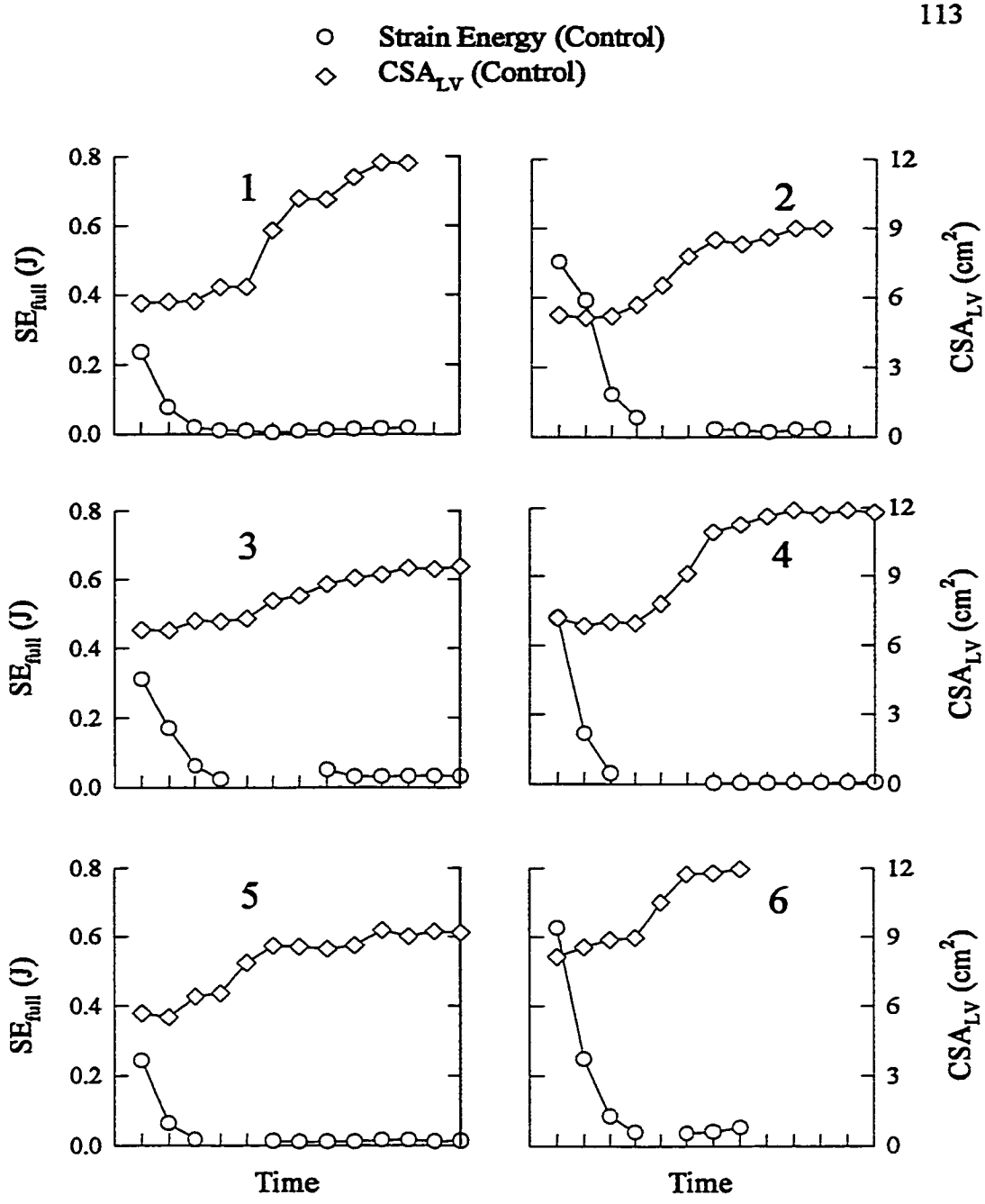

Figure 5.25 Strain energy (SE_{full}, strain energy calculated for the entire mesh; open circles) of the septum and left ventricular cross-sectional area (CSA_{LV}; open diamonds) plotted as a function of time during diastole (end-systole to end-diastole) in all 6 dogs. Each tick on the time axis corresponds to one echo frame.

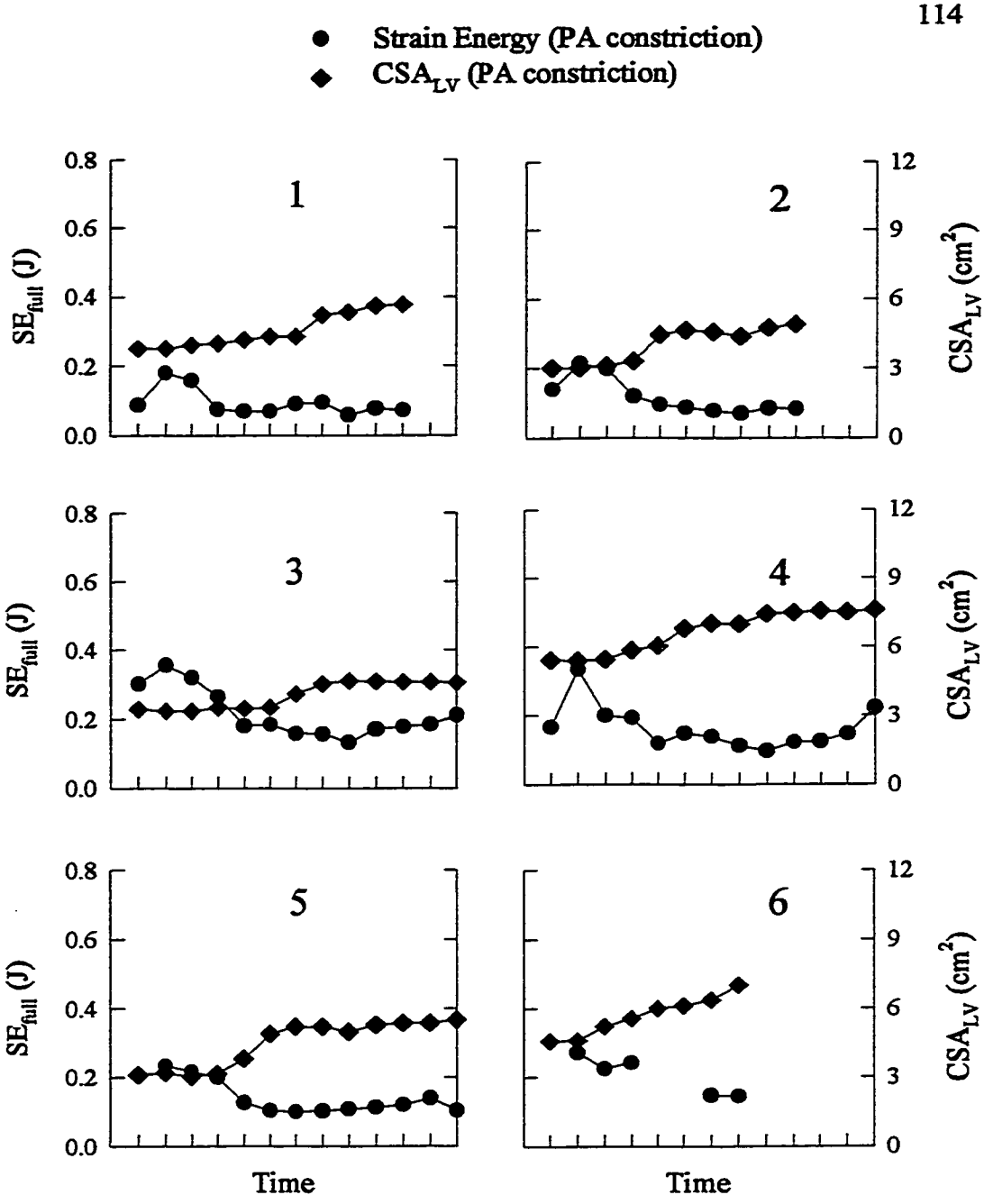

Figure 5.26 Strain energy (SE_{full}, strain energy calculated for the entire mesh; filled circles) of the septum and left ventricular cross-sectional area (CSA_{LV}; filled diamonds) plotted as a function of time during diastole (end-systole to end-diastole) in all 6 dogs. Each tick on the time axis corresponds to one echo frame.

Table 5.2 SE_{60} (strain energy calculated for 60% of the mesh) expressed as a percentage of SE_{full} (strain energy calculated for the entire mesh) during control and PA constriction at Max TSP_{neg} and ED. (For control, a position equivalent in time to Max TSP_{neg} during PA constriction was chosen, i.e., near completion of IVR period.)

		SE_{60}/SE_{full} x 100 (%)	
	Dog	Control	PA constriction
Max TSP_{neg}			
	1	59.7	17.2
	2	51.6	13.1
	3	56.5	12.5
	4	58.1	15.0
	5	61.1	13.9
	6	55.3	17.8
	Mean ± SD	57.1 ± 3.4	14.9 ± 2.2
ED			
	1	61.1	20.5
	2	62.5	24.1
	3	59.4	14.2
	4	48.4	22.5
	5	60.0	15.5
	6	61.5	27.6
	Mean ± SD	58.8 ± 5.2	20.7 ± 5.1

SD, Standard Deviation

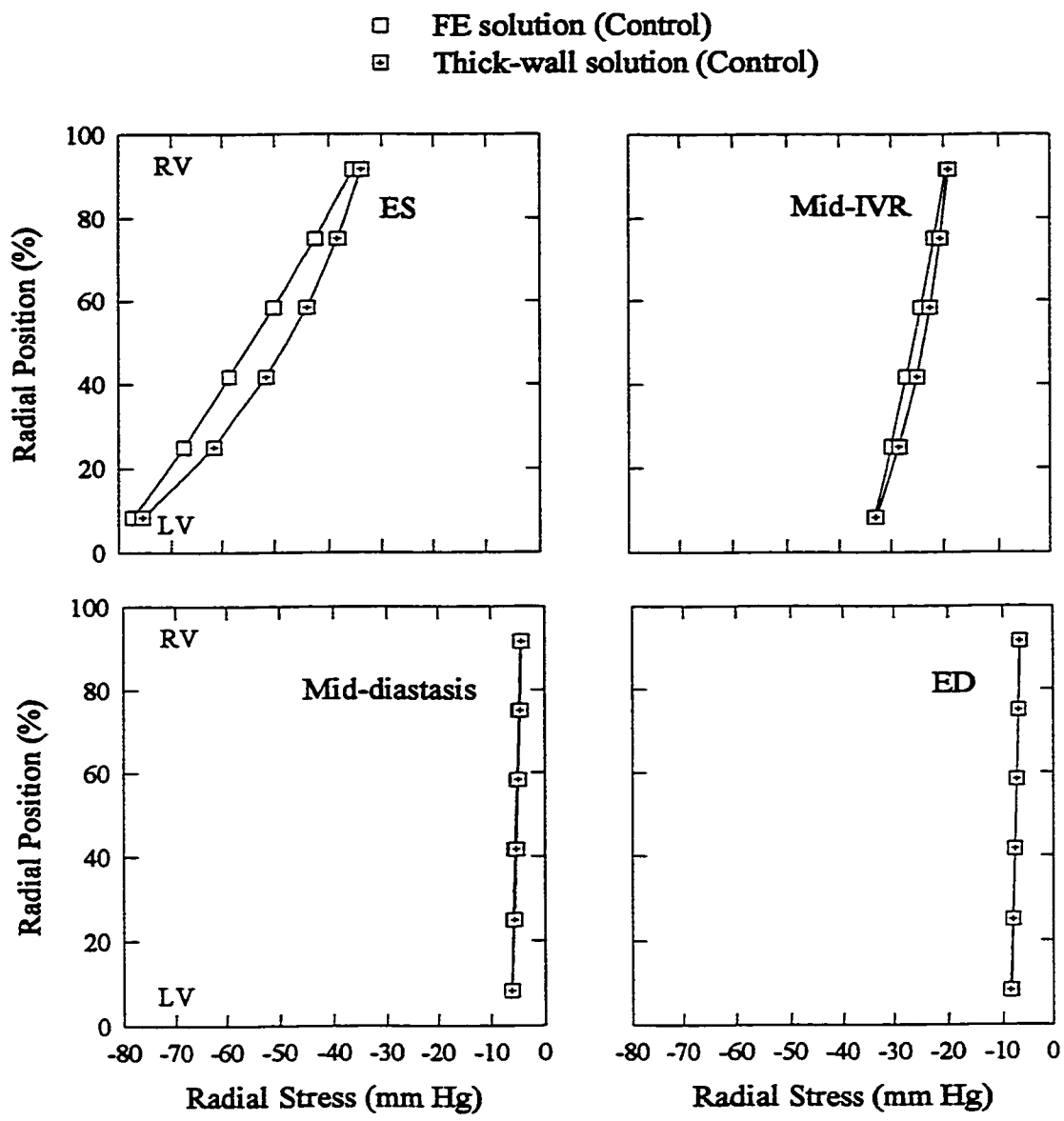

Figure 5.27 Comparison of transseptal radial stress values calculated by the finite element model (open squares) and a thick-wall solution (crossed squares) during control (at end-systole, ES; mid-isovolumic relaxation, Mid-IVR; mid-diastasis; end-diastole, ED). Values shown are from a representative dog (Dog 1).

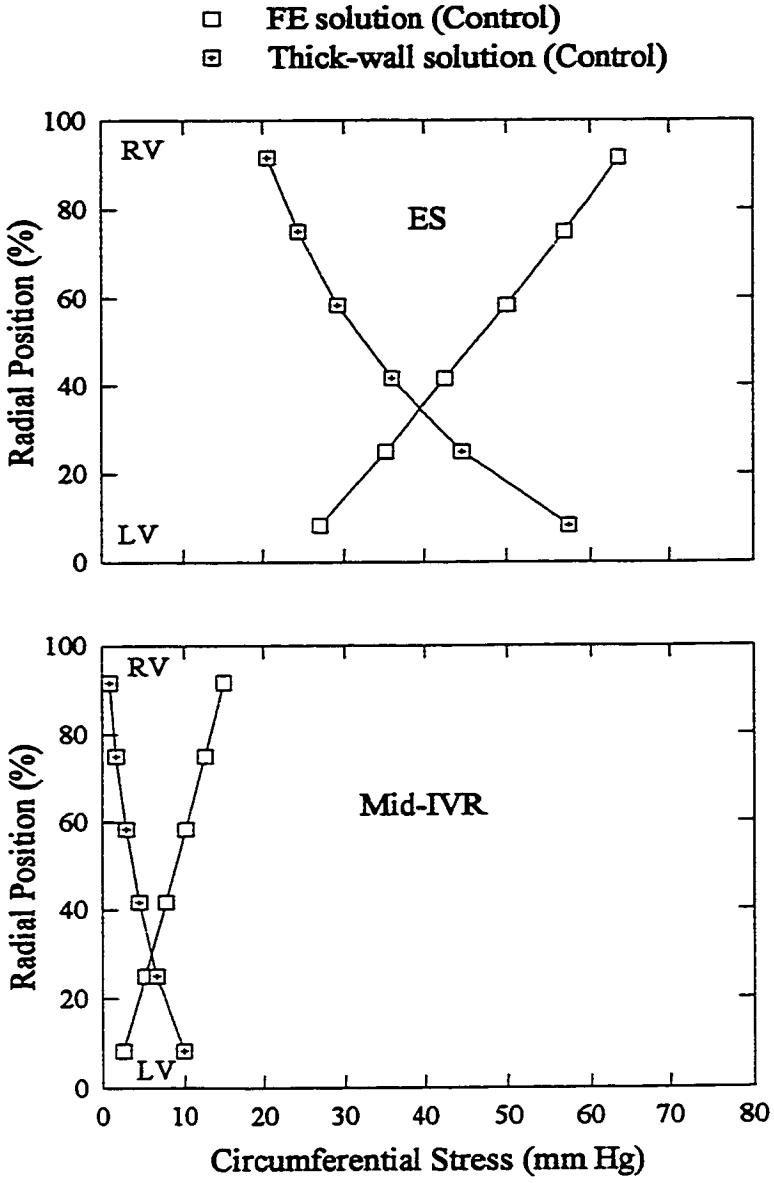

Figure 5.28 Comparison of transseptal circumferential stress values calculated by the finite element model (open squares) and a thick-wall solution (crossed squares) during control (at end-systole, ES; mid-isovolumic relaxation, Mid-IVR) Values shown are from a representative dog (Dog 1).

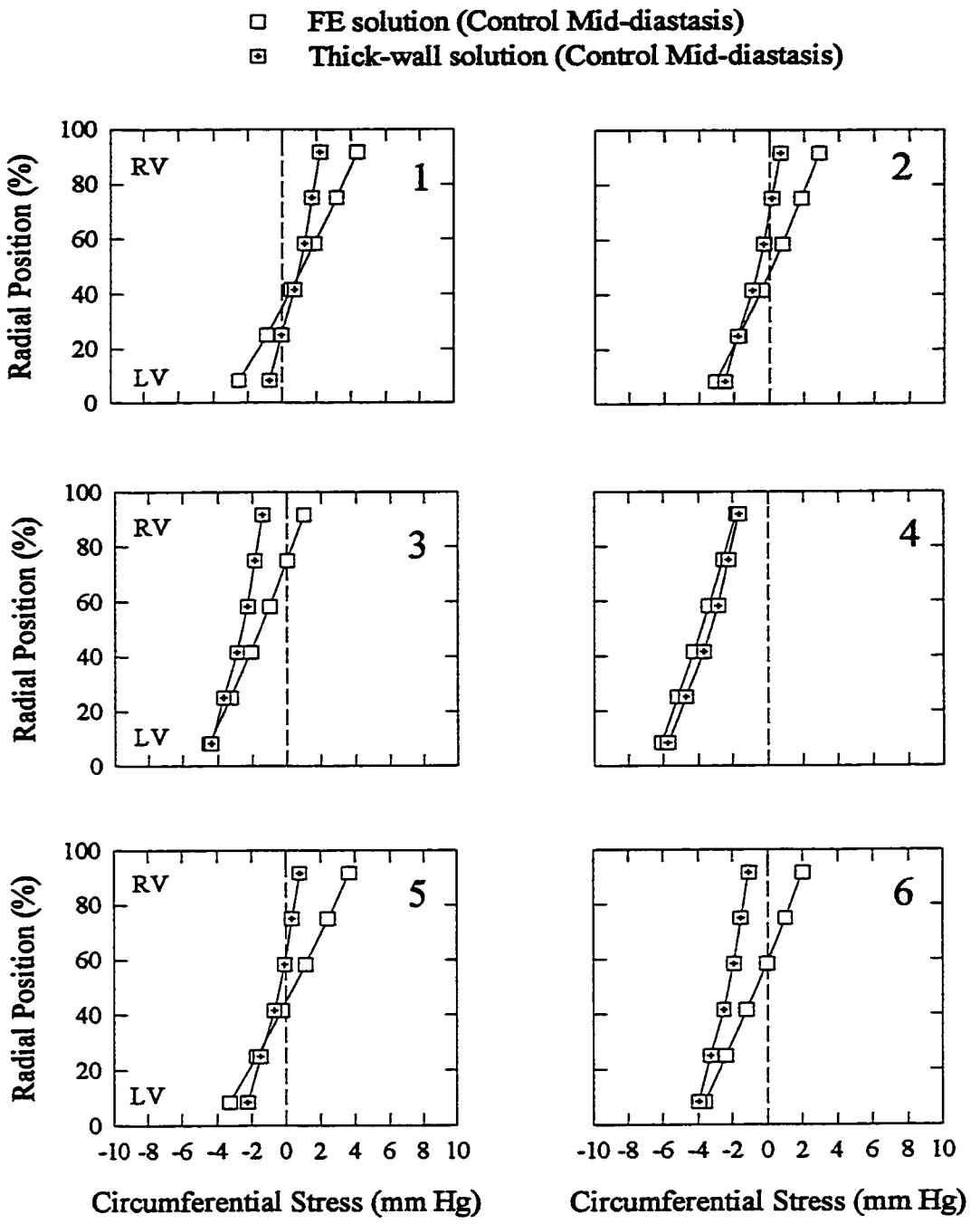

Figure 5.29 Comparison of transseptal circumferential stress values calculated by the finite element model (open squares) and a thick-wall solution (crossed squares) during control (mid-diastasis) in all 6 dogs.

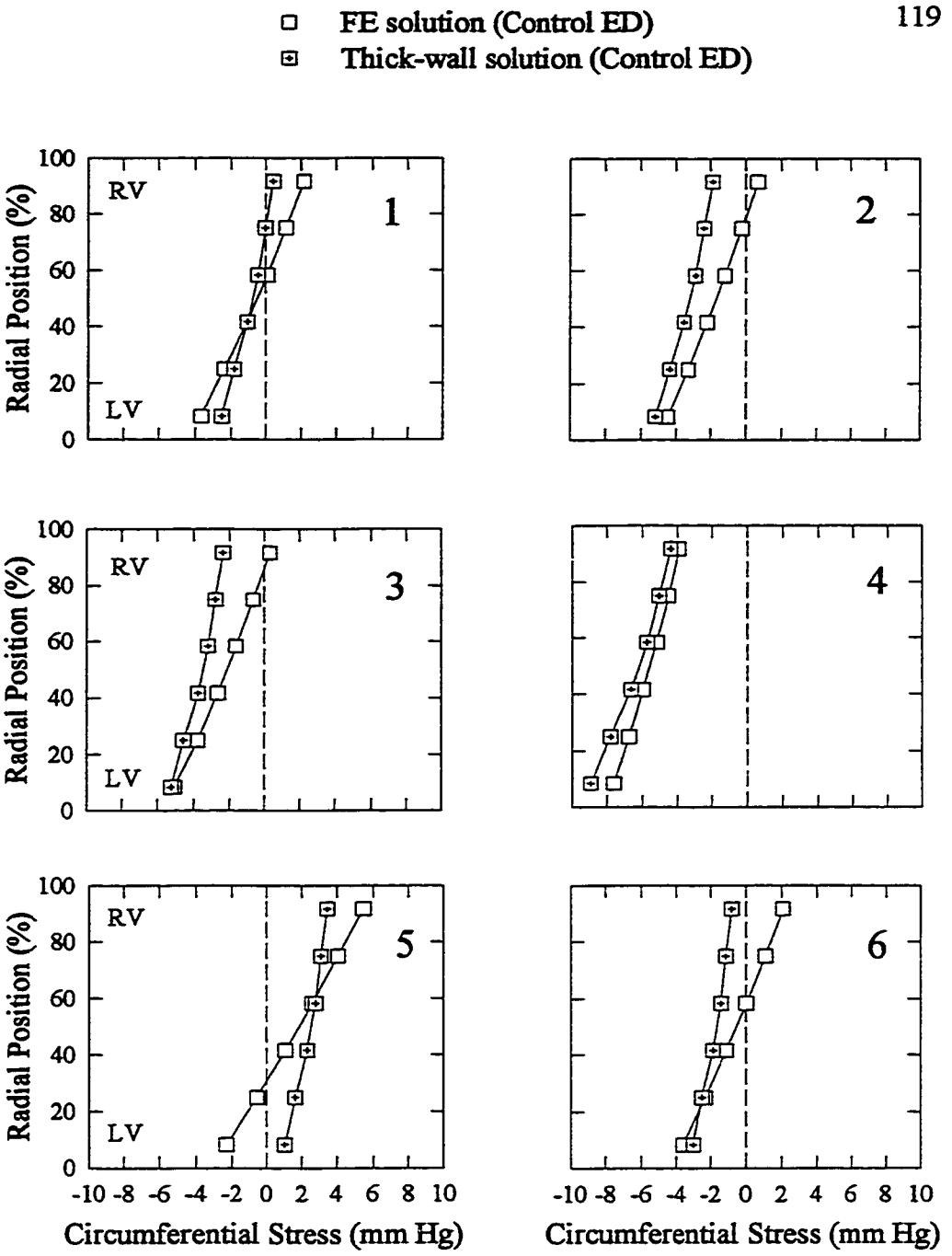

Figure 5.30 Comparison of transseptal circumferential stress values calculated by the finite element model (open squares) and a thick-wall solution (crossed squares) during control (at end-diastole, ED) in all 6 dogs.

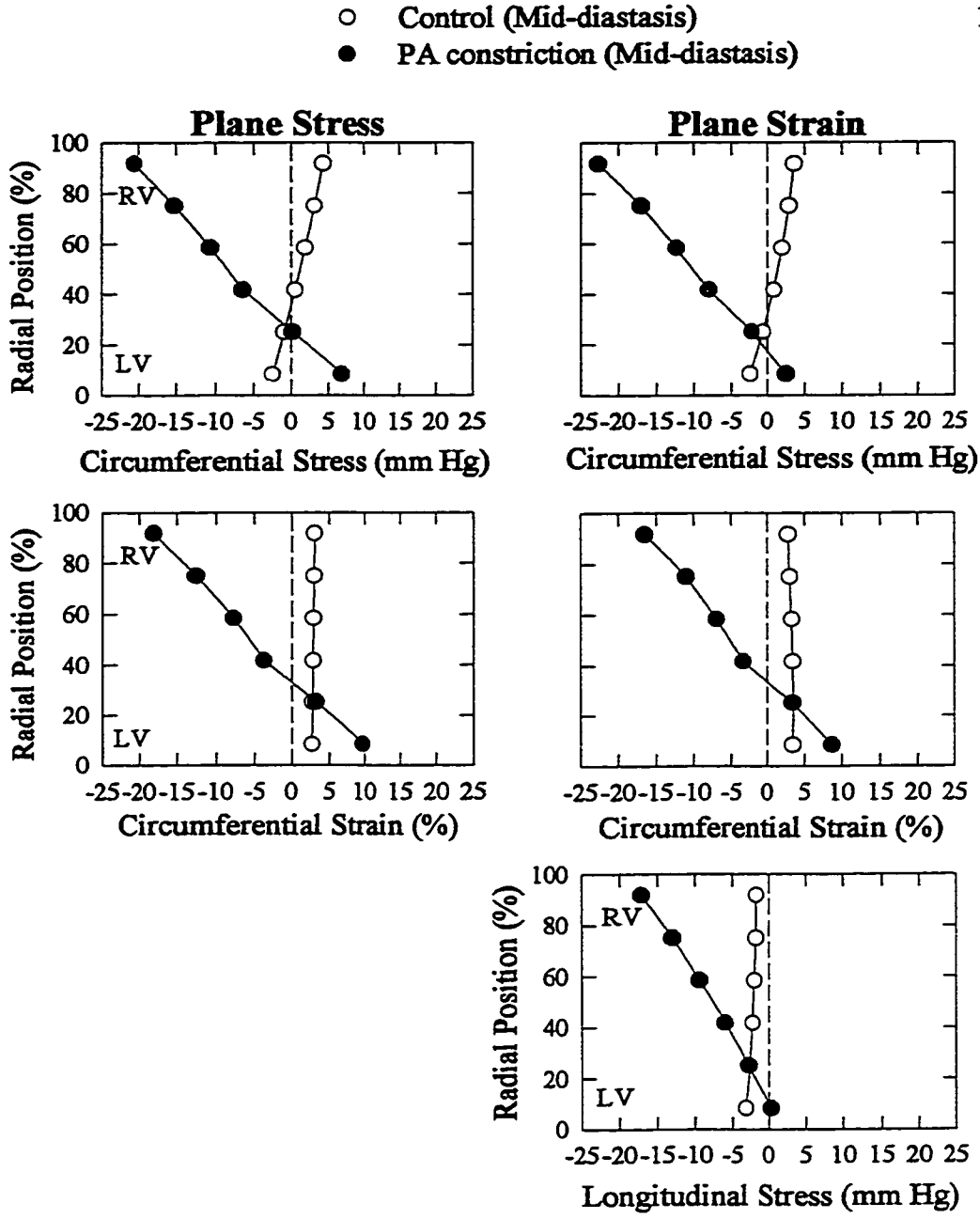

Figure 5.31 Comparison of stress and strain values obtained from finite element meshes constructed using either plane stress or plane strain elements (control and PA constriction at mid-diastasis). Values shown are from a representative dog (Dog 1).

CHAPTER 6

DISCUSSION

The following discussion is divided into 3 sections: (1) the effect of PA constriction on hemodynamics and septal geometry, (2) model findings and considerations, and (3) conclusions.

6.1 Effect of PA Constriction on Hemodynamics and Septal Geometry

As expected, PA constriction induced marked changes in the measured pressures and geometry of the septum, relative to control in all 6 dogs. RVP increased (see Figure 5.2) during PA constriction, undoubtedly because of the barrier to outflow imposed by constriction of the PA. Conversely, LVP decreased (see Figure 5.1) during PA constriction presumably on account of reduced pulmonary venous return, evidenced by the substantial reduction in CSA_{LV} (an indicator of intracavitary LV volume, see Figure 5.4) and leftward shift of the LVP-CSA_{LV} curves (see Figure 5.5). The severity of PA constriction is further emphasized by the reduction in mean diastolic AoP which occurred (shown in Table 5.1). The increase in RVTMP (see Figure 5.7) during PA constriction relative to control was largely due to the increase in RVP (see Figure 5.2) which occurred under the same conditions. The RVTMP was reduced, however, relative to RVP during PA constriction, reflecting regional pericardial distension over the dilated RV, i.e., increased RVP_{peri} (as shown previously by Smiseth et al[137]). Similarly, LVTMP (see Figure 5.6) was reduced during PA constriction relative to control largely on account of the reduced LVP (see Figure 5.1). LVTMP was reduced relative to LVP, because of regional pericardial distension over the LV free wall, i.e., increased LVP_{peri}. The proposed mechanism being

that the dilated RV pushes the heart leftward, with a resulting increase in pericardial pressure over the LV free wall.[137]

Although the magnitude and temporal trend of TSP (see Figure 5.3) during PA constriction was similar in all 6 dogs, surprisingly, the degree of flattening and inversion (reflected in the curvature vs. time plots, see Figure 5.8) observed was different. Three of the 6 dogs showed inversion (one of which only transiently), while the other 3 only showed flattening, indicating markedly different responses to similar loading conditions. With reduction in the intracavitary LV volume (supported by the reduced CSA_{LV}, see Figure 5.4) which occurred during PA constriction, the concomitant increase in thickness (see Figure 5.10) relative to control was expected since the mass of the LV and septum must be conserved. A decrease in L_{IP} (see Figure 5.9) during PA constriction (relative to control), however, which would have been expected based on the preceding argument, was not observed.

6.2 Model Findings and Considerations

6.2.1 Increased K_{bend} and G during PA Constriction

As suggested by a pressure-volume loop, G (see Figure 5.11) and K_{bend} (see Figure 5.20) for both control and PA constriction decreased from ES to a near-stable value for the remainder of diastole. The model, however, suggests that K_{bend} (which is the resistance of the structure to bending in the face of lateral loading) during PA constriction was greater than during the control loading conditions. Since thickness was included in the calculation

of K_{bend}, the increase in G which the model required during PA constriction (in order for satisfactory matches to be obtained) must be explained. It is unlikely that the difference in G resulted from changes in endosarcomeric (e.g., titin) or extracellular-matrix (e.g., collagen) proteins because the PA was constricted for less than 30 s. G may have increased owing to an increase in coronary venous pressure. In isolated, perfused dog hearts, Watanabe et al[160] raised coronary venous pressure by increasing RA/RV pressure, and showed LVEDP (an indicator of LV stiffness) increased significantly at the same LV volume. They also showed that coronary venous pressure was more effective in raising LVEDP than coronary arterial pressure in the range tested. They suggested that this apparent increase in stiffness was related to an increase in intramyocardial blood volume,[74,87] as opposed to either increased pressure or flow. Similarly, Resar et al[123] have shown that transverse stiffness (which is analogous to K_{bend} in this study) increased at least twofold as a result of an increase in coronary arterial perfusion pressure from 20-80 mm Hg. Therefore, coronary venous congestion following PA constriction may be sufficient to explain the increase in K_{bend} (via an increase in G) predicted by the model.

The fact that G and K_{bend} were greater during the post-IVR control period in Dog 4, and that at certain locations during both control and PA constriction, matches between the measured and model derived deformations could not be obtained (i.e., so-called dropout occurrences), requires explanation. For the last 7 control loading conditions in Dog 4, the TSP was approximately 0 mm Hg (see Figure 5.3). This interval coincided with approximately the end of the rapid filling phase of the LV until the end of diastole (see last

7 CSA_{LV} points in control Dog 4, Figure 5.4). For all other dogs, the TSP in this period was between 2 and 5 mm Hg. Recall, the initial RS mesh was determined based on the control loading and curvature of the septum at ED and then the geometry was adjusted accordingly (i.e., for thickness and idealised SL) for further analysis during diastole. Because TSP was approximately 0 mm Hg, the curvature of the RS mesh was equal to that of the measured curvature of the septum at ED. However, in order to prevent the mesh from collapsing downward, towards the centre of the LV cavity (the downward thrust of RVP had a greater effect on the structure than the upward thrust of LVP even though TSP ≈0 mm Hg), G had to be increased (coincidentally, above that required to obtain matches during PA constriction in this same period). Whether the requirement for an increased G over this interval is true or rather an artifact of the model cannot be determined. Furthermore, what role an abnormally stiffened septum might play in preventing an otherwise positive TSP from developing is not readily understood.

In all dogs except Dog 1, dropout occurred during control in the interval coinciding approximately with the rapid filling phase of the LV (see CSA_{LV} vs. time plots, Figure 5.4, where CSA_{LV} increased rapidly). Over this interval, septal L_{IP} increased (see Figure 5.9) and septal curvature decreased (see Figure 5.8), both of which were expected based on the fact that the LV volume increased rapidly during this period. Furthermore, the TSP in this period was between 0.5 and 1.5 mm Hg (in Dogs 2, 3, 5, and 6). Dropout occurred because convergence could not be obtained when G was lowered below a particular threshold, i.e., even though the geometry of the RS mesh was adjusted according to

idealised SL (with a resulting increase in L_{IP} and decrease in curvature), G could not be lowered to a level such that the net positive TSP had an "upward" thrust thereby allowing a satisfactory match to be obtained. The LVP-CSA_{LV} curves (see Figure 5.3) suggest that the stiffness of the LV (and septum) should approach a minimum at this point in diastole – something which the model seems to suggest as well. In Dog 4, the TSP during control was slightly negative over this interval, loading which was incompatible with the observed deformation. Similarly during PA constriction, in Dogs 5 and 6 at ES, and in Dog 6 mid-way through diastole, TSP was incompatible with the observed deformations and therefore, matches could not be obtained.

6.2.2 End-Bending Moment Requirements during PA Constriction

The requirement for greater end-bending moments during PA constriction (they were not required during control) near ES (see Figure 5.12) relative to the rest of diastole is consistent with the septum being much stiffer (both G and K_{bend} were greatest near ES, see Figures 5.11 and 5.20, respectively) during this part of the cycle.

Furthermore, the requirement for greater end-bending moments at the anterior insertion point (compared to the posterior insertion point) reflects asymmetric flattening and inversion of the septum. Specifically, the curvature of the septum was greatest near the anterior insertion point, and thus greater end-bending moments were required in order for matches to be obtained in this region of the septum. The asymmetry likely results from the septum being constrained at the anterior side more so than at the posterior side. Whether

this constraint is due to an anatomical difference in the 2 insertion points or because of some artificially imposed boundary (e.g., the dog was in the supine position during echocardiographic recording) has yet to be determined.

6.2.3 Arch-like Behaviour of the Distorted Septum

Compared to the stresses which developed during the control cycle, the substantial circumferential compressive stress distribution which developed in the PA-constriction loading conditions (see Figures 5.14 to 5.19) suggests an arch-like behaviour of the septum under these severe conditions. Recall, the arch is a structural system in which the primary internal force is axial compression.[24] Like an arch, the septum bears the PA-constriction loading by distributing the net "downward" thrust of the load laterally, through a pattern of compressive stress towards its "supports," which, although not shown, seem to be the RV insertions.

Compression in the septum has been suggested previously by Pao et al[114] and Heethaar et al[57] (see Chapter 2, Analysis of Stress in the Heart). However, the arch-like distribution of stresses shown here, with, specifically, maximum compression occurring at the RV-septal surface, is a novel finding. Furthermore, the model is the first to demonstrate that this behaviour is sustained during diastole in all dogs analysed (many previous investigators have limited their analysis to ED only). At Max TSP_{neg}, the greatest compressive stresses were observed, with the smallest corresponding strains (see Figure 5.15). This is consistent with the fact that during PA constriction, a greater G was required

at Max TSP_{neg} in all 6 dogs (see Figure 5.11; compared to the remainder of the diastolic interval), in order to match the RS mesh satisfactorily to the observed shape of the septum. It is plausible that the *G* required at Max TSP_{neg} be greater than for the remainder of diastole because even though the net downward force was at its greatest in the cycle, the curvature was still near its maximum (see Figure 5.8). For the inverted septum which occurred at mid-diastasis in Figure 5.16 (in the 3 dogs of the 6 which inverted, inversion occurred at approximately mid-diastasis and beyond), the smallest compressive stresses were observed with the largest corresponding strains (see Figure 5.17). This is opposite to what occurred at Max TSP_{neg} and is consistent with the fact that the *G* required in the mid-diastasis interval during PA constriction was near minimum in all dogs except Dog 6 (see Figure 5.11; for Dog 6, matches could not be obtained, but the other points suggest the same trend). It is plausible that the *G* required at mid-diastasis be at a minimum for the cycle since TSP was the least negative (see Figure 5.3) and the septum was also near its maximum deformation (see Figure 5.8) at this point in the cycle in all 6 dogs. The magnitude of the circumferential compressive stresses and corresponding strains at ED (see Figure 5.19) appeared to be somewhere in between that obtained for Max TSP_{neg} and mid-diastasis. This is consistent with the fact that the *G* required at ED was greater relative to that at mid-diastasis but still less than that required at Max TSP_{neg} (see Figure 5.11). This, in turn, is consistent with the TSP becoming more negative towards ED (but less than that at Max TSP_{neg}) with the flattening or inversion of the septum becoming less severe.

A degree of circumferential tension developed on, and slightly below the LV-septal

surface during PA constriction in all dogs. The magnitude of this tension was greater when the septum inverted (e.g., see Figures 5.16 and 5.17) as opposed to when it only flattened (e.g., see Figures 5.18 and 5.19). This observation is consistent with that made in a previous study from our laboratory in which septal segment length was measured using sonomicrometry crystals that were positioned circumferentially, approximately half-way between the RV- and LV- septal surfaces.[33] It was a surprise to find that the segment did not lengthen, even with extreme degrees of septal inversion. It had been assumed that the septum behaved like a thin-walled membrane and it therefore was reasoned that large negative values of TSP would (re-) lengthen the segment, but this was never observed. However, as was speculated at the time, because the crystals had not been placed very close to the LV-septal surface, lengthening perhaps should not have been expected.

6.2.4 Comparison of Control Results with Thick-Walled Model

Given the complexity of deformations (i.e., flattening and inversion of the septum) observed during PA constriction, an attempt to provide validation of the FE results with those obtained from an analytical solution was not feasible because such a solution is either nonexistent or the equations involved are mathematically intractable. Comparison of the control results, however, was possible.

Although similar radial stresses (see Figure 5.27) were calculated by both FE and thick-walled solutions for the entire diastolic interval (i.e., ES to ED) in all dogs analysed, it was not the case for the circumferential stresses. At ES and mid-IVR (see Figure 5.28),

agreement between the 2 solutions was poor but, at mid-diastasis (see Figure 5.29) and ED (see Figure 5.30), the agreement was strong. The discrepancy most probably relates to the fact that the thick-walled solution is based on an assumption of axisymmetric deformation of a cylindrical cross-section (i.e., when the septum and LV free wall are connected with equivalent curvature) whereas the FE model assumes the septum is isolated from the rest of the heart (i.e., analysis of the septum in its free-body form). In the thick-walled cylindrical solution, an inward acting (negative) bending moment develops around the circumference of the section due to the applied pressure loading, which thereby prevents the circumferential tensile gradient from becoming greatest at the exterior of the wall (consistent with the thick-walled and FE models described previously[45,47,71,96,113,162]). In the FE model of the isolated septum presented here, it was not possible to account for this type of inward acting (negative) bending moment at the ends of the mesh and still match the observed shape of the septum during control (as the application of a negative bending moment at the ends produced irregular shapes). Agreement between the 2 solutions at mid-diastasis and ED is undoubtedly related to the fact that the residual stresses changed the stress gradient obtained by the thick-walled solution because the magnitude of stress calculated was so small to begin with at this point in the cycle (the residual stress had little effect on the stress gradient when TSP was high). It follows that, although the FE model may well handle the complex deformations which occur during PA constriction because application of positive bending moments (upward acting) at the ends of the mesh (which are required in order for appropriate matches to be obtained) is practical, adjustments to the

boundary conditions need to be examined for modelling control loading conditions when TSP is high. Finally, it is emphasized that, although agreement between the 2 solutions is poor when control TSP is high, this does not necessarily indicate that the results obtained from the FE solution are wrong (or that the results from the thick-walled solution are right, for that matter). The thick-walled cylindrical solution does not take into account the difference in loading between the septum and the LV free wall (and the slight curvature difference which exists during control), and furthermore, does not allow for any change at the RV insertions. The free-body approach to analysis of the septum, which was used in the FE model presented here, was chosen in order to investigate primarily the structural behaviour of the septum when it flattens and inverts during PA constriction. This approach, although limited with respect to the practical application of negative bending moment at the insertions during control (as mentioned above), allows for the demonstration of structural principles (specifically, variation of bending moment in the septum, see next section) which otherwise would not have been determined had a thick-walled solution been employed (the thick-walled solution cannot deal with varying bending moment around the section).

6.2.5 Variation of Axial Force and Bending Moment in the Septum

Although the magnitude of the axial force (see Figure 5.22) at control mid-diastasis and ED (compared to PA constriction) could be declared negligible, the opposing signs of axial force calculated for the 2 control situations demonstrates a variation depending on the predominant stress, as opposed to the circumferential stress gradient which develops across

the septum (i.e., the gradient developed between LV- and RV-septal surfaces). If the predominant circumferential stress is tensile (which was the case for the control example at mid-diastasis, see stress plots in Figures 5.16 and 5.17), then the axial force will be positive. If the predominant circumferential stress is compressive (which was the case for the control example at ED, see Figures 5.18 and 5.19), then the axial force will be negative. Consequently, the axial force calculated for both the inverted septum and flattened septum examples in Figure 5.22 was negative and of substantially greater magnitude than the controls, because the predominant circumferential stress throughout PA constriction was compressive. The variation in axial force which was observed through the length of the septum for both the inverted and flattened examples is explained by the variation in magnitude of circumferential compression observed throughout the length of the structure. In general, greater compression was observed near the ends of the septum (as compared to the middle) with, therefore, correspondingly greater negative axial force.

The bending moment diagrams (see Figure 5.23) show positive bending moment for both control mid-diastasis and ED examples, even though axial force was calculated as positive and negative, respectively, for the 2 cases. This demonstrates that bending moment depends on the circumferential stress gradient which develops across the structure rather than the predominant circumferential stress. For both control examples, the circumferential stress gradient from the LV-septal surface to the RV-septal surface was compressive to tensile. Therefore, the bending moment was calculated as positive. Consequently, the bending moment calculated for both the inverted septum and flattened septum examples

show variation about the 0 N • mm line since the circumferential stress gradient reversed at two locations. Before element position 5, the bending moment was positive (consistent with all *end*-bending moments at the posterior insertion point, see Figure 5.12) because the stress gradient across the septum was compressive to tensile. From element position 5 through 14, the bending moment was negative because the stress gradient reversed, becoming tensile to compressive. Finally, after element position 14, the bending moment became positive again (consistent with all *end*-bending moments at the anterior insertion point, see Figure 5.12) because the stress gradient again became compressive to tensile. These results make sense from a structural mechanics viewpoint. In Figure 6.1a, a beam with fixed ends is subject to uniformly distributed loading. The deformation and corresponding bending moment diagram (Figure 6.1b) are similar to those obtained by the model (Figure 1.7b and bottom 2 panels of Figure 5.23, respectively). Specifically, inversion is maximal near the middle of the septum (see inverted septum, Figure 5.16), the zero moment points coincide approximately with the points of inflection, and the maximum (absolute) bending moment is achieved at the ends (i.e., at the RV insertions). The similarity just described gives confidence that the model is predicting the structural behaviour correctly, but perhaps more importantly, also confirms the necessity and importance of including bending effects in the model.

6.2.6 Strain Energy and Diastolic Suction

In general terms, strain energy can be thought of as energy stored in a stressed body

that can be recovered as work upon unloading. Compared to the control cycle, the greater SE_{full} (strain energy for the entire septum) which was achieved during PA constriction (see Figure 5.24) is consistent with deformation of a stiffer structure with accordingly greater developed stresses. Table 5.2 suggests that most of the strain energy during PA constriction is stored in the ends of the mesh (which is expected because of the large bending moments at the ends), whereas during control, the strain energy is almost evenly distributed along the length of the mesh (evidenced by SE_{60} having approximately 60% of the strain energy contained in the entire mesh).

The fact that SE_{full} seemed to reach a peak during PA constriction almost simultaneously with Max TSP_{neg} may have implications for LV filling, specifically for so-called "diastolic suction." It has long been appreciated that the LV has the capacity to suck blood into itself in the absence of left atrial filling pressure.[20,73,127] Numerous mechanisms for this suction have been suggested, most of which have pointed to potential energy stored during the process of ventricular contraction which is then released in diastole.[79,80,115,120,122,157] Recently in our lab, wave-intensity analysis has indicated the development of a backward expansion wave (a portion of which exists before mitral valve opening) which may also help to suck blood into the LV. The strain energy which developed in the septum during PA constriction, specifically at Max TSP_{neg}, may be but another mechanism for diastolic suction (it has been thought to play a role in disease states which have similar hemodynamics to that of PA constriction in which filling is impeded). In Figure 5.25, SE_{full} during control declined rapidly from ES to a baseline level in all dogs

before the LV began to fill (as indicated by CSA_{LV}). In contrast, during PA constriction (see Figure 5.26), in Dogs 2, 4, 5, and 6, SE_{full} declined from a peak level at Max TSP_{neg} (where the septum was loaded maximally) near where the LV began to fill. Because the stresses during PA constriction were predominantly circumferential and compressive, consistent with the idea of a restoring force (in contrast, the circumferential stresses which contributed to the high SE_{full} values immediately after ES during control were all tensile), it is conceivable that as the negative TSP was reduced, energy was released which might have helped the LV to fill.

6.2.7 Reverse FE Analysis

As presented in this dissertation, the FE method has been run in a reverse manner. By matching satisfactorily the measured "deformations" of the septum (as defined by the position of the septal mid-wall line), and magnitudes of pressure loading, there can be only a few reasonable combinations of initial geometry and material properties which would provide the same end result. This reverse approach is not new. Nikravesh[106] in 1976, Ghista et al[44] in 1980, and recently, Pao and Ritman[112] used the FE method not for stress analysis, but for constitutive modelling, the rationale of their analyses being that the FE solution will converge to the real solution if the proper loading conditions, boundary conditions, deformations, and constitutive relations are employed and equilibrium is enforced.[164] Outside of some practical considerations (e.g., constitutive relations must be amenable to iteration; predicted material properties must be validated using directly

measured values),[164] these investigators were mainly concerned with the boundary conditions (given that the loading conditions and deformations were all known), as their goal was to determine the appropriate constitutive relation. In this case, not only were the boundary conditions a concern (an attempt was made to minimize the end-effects – the 4 columns of elements on either side of each mesh were not shown) but, perhaps more importantly, the constitutive relation that was employed. It is for this reason that emphasis is placed on the difference in structural behaviour of the septum under different loading conditions rather than attempting to specify the exact magnitudes of stresses under these conditions.

6.2.8 Neo-Hookean Stress-Strain Relation

Many attempts have been made to describe an appropriate constitutive relation for the passive myocardium.[61-63,66,67,107] As a first approximation to the material properties of the septum, however, a neo-Hookean (i.e., linear stress-strain) strain-energy function was used, an approximation that requires justification. Over the normal working range of rat[134] and cat[30] trabeculae, SL varies between 1.55 μm and 2.40 μm. Rodriguez et al[125] and Guccione et al[53] have shown that SL varies between 1.70 μm and 2.40 μm in the intact, normal canine LV. Slack length of the sarcomeres (SL_0) has been shown to be approximately 1.85 μm.[149] Between SL of 1.60 μm (15% negative strain) and 2.20 μm (20% positive strain), the force-SL relation is practically linear, i.e., the stiffness is nearly constant.[9,30,59,134] Below 1.60 μm and above 2.20 μm the stiffness increases steeply. Thus, the material properties of the

septum have been approximated by using a neo-Hookean strain-energy function over this range. Further, Rodriguez et al[125] and Guccione et al[53] showed that SL = 2.20 μm occurred at an LV end-diastolic pressure (LVEDP) of approximately 15 mm Hg. Because LVEDP never exceeded 12 mm Hg under our control loading conditions, it is assumed that SL did not exceed 2.20 μm. For the PA-constriction loading conditions in Figures 5.14 through 5.19, the maximum circumferential compressive strain achieved at the middle of the RV-septal surface was just greater than -15%. The maximum circumferential tensile strain achieved at the middle of the LV-septal surface was approximately 10%. Rodriguez et al[126] have shown that the unloaded (but residually stressed) SL in the LV of the rat varied between a mean of 1.91 μm at the epicardium to a mean of 1.78 μm at the endocardium. It is assumed that the same distribution occurs in the canine septum. Because an unloaded, but residually stressed mesh was used to model the septum before loading at every point in diastole, the calculated values of strain can be related to SL_0. Most of the strain values calculated for PA constriction fall within the relatively linear region of the force-SL relation (or just outside, in the case of the negative strain achieved in the middle of the septum during inversion). It therefore seems reasonable to assume that the material relation employed in the model holds both for analysis of the control condition and for PA constriction. However, although the stress and strain levels are in a range over which the assumption of constant stiffness is a reasonable *first approximation*, it is emphasized that the numerical values obtained are not the most important element, but rather understanding the structural principles under which the septum operates. It is reasonable to expect strain

values corresponding to SL below 1.60 μm or above 2.20 μm, particularly near the ends of the mesh where the substantial bending moments which are applied have their greatest effect. If this occurs, the model would likely *underestimate* peak compressive and tensile stresses, respectively, as the slope of the F-SL relation increases (i.e., stiffness increases) markedly in these regions.

6.2.9 Principal Stresses

Although not commonly adopted in analyses of the heart, principal stresses have been used to describe the mechanics of other biological structures such as bone,[152] ligament,[90] and cartilage.[89] It is recognized that the principal stresses indicated by the model cannot be interpreted satisfactorily without accounting for fibre orientation, but, in general, remain an excellent mechanism for showing how load is transferred through the structure.

6.2.10 Assessment of Septal Geometry

Geometric parameters (thickness, radius of curvature, and insertion-point length) of the interventricular septum were derived from a septal mid-wall line. Local myocardial deformation gradients, as determined by Rodriguez et al[125] and Guccione et al,[53] cannot be obtained using echocardiography. This limitation of echocardiography is particularly relevant in the PA-constriction loading condition where the model suggests substantial circumferential compression and where steep transmural deformation gradients seem to occur. Measurement of septal segment length, as performed previously by Dong et al[34]

using sonomicrometry, might enable better determination of such gradients.

6.2.11 Residual Stress

Using relatively simple models for the calculation of stress, investigators have often assumed that wall stress is zero when LVP is zero. However, it has been demonstrated that the unloaded in-situ LV is not stress-free; Omens and Fung[110] showed that when a cross-sectional ring of a freshly excised, potassium-arrested rat LV is transected radially, it springs open, forming an arc. The 'residual' strain values obtained were consistent with bending moments having maintained the LV in its original, annular configuration. Using the strain data of Omens and Fung, Guccione et al[52] adapted an anisotropic model of the unloaded canine LV and calculated the approximate distribution of circumferential, longitudinal, and radial residual stress components across the LV wall. The magnitudes of radial residual stresses were negligible, but the circumferential and longitudinal stresses showed increasingly compressive values toward the LV-septal surface and increasingly tensile values toward the RV-septal surface. Because the model described in this dissertation is 2-D, incorporation of the circumferential residual stress distribution seemed most important. Although it could be argued that residual stress (the circumferential distribution ranges between +3 and -3 mm Hg[52]) does not significantly contribute to the structural behaviour patterns for large loading steps (i.e., during PA constriction where the compression is substantial or when TSP is high during control), it is a necessary component for analysis of the septum where the applied loads are of the same order of magnitude as the residual

stresses. This is particularly evident in Figures 5.17 and 5.19 which show the control circumferential stress gradient to be essentially the same as the residual stress distribution (it should be noted that compressive stresses developed during control in the absence of compressive strains – this occurred because of the fact that the residual stress distribution was incorporated as an external "initial conditions" file prior to loading of the mesh; an external residual strain distribution could not be incorporated using ABAQUS). Although the exact mechanism underlying the development of such stresses is not yet known, some investigators have speculated that restricted growth of myocytes which occurs in tissue, leads to interactions creating residual stresses and strains which are borne by the intercellular structures.[91]

6.3 Conclusions

The results of the model allowed the following conclusions (regarding the structural behaviour of the septum) to be made:

(i) Compared to control, substantial circumferential compressive stresses develop in the septum during PA constriction.

(ii) Compared to control, the septum exhibits arch-like behaviour during PA constriction. Specifically, the septum bears the PA-constriction loading by distributing the net "downward" thrust of the load laterally, through a pattern of compressive stress towards the RV insertions.

(iii) Compared to control, substantial bending moments develop in the septum,

which vary along its length, during PA constriction.

(iv) Compared to control, the stiffness of the septum increases during PA constriction.

(v) Compared to control, greater strain energy develops in the septum during PA constriction.

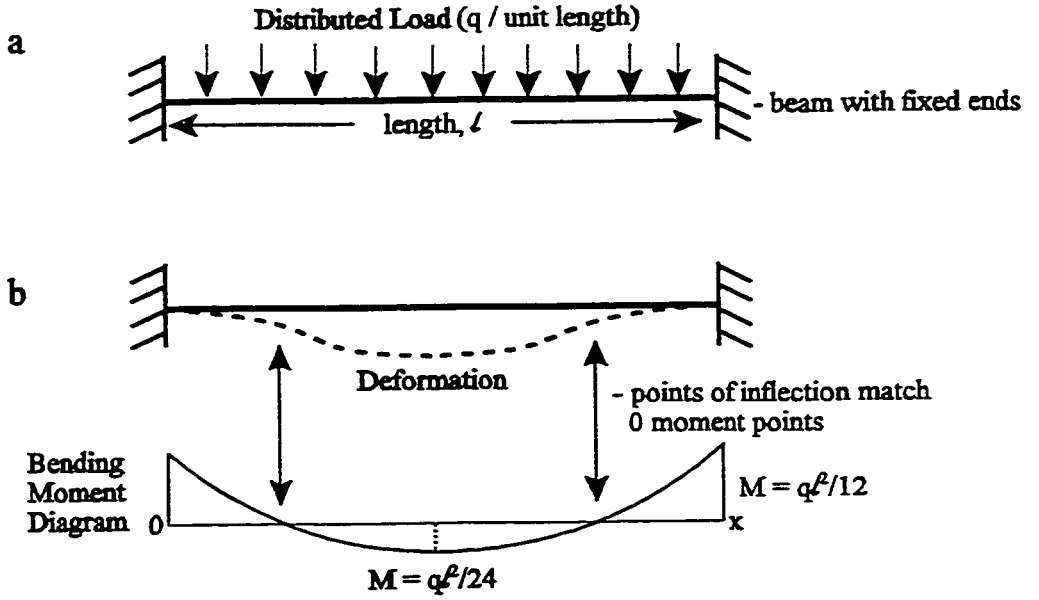

Figure 6.1 (a) A beam with fixed ends is subject to uniformly distributed loading, with (b) resulting deformation and bending moment diagram. See text for further details.

CHAPTER 7

FUTURE DIRECTIONS

7.1 Circumferential Compressive Stress and Septal Ischemia

The substantial circumferential compressive stresses predicted by the model during PA constriction may pertain to a number of clinical situations. In several diseases in which the TSP is decreased or reversed (e.g., mitral stenosis, primary pulmonary hypertension, and pulmonary thromboembolic disease) and septal flattening and inversion is observed, there may be chest pain which is indistinguishable from that associated with myocardial ischemia. This has usually been attributed to RV ischemia, despite the absence of coronary arterial stenoses. In addition, in the presence of left-bundle branch block (LBBB) which also alters septal motion, thallium perfusion studies are often "falsely positive," suggesting relative septal ischemia even though the coronary arteries are shown to be normal.[12] The demonstration of substantial circumferential compressive stresses in the septum leads to a hypothesis which must be tested rigorously: that such stresses could increase resistance to diastolic blood flow to a degree sufficient to cause ischemia. Perfusion studies utilizing either Doppler Flowire or contrast echocardiography techniques will be required in order to test this hypothesis.

7.2 Effects of the Pericardium and Extension of the Model to the LV Free Wall

The pericardium was closed during the experiments, which has important implications with respect to the RV. Because the RV free wall is so thin and distensible, approximately 80% of RV intracavitary pressure is really due to the pericardium.[56,155] For example, an intracavitary pressure of 5 mm Hg would correspond to a transmural pressure

of 1 mm Hg and a normal RV volume. However, in the absence of the pericardium, the same intracavitary pressure of 5 mm Hg (which would then equal the transmural pressure) would distend the RV considerably. Thus, these results cannot be compared directly to those from experiments in which the pericardium was left open. The fact that RV distension was limited by the pericardium must have affected the angle and the magnitude of the RV force vector at the insertion points. The presence of the pericardium probably also affected the end-bending moments required for the PA constriction loading condition. In order for equilibrium to be established, the bending moments which were required at the RV insertion points must have been accompanied by balancing, oppositely directed end-bending moments. Those end-bending moments must have been borne by the LV free wall, as modulated by local pericardial pressure. In many echocardiograms in which the LV free wall was observed, the LV free wall was flattened, consistent with there being oppositely acting end-bending moments to those on the septum. Furthermore, flattening of the LV free wall may have occurred since LVTMP (which is the major determinant of distension of the free wall) was 0 mm Hg or slightly negative during PA constriction (see Figure 5.6). Further investigation in this area will require extension of the current model to include the LV free wall. This might also have the potential of providing a more satisfactory analysis of control loading conditions when TSP is high.

7.3 Fibre Architecture and Nonlinear Constitutive Relations

A model based on thin-walled theory would not have revealed the structural

differences between the control and PA-constriction loading conditions detailed in this paper. The desire to develop a model sufficient to detect such differences and characterize possible compressive stresses and end-bending moments, but not be overwhelmingly complex, resulted in the use of a 2-D FE model with plane stress elements. Perhaps the most significant limitation of such a model is that fibres, which render the myocardium anisotropic, cannot be incorporated. To attempt to account for the effect of myocardial fibres, one could vary the stiffness in different directions across the mesh (e.g., incorporation of a parabolic variation in circumferential elastic modulus[97,145]). Granzier and Irving[49] have shown that a substantial fraction of the passive stiffness derives from the endosarcomeric protein, titin, which runs coaxially with the fibres. Varying the stiffness, however, would require more material parameters than for the isotropic neo-Hookean hyperelasticity used here, making the problem more difficult to solve numerically. In future studies, not only should attempts be made to account for fibre orientation, but also a nonlinear stress-strain relation should be employed. This would allow for a more realistic calculation of stresses, particularly near the RV insertion points, where the strains are larger than those which occur along the middle of the RV-septal surface during inversion. It is conceivable that these larger strains (at the ends of the mesh), which fall *outside* the relatively linear range of the F-SL relation, i.e., where stiffness increases steeply, may be contributing to the increased stiffness observed during PA constriction – incorporation of a nonlinear constitutive law would help determine more clearly the contribution of coronary venous congestion under these severe conditions. Finally, the assumption of myocardial

incompressibility in the model may be incorrect. Recently, Yin et al[166] have shown, using a digital subtraction angiographic method, that perfused myocardium is in fact compressible. The authors suggested accounting for compressibility by using mixture theory or other similar approaches.

7.4 Long-Axis Inversion of the Septum

The present model has utilized plane stress elements to model short-axis septal flattening and inversion, thus ignoring any stress development in the third dimension. The concern arises that long-axis curvature changes may affect the results calculated using such a model. To attempt to investigate this effect, a mesh was constructed using plane strain elements (a 2-D plane strain model implies that there is no strain in the long-axis direction). The close agreement between the two models during both control and PA constriction (see Figure 5.31) suggests that long-axis stresses do not have a significant effect on the structural behaviour which develops in the short axis (particularly during PA constriction where substantial longitudinal compression develops). A potential future direction will involve investigation of the effect of long-axis septal inversion on that which occurs in the short axis, something which the 2-D plane strain model cannot address.

REFERENCES

1. *The Heart: Arteries and Veins*. New York, McGraw-Hill Inc, 1994.

2. *Gray's Anatomy. The Anatomical Basis of Medicine and Surgery*. New York, Churchill Livingstone, 1995.

3. Agata Y, Hiraishi S, Misawa H, Takanashi S, Yashiro K: Two-dimensional echocardiographic determinants of interventricular septal configuration in right and left ventricular overload. *Am Heart J* 1985;110:819-825.

4. Akima H: A method of bivariate interpolation and smooth surface fitting based on local procedures. *Comm ACM* 1974;17:18-31.

5. Alpert NR: *Cardiac Hypertrophy*. New York, Academic Press, 1971.

6. Anderson RH, AE Beeker: *Cardiac Anatomy: An Integrated Text and Color Atlas*. London, Gower Medical Publisher, 1980.

7. Argyris JH: *Energy Theorems and Structural Analysis*. London, Butterworth, 1960.

8. Armour JA, Randall WC: Structural basis for cardiac function. *Am J Physiol* 1970;218:1517-1523.

9. Backx PH: The force-sarcomere length relation in cardiac myocytes. PhD Thesis, University of Calgary, 1989.

10. Badke FR: Left ventricular dimensions and function during right ventricular pressure overload. *Am J Physiol Heart Circ Physiol* 1982;242:H611-H618.

11. Bemis CE, Serur JR, Borkenhagen D, Sonnenblick EH, Urschel CW: Influence of right ventricular filling pressure on left ventricular pressure and dimension. *Circ Res* 1974;34:498-504.

12. Beppu S, Matsuda H, Shishido T, Miyatake K: Functional myocardial perfusion abnormality induced by left ventricular asynchronous contraction: experimental study using myocardial contrast echocardiography. *J Am Coll Cardiol* 1997;29:1632-1638.

13. Berne RM, MN Levy: *Cardiovascular Physiology*. Chicago, Mosby Year Book, 1992.

14. Berne RM, Rubio R: Coronary circulation, in Berne RM, Sperelakis N, Geiger SR (eds): *Handbook of Physiology Section 2: The Cardiovascular System*. Bethesda, American Physiological Society, 1979, pp 873-952.

15. Beyar R, Dong S-J, Smith ER, Belenkie I, Tyberg JV: Ventricular interaction and septal deformation: A model compared with experimental data. *Am J Physiol Heart Circ Physiol* 1993;265:H2044-H2056.

16. Beyar R, Sideman S: Left ventricular mechanics related to the local distribution of oxygen demand throughout the wall. *Circ Res* 1986;58:664-677.

17. Bogen DK, Needleman A, McMahon TA: An analysis of myocardial infarction: the effect of regional changes in contractility. *Circ Res* 1984;55:805-815.

18. Bogen DK, Rabinowitz SA, Needleman A, McMahon TA, Abelmann WH: An analysis of the mechanical disadvantage of myocardial infarction in the canine left ventricle. *Circ Res* 1980;47:728-741.

19. Brebbia CA, JJ Connor: *Fundamentals of Finite Element Techniques for Structural Engineers*. London, Butterworth & Co. Ltd., 1973.

20. Brecher GA: Experimental evidence of ventricular diastolic suction. *Circ Res* 1956;4:513-518.

21. Brinker JA, Weiss JL, Lappe DL, Rabson JL, Summer WR, Permutt S, Weisfeldt ML:

Leftward septal displacement during right ventricular loading in man. *Circulation* 1980;61:626-633.

22. Burns JW, Covell JW, Myers R, Ross J, Jr. Comparison of directly measured left ventricular wall stress and stress calculated from geometric reference figures. *Circ Res* 1971;28:611-621.

23. Burton AC: The importance of the shape and size of the heart. *Am Heart J* 1957;54:801-810.

24. Chajes A: *Structural Analysis.* Englewood Cliffs, Prentice Hall, 1990.

25. Chandran KB: *Cardiovascular Biomechanics.* New York, New York University Press, 1992.

26. Cook RD: *Concepts and Applications of Finite Element Analysis.* New York, John Wiley & Sons, 1974.

27. Costa KD, Hunter PJ, Rogers JM, Guccione JM, Waldman LK, McCulloch AD: A three-dimensional finite element method for large elastic deformations of ventricular myocardium. I. Cylindrical and spherical polar coordinates. *ASME J Biomech Eng*

1996;118:452-463.

28. Costa KD, Hunter PJ, Wayne JS, Waldman LK, Guccione JM, McCulloch AD: A three-dimensional finite element method for large elastic deformations of ventricular myocardium. II. Prolate spheroidal coordinates. *ASME J Biomech Eng* 1996;118:464-472.

29. Costa KD, May-Newman K, Farr D, O'Dell WG, McCulloch AD, Omens JH: Three-dimensional residual strain in midanterior canine left ventricle. *Am J Physiol Heart Circ Physiol* 1997;273:H1968-H1976.

30. de Tombe PP, ter Keurs HEDJ: Sarcomere dynamics in cat cardiac trabeculae. *Circ Res* 1991;68:588-596.

31. Demer LL, Yin FCP: Passive biaxial mechanical properties of isolated canine myocardium. *J Physiol Lond* 1983;339:615-630.

32. Diamond MA, Dillon JC, Haine CL, Chang S, Feigenbaum H: Echocardiographic features of atrial septal defect. *Circulation* 1971;43:129.

33. Dong S-J, Beyar R, Zhou Z-N, Fick GH, Smith ER, Tyberg JV: Determinants of

midwall circumferential segmental length of the canine ventricular septum at end diastole. *Am J Physiol Heart Circ Physiol* 1993;265:H2057-H2065.

34. Dong S-J, Smith ER, Tyberg JV: Changes in the radius of curvature of the ventricular septum at end diastole during pulmonary arterial and aortic constrictions in the dog. *Circulation* 1992;86:1280-1290.

35. Elzinga G, Van Grondelle R, Westerhof N, VandenBos GC: Ventricular interference. *Am J Physiol* 1974;226:941-947.

36. Elzinga G, Westerhof N: How to quantify pump function of the heart. *Circ Res* 1979;44:303.

37. Falsetti HL, Mates RE, Grant C, Bunnell IL: Left ventricular wall stress calculated from one-plane cineangiography. *Circ Res* 1970;26:71-83.

38. Feigl EO, Simon GA, Fry DL: Auxotonic and isometric cardiac force transducers. *J Appl Physiol* 1967;23:597-600.

39. Feit TS: Diastolic pressure-volume relations and distribution of pressure and fiber extension across the wall of a model left ventricle. *J Biophys* 1979;28:143-166

40. Feneley M, Gavaghan T: Paradoxical and pseudoparadoxical interventricular septal motion in patients with right ventricular volume overload. *Circulation* 1986;74:230-238.

41. Feneley MP, Olsen CO, Glower DD, Rankin JS: Effect of acutely increased right ventricular afterload on work output from the left ventricle in conscious dogs: Systolic ventricular interaction. *Circ Res* 1989;65:135-145.

42. Fox CC, Hutchins GM: The architecture of the human ventricular myocardium. *Johns Hopkins Med J* 1971;130:289-299.

43. Fung YC: *Biodynamics: Circulation.* New York, Springer-Verlag, 1984.

44. Ghista DN, Ray G, Sandler H: Cardiac assessment mechanics: 1. Left ventricular mechanomyocardiography, a new approach to the detection of diseased myocardial elements and states. *Med Biol Eng Comput* 1980;18:271-280.

45. Ghista DN, Sandler H: An analytic elastic-viscoelastic model for the shape and the forces in the left ventricle. *J Biomech* 1969;2:35-47.

46. Goor DA, Edwards JE, Lillehei R: The development of the interventricular septum of

the human heart: correlative morphogenetic study. *Chest* 1970;58:453-457.

47. Gould P, Ghista D, Brombolich L: In vivo stresses in the human left ventricular wall: analysis accounting for the irregular 3-dimensional geometry and comparison with idealized geometry analyses. *J Biomech* 1972;5:521-539.

48. Grant JCB, JB Basmajian: *Grant's Method of Anatomy*. Baltimore, The Williams & Wilkins Company, 1965.

49. Granzier H, Irving TC: Passive tension in cardiac muscle: contribution of collagen, titin, microtubules, and intermediate filaments. *Biophys J* 1995;68:1027-1044.

50. Guccione JM, Costa KD, McCulloch AD: Finite element stress analysis of left ventricular mechanics in the beating dog heart. *J Biomech* 1995;28:1167-1177.

51. Guccione JM, McCulloch AD: Finite element modelling of ventricular mechanics, in Glass L, Hunter P, McCulloch AD (eds): *Theory of Heart. Biomechanics, Biophysics, and Nonlinear Dynamics of Cardiac Function.* New York, Springer-Verlag, 1991, pp 121-144.

52. Guccione JM, McCulloch AD, Waldman LK: Passive material properties of intact

ventricular myocardium determined from a cylindrical model. *ASME J Biomech Eng* 1991;113:42-55.

53. Guccione JM, O'Dell WG, McCulloch AD, Hunter WC: Anterior and posterior left ventricular sarcomere lengths behave similarly during ejection. *Am J Physiol Heart Circ Physiol* 1997;272:H469-H477.

54. Guzman PA, Maughan WL, Yin FCP, Eaton LW, Brinker JA, Weisfeldt ML, Weiss JL: Transseptal pressure gradient with leftward septal displacement during the Mueller manoeuvre in man. *Br Heart J* 1981;46:657-662.

55. Halperin HR, Tsitlik JE, Gelfand M, Downs J, Yin FC: Servo-controlled indenter for determining the transverse stiffness of ventricular muscle. *IEEE Trans Biomed Eng* 1991;38:602-607.

56. Hamilton DR, Dani RS, Semlacher RA, Smith ER, Kieser TM, Tyberg JV: Right atrial and right ventricular transmural pressures in dogs and humans. Effects of the pericardium. *Circulation* 1994;90:2492-2500.

57. Heethaar RM, Robb RA, Pao YC, Ritman EL: Three-dimensional stress and strain in the intact heart, in Martin JI (ed): *Proceedings of the San Diego Biomedical*

Symposium. New York, Academic Press, 1976, pp 337-342.

58. Hefner LL, Sheffield LT, Cobbs GC, Klip W: Relation between mural force and pressure in the left ventricle of the dog. *Circ Res* 1962;11:654-663.

59. Helmes M, Trombitas K, Granzier H: Titin develops restoring force in rat cardiac myocytes. *Circ Res* 1996;79:619-626.

60. Henderson Y, Prince AL: The relative systolic discharges of the right and left ventricles and their bearing on pulmonary congestion and depletion. *Heart* 1914;5:217-226.

61. Horowitz A, Lanir Y, Yin FCP, Perl M, Sheinman I, Strumpf RK: Structural three-dimensional constitutive law for the passive myocardium. *ASME J Biomech Eng* 1988;110:200-207.

62. Horowitz A, Sheinman I, Lanir Y: Non-linear incompressible finite element for simulating loading of cardiac tissue. Part II: Three-dimensional formulation for thick ventricular wall segments. *ASME J Biomech Eng* 1988;110:62-68.

63. Horowitz A, Sheinman I, Lanir Y, Perl M, Sideman S: Non-linear incompressible finite element for simulating loading of cardiac tissue. Part I: Two-dimensional

formulation for thin myocardial strips. *ASME J Biomech Eng* 1988;110:57-61.

64. Huisman RM, Elzinga G, Westerhof N, Sipkema P: Measurement of left ventricular wall stress. *Cardiovasc Res* 1980;14:142-153.

65. Huisman RM, Sipkema P, Westerhof N, Elzinga G: Wall stress measurements in non-beating canine hearts: application of a method tested in rubber models. *Cardiovasc Res* 1979;13:642-651.

66. Humphrey JD, Strumpf RK, Yin FC: Determination of a constitutive relation for passive myocardium: II. Parameter estimation. *ASME J Biomech Eng* 1990;112:340-346.

67. Humphrey JD, Strumpf RK, Yin FC: Determination of a constitutive relation for passive myocardium: I. A new functional form. *ASME J Biomech Eng* 1990;112:333-339.

68. Iliceto S, Dambrosie M, Sorino M, D'Ambrosio G, Amico A, Fiore T, Rizzon P: Effects of acute intrathoracic pressure changes on left ventricular geometry and filling. *Am Heart J* 1988;116:455-465.

69. James TN, Burch GE: Blood supply of the human interventricular septum. *Circulation* 1958;17:391-396.

70. Jan KM: Distribution of myocardial stress and its influence on coronary blood flow. *J Biomech* 1985;18:81-820.

71. Janz RF, Grimm AF: Finite-element model for the mechanical behaviour of the left ventricle. *Circ Res* 1972;30:244-251.

72. Janz RF, Kubert BR, Moriarity TF: Deformation of the diastolic left ventricle. II. Nonlinear geometric effects. *J Biomech* 1974;7:509-516.

73. Katz LN: The role played by the ventricular relaxation process in filling the ventricle. *Am J Physiol* 1930;95:542-553.

74. Kaul S, Jayaweera AR: Coronary and myocardial blood volumes. Noninvasive tools to assess the coronary microcirculation? *Circulation* 1997;96:719-724.

75. Kent RS, Carew TE, LeWinter MM, Covell JW: Comparison of left ventricular free wall and septal diastolic compliance in the dog. *Am J Physiol Heart Circ Physiol* 1978;234:H392-H398.

76. Kerber RE, Dippel WF, Abboud FM: Abnormal motion of the interventricular septum in right ventricular volume overload. *Circulation* 1973;48:86-96.

77. King ME, Braun H, Goldblatt A, Liberthson R, Weyman AE: Interventricular septal configuration as a predictor of right ventricular systolic hypertension in children: a cross-sectional echocardiographic study. *Circulation* 1983;68:68-75.

78. Kingma I, Tyberg JV, Smith ER: Effects of diastolic transseptal pressure gradient on ventricular septal position and motion. *Circulation* 1983;68:1304-1314.

79. Kroeker CAG, Tyberg JV, Beyar R: The effects of load manipulations, heart rate, and contractility on apical rotation: an experimental study in anaesthetized dogs. *Circulation* 1995;92:130-141.

80. Kroeker CAG, Tyberg JV, Beyar R: The effects of ischemia on left ventricular apex-rotation: an experimental study in anaesthetized dogs. *Circulation* 1995;92:3539-3548.

81. Lame G: *Lecons sur la theorie mathematique de l'elasticite des corps solides.* Paris, Gauthier-Villars, 1866.

82. LaPlace PS: *Theorie de l'action capillarie en traité de mechanique celeste, suppl au livre X.* Paris, Coarcien, 1806.

83. Laurenceau JL, Dumesnil JG: Right and left ventricular dimensions as determinants of ventricular septal motion. *Chest* 1976;69:388-393.

84. Lew WYW: Influence of ischemic zone size on nonischemic area function in the canine left ventricle. *Am J Physiol Heart Circ Physiol* 1987;252:H990-H997.

85. Lewartowski B, Sedek G, Okolska A: Direct measurement of tension within the left ventricular wall of the dog heart. *Cardiovasc Res* 1972;6:28-35.

86. Lima JAC, Guzman PA, Yin FCP, Brawley RK, Humphrey L, Traill TA, Lima SD, Marino P, Weisfeldt ML, Weiss JL: Septal geometry in the unloaded living human heart. *Circulation* 1986;74:463-468.

87. Lindner JR, Skyba DM, Goodman NC, Jayaweera AR, Kaul S: Changes in myocardial blood volume with graded coronary stenosis. *Am J Physiol Heart Circ Physiol* 1997;272:H567-H575.

88. Louie EK, Rich S, Brundage BH: Doppler echocardiographic assessment of impaired

left ventricular filling in patients with right ventricular pressure overload due to primary pulmonary hypertension. *J Am Coll Cardiol* 1986;8:1298-1306.

89. MacConaill MA: The movement of bones and joints - 4. The mechanical structure of articulating cartilage. *J Bone Jt Surg* 1951;33:251-257.

90. Matyas JR, Anton MG, Shrive NG, Frank CB: Stress governs tissue phenotype at the femoral insertion of the rabbit MCL. *J Biomech* 1995;28:147-157.

91. McCulloch AD, Omens JH: Factors affecting the regional mechanics of the diastolic heart, in Glass L, Hunter P, McCulloch AD (eds): *Theory of Heart. Biomechanics, Biophysics, and Nonlinear Dynamics of Cardiac Function.* New York, Springer-Verlag, 1991, pp 87-119.

92. McGregor M: Pulsus paradoxus. *N Engl J Med* 1979;301:480-482.

93. McHale PA, Greenfield JC: Evaluation of several geometric models for estimation of left ventricular circumferential wall stress. *Circ Res* 1973;33:303-312.

94. McMahon SM, Permutt S, Proctor DF: A model to evaluate pleural surface pressure measuring devices. *J Appl Physiol* 1969;27:886-891.

95. Meyer RA, Schwartz DC, Benzing G, III, Kaplan S: Ventricular septum in right ventricular volume overload: an echocardiographic study. *Am J Cardiol* 1972;30:349-353.

96. Mirsky I: Left ventricular stresses in the intact human heart. *Biophys J* 1969;9:189-208.

97. Mirsky I: Ventricular and arterial wall stresses based on large deformation analyses. *Biophys J* 1970;13:1141-1159.

98. Mirsky I: Effects of anisotropy and nonhomogeneity on left ventricular stresses in the intact human heart. *Bull Math Biophys* 1973;32:197-213.

99. Mirsky I: Review of various theories for the evaluation of left ventricular wall stresses, in Mirsky I, Ghista DN, Sandler H (eds): *Cardiac Mechanics: Physiological, Clinical and Mathematical Considerations*. New York, John Wiley and Sons, Inc. 1974, pp 381-409.

100. Mirsky I: Assessment of passive elastic stiffness of cardiac muscle: Mathematical concepts, physiologic and clinical considerations, directions of future research. *Prog Cardiovasc Dis* 1976;18:277-308.

101. Mirsky I: Elastic properties of the myocardium: a quantitative approach with physiological and clinical applications, in Berne RM (ed): *Handbook of Physiology, Section 2, The Cardiovascular System*. Washington, D.C. American Physiological Society, 1979, pp 497-531.

102. Moir TW, Driscol TE, Eckstein JW: Thebesian drainage in the left heart of the dog. *Circ Res* 1964;14:245-249.

103. Molaug M, Geiran O, Stokland O, Thorvaldson J, Ilebekk A: Dynamics of the interventricular septum and free ventricular walls during blood volume expansion and selective right ventricular volume loading in dogs. *Acta Physiol Scand* 1982;116:245-256.

104. Molaug M, Stokland O, Ilebekk A, Lekven J, Kiil F: Myocardial function of the interventricular septum. Effects of right and left ventricular pressure loading before and after pericardiotomy in dogs. *Circ Res* 1981;49:52-61.

105. Moriarity TF: The law of LaPlace, its limitations as a relation for diastolic pressure, volume, or wall stress of the left ventricle. *Circ Res* 1980;46:321-331.

106. Nikravesh E: Optimization in finite-element analysis with special reference to

three-dimensional left ventricular dynamics. PhD Thesis, Tulane University, 1976.

107. Novak VP, Yin FC, Humphrey JD: Regional mechanical properties of passive myocardium. *J Biomech* 1994;27:403-412.

108. Olsen CO, Tyson GS, Maier GW, Spratt JA, Davis JW, Rankin JS: Dynamic ventricular interaction in the conscious dog. *Circ Res* 1983;52:85-104.

109. Olsson RA, Bunger R, Spaan JAE: Coronary circulation, in Fozzard HA, Haber E, Jennings RB, Katz AM, Morgan HE (eds): *The Heart and Cardiovascular System. Scientific Foundations.* New York, Raven Press, 1992, pp 1393-1425.

110. Omens JH, Fung Y-C: Residual strain in rat left ventricle. *Circ Res* 1990;66:37-45.

111. Panda SC, Natarajan R: Finite-element method of stress analysis in the human left ventricular layered wall structure. *Med Biomed Eng Comput* 1977;15:67-71.

112. Pao YC, Ritman EL: Comparative characterization of the infarcted and reperfused ventricular wall muscles by finite element analysis and a myocardial muscle: blood composite model. *Comp Biomed Res* 1998;31:18-31.

113. Pao YC, Ritman EL, Wood EH: Finite-element analysis of left ventricular myocardial stresses. *J Biomech* 1974;7:469-477.

114. Pao YC, Robb RA, Ritman EL: Plane-strain finite-element analysis of reconstructed diastolic left ventricular cross section. *Ann Biomed Eng* 1976;4:232-249.

115. Parsons C, Porter KR: Muscle relaxation: evidence for intrafibrillar restoring force in vertebrate striated muscle. *Science* 1966;153:426-427.

116. Pearlman AS, Clark CE, Henry WL, Morganroth J, Itscoitz SB, Epstein SE: Determinants of ventricular septal motion: influence of relative right and left ventricular size. *Circulation* 1976;54:83-91.

117. Pearlman ES, Weber KT, Janicki JS, Pietra GG, Fishman AP: Muscle fiber orientation and connective tissue content in the hypertrophied human heart. *Lab Invest* 1982;46:158-164.

118. Pina JAE, Correia M, Goyri O'Neill J: Morphological study on the thebesian veins of the right cavities of the heart in the dog. *Acta Anat* 1975;92:310-320.

119. Pinto JG, Fung YC: Mechanical properties of the heart muscle in the passive state. *J*

Biomech 1973;6:597-616.

120. Pollack GH, Huntsman LL, Verdugo P: Cardiac muscle models: an overextension of series elasticity. *Circ Res* 1972;31:569-579.

121. Popp RL, Wolfe SB, Hirata T, Feigenbaum H: Estimation of right and left ventricular size by ultrasound: a study of the echoes from the interventricular septum. *Am J Cardiol* 1969;24:523-530.

122. Rademakers FE, Buchalter MB, Rogers WJ, Zerhouni EA, Weisfeldt ML, Weiss JL, Shapiro EP: Dissociation between left ventricular untwisting and filling. Accentuation by catecholamines. *Circulation* 1992;85:1572-1581.

123. Resar JR, Judd RM, Halperin HR, Chacko VP, Weiss RG, Yin FCP: Direct evidence that coronary perfusion affects diastolic myocardial mechanical properties in canine heart. *Cardiovasc Res* 1993;27:403-410.

124. Robie NW, Newman WH: Effects of altered ventricular load on the Walton-Brodie strain gauge arch. *J Appl Physiol* 1974;36:20-27.

125. Rodriguez EK, Hunter WC, Royce MJ, Leppo MK, Douglas AS, Weisman HF: A

method to reconstruct myocardial sarcomere lengths and orientations at transmural sites in beating canine hearts. *Am J Physiol Heart Circ Physiol* 1992;263:H293-H306.

126. Rodriguez EK, Omens JH, Waldman LK, McCulloch AD: Effect of residual stress on transmural sarcomere length distributions in rat left ventricle. *Am J Physiol Heart Circ Physiol* 1993;264:H1048-H1056.

127. Rushmer RF, Crystal DK, Wagner C: The functional anatomy of ventricular contraction. *Circ Res* 1953;1:162.

128. Sagawa K, L Maughan, H Suga, K Sunagawa: *Cardiac Contraction and the Pressure-Volume Relationship*. New York, Oxford, Oxford University Press, 1988.

129. Sandler H, Dodge HT: Left ventricular tension and stress in man. *Circ Res* 1963;13:91-104.

130. Sandler H, Ghista DN: Mechanical and dynamical implications of dimensional measurements of the left ventricle. *Federation Proc* 1969;28:1344-1350.

131. Santamore WP, Lynch PR, Meyer G, Heckman J, Bove AA: Myocardial interaction

between the ventricles. *J Appl Physiol* 1976;41:362-368.

132. Sarnoff SJ, Braunwald E, Welch GHJ, Case RB, Stainsby WN, Macruz R: Hemodynamic determinants of oxygen consumption of the heart with special reference to the tension-time index. *Am J Physiol* 1958;192:148-156.

133. Sasayama S, Nakamura M, Takahashi M, Osakada G, Shimada T, Nishimura E, Kawai C: Influence of acute mechanical overload on dimension and dynamics of interventricular septal thickness in dogs. *Am J Cardiol* 1981;48:93-100.

134. Schouten VJ, Bucx JJ, de Tombe PP, ter Keurs HE: Sarcolemma, sarcoplasmic reticulum, and sarcomeres as limiting factors in force production in rat heart. *Circ Res* 1990;67:913-922.

135. Scott-Douglas NW, Traboulsi M, Smith ER, Tyberg JV: Experimental instrumentation and left ventricular pressure-strain relationship. *Am J Physiol Heart Circ Physiol* 1991;261:H1693-H1697.

136. Smiseth OA, Frais MA, Kingma I, Smith ER, Tyberg JV: Assessment of pericardial constraint in dogs. *Circulation* 1985;71:158-164.

137. Smiseth OA, Scott-Douglas NW, Thompson CR, Smith ER, Tyberg JV: Nonuniformity of pericardial surface pressure in dogs. *Circulation* 1987;75:1229-1236.

138. Smith ER, Tyberg JV: Mechanics of the ventricular septum, in ter Keurs HEDJ, Tyberg JV (eds): *Mechanics of the Circulation*. Dordrecht, Martinus Nijhoff Publishers, 1987, pp 171-188.

139. Sonnenblick EH: Force-velocity relations in mammalian heart muscle. *Am J Physiol* 1962;202:931-939.

140. Sonnenblick EH: Series elastic and contractile elements in heart muscle: changes in muscle length. *Am J Physiol* 1964;207:1330-1338.

141. Sonnenblick EH, Parmley WW, Urschel CW: The contractile state of the heart as expressed by force-velocity relations. *Am J Cardiol* 1969;23:488.

142. Stein PD, Marzilli M, Sabbah HN, Lee T: Systolic and diastolic pressure gradients within the left ventricular wall. *Am J Physiol Heart Circ Physiol* 1980;238:H625-H630.

143. Stool EW, Mullins CB, Leshin SJ, Mitchell JH: Dimensional changes of the left ventricle during acute pulmonary arterial hypertension in dogs. *Am J Cardiol* 1974;33:868-875.

144. Streeter DD: Gross morphology and fiber geometry of the heart, in Berne RM, Sperelakis N, Geiger SR (eds): *Handbook of Physiology, Section 2: The Cardiovascular System, Volume 1*. Bethesda, American Physiological Society, 1979, pp 61-112.

145. Streeter DD, Spotnitz HM, Patel DJ, Ross J, Jr., Sonnenblick EH: Fiber orientation in the canine left ventricle during diastole and systole. *Circ Res* 1969;24:339-347.

146. Streeter DD, Vaishnav RN, Patel DJ, Spotnitz HM, Ross J, Jr., Sonnenblick EH: Stress distribution in the canine left ventricle during diastole and systole. *Biophys J* 1970;10:345-363.

147. Streeter DD, Jr., Hanna WT: Engineering mechanics for successive states in canine left ventricular myocardium: I. Cavity and wall geometry. *Circ Res* 1973;33:639-655.

148. Tanaka H, Tei C, Nakao S, Tahara M, Sakurai S, Kashima T, Kanehisa T: Diastolic bulging of the interventricular septum toward the left ventricle. An

echocardiographic manifestation of negative interventricular pressure gradient between left and right ventricles during diastole. *Circulation* 1980;62:558-563.

149. ter Keurs HEDJ, Rijnsburger WH, van Heuningen R, MJ N: Tension development and sarcomere length in rat cardiac trabeculae evidence of length-dependent activation. *Circ Res* 1980;46:703-714.

150. Theroux P, Ross J, Jr., Franklin D, Covell JW, Bloor CW, Sasayama S: Regional myocardial function and dimensions early and late after myocardial infarction in the unanesthetized dog. *Circ Res* 1977;40:158-165.

151. Thompson CR, Kingma I, MacDonald RPR, Belenkie I, Tyberg JV, Smith ER: Transseptal pressure gradient and diastolic ventricular septal motion in patients with mitral stenosis. *Circulation* 1987;76:974-980.

152. Toridis TG: Stress analysis of the femur. *J Biomech* 1969;2:163-174

153. Torrent-Guasp F: *Anatomia Funcional del Corazon*. Madrid, Editorial Paz Montalvo, 1957.

154. Tozeren A: Static analysis of the left ventricle. *ASME J Biomech Eng* 1983;105:39-46.

155. Traboulsi M, Scott-Douglas NW, Smith ER, Tyberg JV: The right and left ventricular intracavitary and transmural pressure-strain relationships. *Am Heart J* 1992;123:1279-1287.

156. Turner MJ, Clough RW, Martin HC, Topp LJ: Stiffness and deflection analysis of complex structures. *J Aero Sci* 1956;23:805-823.

157. Tyberg JV, Keon WJ, Sonnenblick EH, Urschel CW: Mechanics of ventricular diastole. *Cardiovasc Res* 1970;4:423-428.

158. Visner MS, Arentzen CE, O'Conner MJ, Larson EV, Anderson RW: Alterations in left ventricular three-dimensional dynamic geometry and systolic function during acute right ventricular hypertension in the conscious dog. *Circulation* 1983;67:353-365.

159. Walker ML, Hawthorne EW, Sandler H: Methods for assessing performance for the intact hypertrophied heart, in Alpert NR (ed): *Cardiac Hypertrophy*. New York, Academic Press, 1971, pp 387-405.

160. Watanabe J, Levine MJ, Bellotto F, Johnson RG, Grossman W: Effects of coronary venous pressure on left ventricular diastolic distensibility. *Circ Res* 1981;49:829-842.

161. Wolfe KB: Anatomy of the septal artery in dogs' hearts. *Am J Surg* 1959;97:279-282.

162. Wong AYK, Rautaharju PM: Stress distribution within the left ventricular wall approximated as a thick ellipsoidal shell. *Am Heart J* 1968;75:649-662.

163. Woods RH: A few applications of a physical theorem to membranes in the human body in a state of tension. *J Anat Physiol* 1892;26:362-370.

164. Yin FCP: Brief reviews: Ventricular wall stress. *Circ Res* 1981;49:829-842.

165. Yin FCP: Applications of the finite-element method to ventricular mechanics. *CRC Crit Rev Biomed Eng* 1985;12:311-342.

166. Yin FCP, Chan CCH, Judd RM: Compressibility of perfused passive myocardium. *Am J Physiol Heart Circ Physiol* 1996;271:H1864-H1870.

167. Yin FCP, Strumpf RK, Chew PH, Zeger SL: Quantification of the mechanical properties of noncontracting canine myocardium under simultaneous biaxial loading. *J Biomech* 1987;20:577-589.

168. Young TH: An essay on the cohesion of fluids. *Phil Trans Roy Soc London, Ser B*

1805;95:66.

169. Zienkiewicz OC: *The Finite Element Method.* New York, McGraw-Hill, 1991.

170. Zienkiewicz OC, Kelly DW: Finite elements: a unified problem-solving and information transfer method, in Gallagher RH, Simon BR, Johnson PC, Gross JF (eds): *Finite Elements in Biomechanics.* New York, John Wiley & Sons, 1982, pp 9-22.